Combined Model and Mesh Adaptivity within 3D Multiscale XFEM for Cracks

Von der Fakultät für Maschinenbau
der Gottfried Wilhelm Leibniz Universität Hannover

zur Erlangung des akademischen Grades
Doktor-Ingenieurin

genehmigte Dissertation
von

Dipl.-Ing. (FH) Corinna Prange

geboren am 4.3.1984 in Rheda-Wiedenbrück

2014

Herausgeber:
Prof. Dr.-Ing. Peter Wriggers

Verwaltung:
Institut für Kontinuumsmechanik
Gottfried Wilhelm Leibniz Universität Hannover
Appelstraße 11
30167 Hannover

Tel: +49 511 762 3220
Fax: +49 511 762 5496
Web: www.ikm.uni-hannover.de

ISBN 978-3-941302-10-5

1. Referent: Prof. Dr.-Ing. Peter Wriggers
2. Referent: Prof. Stéphane Bordas Ph.D.

Tag der Promotion: 22.04.2014

Abstract

This work presents a possibility to precisely include cracks of different length scales in the same simulation in an efficient way, especially for 3D structures. Experiments show, that cracks of orders of magnitudes smaller than the cracks which are visible to the naked eye influence the crack propagation behavior. As the user of numerical simulations is usually restricted by computer memory as well as computational time, an efficient way to accurately include the smaller cracks in the simulation of structures with considerably larger cracks is needed.
The applied numerical method to include cracks in the simulation is the extended finite element method (XFEM), which allows for meshes that are independent of the crack geometry. However, the accuracy of the solution depends on the mesh resolution. Thus, the representation of cracks of different length scales demands adequate element sizes that are either smaller or at most of a size similar to the smallest cracks considered in the respective domain. Therefore, the analysis is separated for the different length scales with the application of a multiscale projection technique which here leads to two scales. However, to improve the solution while keeping low computational costs, additionally a discretization adaptivity scheme is reasonable.
The adaptive mesh refinement, introduced in this work, can be applied on both scales and is based on a discretization error indicator. The error indication process is recovery based and extends the well-known Z^2 error estimator to the XFEM. The indicator is based on the difference between the current stress field resulting from the simulation and an enhanced, recovered stress field. To recover the enhanced stress field a stress smoothing based on the least squares method is applied. Thereby, the singular stress components around a crack front, are included based on asymptotic analytical solutions for the three analytic stress opening modes. Based on this stress field and the stress field computed by means of the XFEM displacement solution field a relative local error on the element level is approximated. The adaptive mesh refinement according to the local error distribution leads to a nearly equilibrated local error distribution after a few refinement steps. Applying this method, not only regions around the crack front but also regions around re-entrant corners or applied boundary conditions are adaptively refined. Thus, the accuracy of the solution is improved in the entire structure.
Additionally, to define the domain for the fine scale analysis within the multiscale projection method, a model indicator is applied. The recovered smooth stress field already used for the discretization adaptivity gives the possibility to evaluate the L_2 norm of the stress gradient for each element. If a threshold value is exceeded, the respective element is included in the fine scale domain where besides the main cracks, fine scale cracks are given explicitly.

Keywords: XFEM, Cracks, Error Estimation, Discretization Adaptivity, Model Adaptivity

Zusammenfassung

In dieser Arbeit wird eine Möglichkeit dargestellt, Risse verschiedener Längenskalen präzise und effizient in derselben Simulation, insbesondere im 3D Fall, abzubilden. In Experimenten kann gezeigt werden, dass neben Rissen, die mit bloßem Auge erkennbar sind, weitere, um mehrere Größenordnungen kleinere Risse auftreten, die das Risswachstumsverhalten beeinflussen. Der Anwender numerischer Simulationen ist normalerweise in Bezug auf Speicherkapazitäten und Rechenzeit beschränkt, sodass eine Methode erforderlich ist, die eine effiziente Berechnung ermöglicht ohne dabei die Genauigkeit der Ergebnisse zu beeinträchtigen.
Als numerische Methode zur Abbildung von Rissen wird die “extended finite element method” (XFEM) verwendet, die ein finites Element Netz unabhängig von der gegebenen Rissgeometrie ermöglicht. Trotzdem hängt die Genauigkeit der Ergebnisse von der Netzauflösung ab, so dass zur Abbildung von Rissen verschiedener Längenskalen unterschiedliche Elementgrößen verwendet werden sollten, die entweder kleiner oder maximal von der gleichen Größenordnung wie der kleinste Riss des jeweils betrachteten Gebietes sind. Die Berechnung wird daher für die verschiedenen Skalen mit Hilfe einer Multiskalenprojektionsmethode aufgespalten, wobei in dieser Arbeit zwei Skalen berücksichtigt werden. Nichts desto trotz ist eine Verwendung von netzadaptiven Methoden erforderlich, um die Ergebnisse der Simulation zu verbessern, whrend die erforderlichen Computerkapazitten gering gehalten werden.
Die in dieser Arbeit eingeführte adaptive Netzverfeinerung, kann auf beiden Skalen angewendet werden und beruht auf einem glttungsbasierten Diskretisierungsfehlerindikator, der den bekannten Z^2 Fehlerschtzer für die XFEM erweitert. Der Diskretisierungsfehler für jedes finite Element wird über die Differenz zwischen dem geglteten Spannungsfeld und dem aus der Simulation übre das XFEM Verschiebungsfeld auszurechnende Spannungsfeld bestimmt. Spannungssingularitten, die in der Nhe der Rissfront auftreten, werden für das geglttete Spannungsfeld über die asymptotische analytische Lösung für die drei analytischen Rissöffnungsmoden abgebildet. Die auf dem relativen Diskretisierungsfehler basierende Netzverfeinerung führt nach wenigen Verfeinerungsstufen zu einem nahezu gleich verteilten Fehlerfeld im gesamten vernetzten Bauteil. Durch den glttungsbasierten Fehlerindikator werden nicht nur Bereich entlang der Rissfront sondern auch Bereiche mit einspringenden Ecken oder vorgegebenen Randbedingungen verfeinert, wodurch eine genauere Lösung im gesamten Bauteil erreicht wird.
Der Bereich, der für die Feinskalenanalyse innerhalb der Multiskalenrechung verwendet wird, basiert auf einem Modellindikator. Das geglttete Spannungsfeld, das bereits bei der Netzverfeinerung Anwendung findet, wird herangezogen, um die L_2 Norm des Spannungsgradienten für jedes Element zu bestimmen. Anschließend werden alle Elemente, bei denen hierfür ein festgelegter Grenzwert überschritten wird, in der Feinskalenberechnung berücksichtigt. Die Feinskala beinhaltet dabei neben den Grobskalenrissen auch die Feinskalenrisse in expliziter Darstellung.

Schlagworte: XFEM, Risse, Fehlerschätzer, Netzadaptivität, Modelladaptivität

Acknowledgements

This thesis is a result of my work at the Institute of Continuum Mechanics (IKM) at the Leibniz Universität Hannover. The work was guided by Prof. Dr.-Ing. habil. Dr. h.c. mult. Peter Wriggers. The work is based on the DFG project 'Multiscale modeling and extended finite element analysis of fracture processes in ceramics' of Dr.-Ing. Stefan Löhnert. The major aim of the project was to include error estimation and error indication techniques into the extended finite element method for the numerical simulation of cracks in brittle materials.
First of all, my thanks go to my advisor and principal referee Prof. Peter Wriggers for his constant support and his trust in my work. He gave me academical freedom to work, but also fruitful discussions and helpful advise. Prof. Wriggers also encouraged me to present and discuss my work on international conferences from which I benefited extremly.
Furthermore I thank my second referee Prof. Stéphane Bordas for the effort to come to Hanover, but also for open and lively discussions on conferences. His work enriched my knowledge for the full depth of my thesis.
Cordial thanks go to my colleagues of the IKM for the exceptionally good working atmosphere. The in and out office times together with my colleagues supported me a lot in my research and also in teaching activities. Especially I would like to thank Stefan, who had always an open door and shared his knowledge regarding the XFEM and FEAP with me. In a lot of fruitful discussions difficulties could be detected and solutions were found. Thank you for your support and for your trust in my work! Also many thanks to the students who supported my work within different student theses or with advise for special instituts tasks.
I thank cordially the technical staff and office staff which organized the background for my research work.
Sincere thanks to my family and friends who believed in me and who supported me all the time I worked for the thesis. I would particularly like to thank Karsten for his patience especially in the last months.

Hanover, October 2014 Corinna Prange

Drei Dinge helfen, die Mühseligkeiten des Lebens zu tragen:
die Hoffnung, der Schlaf und das Lachen.
Immanuel Kant

Contents

Chapter 1

Introduction

A closer look at fracture of different structures results in the recognition of cracks of different length scales. To account for the influence of these cracks on each other, cracks of multiple length scales have to be included in the same analysis. If a sample includes cracks, which are visible to the naked eye directly, a microscopic view of the sample will show additional smaller cracks. A further zoom will again lead to a visualization of even smaller cracks, voids, inclusions and heterogeneities. In case of an analysis of the overall structure, the influence of the smaller cracks is not negligible. Thus, one goal of this work is to account for these different length scales within the same simulation. Nevertheless, the simulation has to provide accurate results. As a higher precision of the model usually leads to increasing computational costs, a special look at computational efficiency of the applied methods has to be taken.

Fracture mechanics is an important research topic because structures of parts become more and more complex with more flexibility in production processes. Goals of engineering processes are the reduction of weight while often stiffness and life time should be increased. However, as structures are usually man-made, fracture may occur during the life time. In general, the most critical issue is abrupt total fracture. However, a preliminary stage of partial fracture can often be recognized. If parts are cracked only partially, the load capacity of the structure has to be investigated to avoid further cracking. Thus, an efficient analysis to predict further failure leads to the possibility to avoid overloading. With such investigations it can be decided, if the structure can be used for the wanted application or if the structure should no longer be used without additional stabilization which can carry the loads.

To analyze fracture in structures, analytical methods usually yield results only for simple examples. The analysis of complex structures makes use of numerical methods such as the finite element method. However, the more complex the structure, the more computational capacities have to be provided for a simulation. To keep the computational costs and the computational time low, different possibilities exist to modify the numerical simulation, otherwise only powerful computer cluster systems are able to obtain accurate solutions. One possibility is to consider cracks at different length scales usingmultiscale techniques. Thus, the cracks of each scale can be modeled separately and still influence the results on other scales. Therefore, different models have to be considered, which are located in subdomains of the overall structure. To define these domains a model indicator is helpful. Improvements for the results are achieved by an error analysis of the structure. Applying error indicators

leads to an adaptive control for the mesh used in the finite element simulation. Furthermore, the application of error indicators leads to an adaptive definition of the domains for models including effects of smaller length scales. Thus, the computational costs can stay low, while accuracy is in the focus of the analysis.

Different aspects of these topics as well as issues of previous research are discussed at the beginning of the corresponding chapter of this thesis. Thereafter, each chapter includes an explanation of the relevant aspects.

The goal of this thesis is an efficient and accurate solution for finite element simulations, which include cracks on different length scales. The structure of this thesis leads to a stepwise fulfillment of this goal in the following way:

First of all, the required aspects of continuum mechanics are introduced in chapter 2 as the regarded structures are assumed to behave in the context of continuum mechanics.

Thereafter, some aspects of fracture mechanics are presented in chapter 3. The analytical description of cracks in the context of linear elastic fracture mechanics is introduced. Thereby, the analytic solution for crack opening is described as the analytical functions are later on also needed for the numerical simulation of cracks. The interaction of cracks is also in the focus of this chapter. Therefore, earlier studies as well as recent experiments are taken into account. The influence of cracks on different length scales on the overall crack propagation behavior is determined in the experiments. The resulting complex crack interaction behavior for structures with arbitrary crack geometries cannot be covered by the analyitcal solutions. Thus, a numerical method has to be utilized to predict these solutions.

In chapter 4 the finite element method (FEM) is discussed. Different modifications to apply the FEM to fracture mechanics are presented. As the applicability of these modifications to fracture mechanics differs for increasing complexity of the crack, the extended finite element method (XFEM) is chosen for the applications presented in this thesis. Aspects concerning the accuracy are discussed in more detail, as accurate solutions are - besides the inclusion of different length scales - the main topic of this thesis.

The XFEM enables a lot of applications regarding simulations of fracture. However, cracks of different length scales in the same simulation lead to large computational effort, especially in 3D. Thus, multiscale methods are presented in chapter 5. With the application of multiscale techniques to the XFEM, cracks of different length scales can be analyzed in subscale simulations. As a result, the computational effort to solve problems with interacting cracks of different length scales is reduced. Nevertheless, 3D simulations can easily exceed the computer capacities of modern standard computer architectures. Additionally, an acceptable computational time, especially for industrial applications, cannot be guaranteed. Further reduction of computational efforts are possible using adaptivity strategies within the XFEM model. These adaptive schemes can be realized with the application of error indication techniques. Furthermore, error indicators lead to a qualitative evaluation of the solution. And in addition, the accuracy of the solution can be improved, if adaptive schemes are applied.

Two types of adaptivity techniques are discussed in chapter 6. The first technique is the so-called mesh adaptivity. This technique is based on an error indicator. With the application of the error indicator an evaluation of the computed solution is possible and thus mesh refinement can be adaptively accomplished. The second adaptivity technique is the so-called model adaptivity. To consider the cracks of different length scales in an accurate and efficient

way, the finite element model has to be adapted. Especially in domains of crack propagation or expected crack nucleation, the influence of the underlying microstructure of the material has to be taken into account. To define these domains, a model indicator is applied. Dependent on the load case, the material properties and the geometry of the entire structure, a model which includes the microstructure, is applied using the model indicator. A numerical validation of the applied model indicator is given.
In chapter 7, numerical results are presented to discuss the performance of the aforementioned computational methods. Discretization adaptivity is presented for various types of material behavior. Results for the presented methods applied to arbitrary meshes and cracks in 3D are shown. Furthermore, in an example based on experimental results, the efficient simulation of cracks of different length scales is demonstrated.
Finally, the applied techniques are summarized in chapter 8. Additionally, further extensions of the introduced methods are presented, e.g. aspects which have to be considered in case of crack propagation.

Chapter 2

Continuum Mechanics

To analyze the behavior of bodies under certain loading conditions, different assumptions have to be utilized. Within this work, each body is assumed to behave in the context of continuum mechanics. A body is defined to consist of a homogeneous material, i.e. micro effects can be captured but the microscopic system is not modelled in detail. At each point of a body the properties are defined to be the same. A short overview of kinematics, balance principles and constitutive equations is given in this chapter. The presented equations are restricted to small deformations. Detailed information about continuum mechanics for finite deformations and more details about mentioned aspects can be found e.g. in (4; 12; 27; 77; 81; 115)
In section 2.1 a strain tensor for small deformations is introduced. Balance principles are presented in section 2.2 and constitutive equations for the material behavior are given in section 2.3.

2.1 Kinematics and Strains

A material body $\mathcal{B}$ with its boundary $\partial\mathcal{B}$ is defined by a composition of material points $\mathcal{P}$ in the EUKLIDean space $\mathbb{E}^3$. A configuration of $\mathcal{B}$ can then be denoted by

$$\chi : \mathcal{B} \rightarrow \mathbb{E}^3 \tag{2.1}$$

and the position of a material point $\mathcal{P} \in \mathcal{B}$ can be expressed as

$$\boldsymbol{x} = \chi(\mathcal{P}). \tag{2.2}$$

This position vector of each material point is prescribed with $\boldsymbol{x} = x_i \boldsymbol{e}_i$ where $\boldsymbol{e}_i$ are the unit vectors of an orthogonal basis system and x_i are the corresponding components of $\boldsymbol{x}$.
The displacement of each material point can be described by three components, each in the direction of one of the three basis vectors. Thus, the displacement is defined as

$$\boldsymbol{u} = u_i \boldsymbol{e}_i. \tag{2.3}$$

Assuming the material points of the body to be connected during the motion, the displacements are continuous functions.

Therefore, the derivative of the displacement with respect to the position vector is calculable as

$$\text{grad}\,(\boldsymbol{u}) = \frac{\partial \boldsymbol{u}}{\partial \boldsymbol{x}}. \tag{2.4}$$

Considering small deformations around $\boldsymbol{u} = \boldsymbol{0}$ the strain tensor is defined as

$$\boldsymbol{\varepsilon} = \frac{1}{2}\left(\frac{\partial \boldsymbol{u}}{\partial \boldsymbol{x}} + \left(\frac{\partial \boldsymbol{u}}{\partial \boldsymbol{x}}\right)^T\right). \tag{2.5}$$

2.2 Balance Equations

Based on fundamental physical observations, some principles within the theory of continuum mechanics have to be fulfilled. Therefore, balance principles are used to describe the evolution of mass, linear and angular momentum, energy and entropy. These equations are independent of the material behavior.
For elastic deformations no energy of the system is dissipated. In this case, the balance of energy does not yield any new information in addition to the balance of linear momentum. For plasticity however, some of the mechanical energy is dissipated due to plastic deformations. This usually leads to an increase in temperature. Thus, the balance of entropy has to be taken into account.
The theory for small deformations is assumed here, leading to only one configuration of the body. As a configuration describes the deformation state, rigid body motions cannot be described in the context of small deformations. In the following section the balance of linear momentum, the balance of angular momentum, the balance of energy and the balance of entropy are briefly explained. These general principles can be formulated in integral (global) or differential (local) form.

Balance of linear momentum

External mechanical forces act as tractions $\boldsymbol{t}$ on the surface $\partial\mathcal{B}$ and as volume forces $\boldsymbol{b}$ on the body $\mathcal{B}$. The total linear momentum $\boldsymbol{I}$ of a body is defined as

$$\boldsymbol{I} = \int_{\mathcal{B}} \rho \boldsymbol{v}\, \mathrm{d}v \tag{2.6}$$

with the material density ρ and the velocity $\boldsymbol{v} = v_i \boldsymbol{e}_i$. Its time derivative is equal to the sum of all external mechanical forces $\boldsymbol{F}^{ext}$, which leads to the balance of linear momentum

$$\dot{\boldsymbol{I}} = \frac{\mathrm{d}}{\mathrm{d}t}\int_{\mathcal{B}} \rho \boldsymbol{v}\, \mathrm{d}v = \int_{\mathcal{B}} \rho \boldsymbol{a}\, \mathrm{d}v = \int_{\mathcal{B}} \boldsymbol{b}\, \mathrm{d}v + \int_{\partial\mathcal{B}} \boldsymbol{t}\, \mathrm{d}a = \boldsymbol{F}^{ext} \tag{2.7}$$

considering the acceleration $\boldsymbol{a} = a_i \boldsymbol{e}_i$ and no changes in the material density, i.e. $\dot{\rho} = 0$. This global formulation of the balance of linear momentum can be reformulated solely in volume

integral terms. Therefore, the traction vector $\boldsymbol{t}$ acting on the surface of an arbitrary cut of the body is expressed as a linear function of the outward normal vector $\boldsymbol{n}$ to this surface, known as CAUCHY's theorem $\boldsymbol{t} = \boldsymbol{\sigma} \cdot \boldsymbol{n}$. Here, $\boldsymbol{\sigma}$ is the CAUCHY stress tensor. Additionally, the GAUSS theorem for the transformation of a surface integral to a volume integral is applied. The general formulation of the GAUSS theorem for a tensor $\boldsymbol{A}$ is denoted as

$$\int_{\mathcal{B}} \operatorname{div}(\boldsymbol{A}) \, \mathrm{d}v = \int_{\partial\mathcal{B}} \boldsymbol{A} \cdot \boldsymbol{n} \, \mathrm{d}a. \tag{2.8}$$

With the CAUCHY theorem and the GAUSStheorem, the global formulation of the balance of linear momentum can then be rewritten as

$$\int_{\mathcal{B}} (\operatorname{div} \boldsymbol{\sigma} + \boldsymbol{b} - \rho \boldsymbol{a}) \, \mathrm{d}v = \boldsymbol{0}. \tag{2.9}$$

As mentioned above, the balance equations hold true for global and local formulations. The local form of the balance of momentum is

$$\operatorname{div} \boldsymbol{\sigma} + \boldsymbol{b} - \rho \boldsymbol{a} = \boldsymbol{0}. \tag{2.10}$$

For static problems the acceleration $\boldsymbol{a}$ vanishes, which leads to the static local formulation applied in this work

$$\operatorname{div} \boldsymbol{\sigma} + \boldsymbol{b} = \boldsymbol{0}. \tag{2.11}$$

Balance of angular momentum

Considering an arbitrary fixed point $\mathcal{P}_0$ and its position vector $\boldsymbol{x}_0$, the angular momentum $\boldsymbol{L}$ of the body $\mathcal{B}$ is defined as

$$\boldsymbol{L} = \int_{\mathcal{B}} (\boldsymbol{x} - \boldsymbol{x}_0) \times \rho \boldsymbol{v} \, \mathrm{d}v. \tag{2.12}$$

The time derivative of the angular momentum is the sum of all external moments $\boldsymbol{M}_0^{ext}$ acting on the body with respect to $\boldsymbol{x}_0$. This leads to the global formulation of the balance of angular momentum denoted by

$$\int_{\mathcal{B}} (\boldsymbol{x} - \boldsymbol{x}_0) \times \rho \boldsymbol{a} \, \mathrm{d}v = \int_{\mathcal{B}} (\boldsymbol{x} - \boldsymbol{x}_0) \times \boldsymbol{b} \, \mathrm{d}v + \int_{\partial\mathcal{B}} (\boldsymbol{x} - \boldsymbol{x}_0) \times \boldsymbol{t} \, \mathrm{d}a. \tag{2.13}$$

The CAUCHY theorem, the GAUSS theorem and the requirement that the balance principles have to be satisfied for every point inside a continuum result in the local form

$$\operatorname{div}((\boldsymbol{x} - \boldsymbol{x}_0) \times \boldsymbol{\sigma}) + (\boldsymbol{x} - \boldsymbol{x}_0) \times (\boldsymbol{b} - \rho \boldsymbol{a}) = \boldsymbol{0} \tag{2.14}$$

which is for static problems reduced to

$$\operatorname{div}((\boldsymbol{x} - \boldsymbol{x}_0) \times \boldsymbol{\sigma}) + (\boldsymbol{x} - \boldsymbol{x}_0) \times \boldsymbol{b} = \boldsymbol{0}. \tag{2.15}$$

Applying the balance of linear momentum (2.10) to (2.14) leads to the symmetry of the CAUCHY stress tensor

$$\boldsymbol{\sigma} = \boldsymbol{\sigma}^T. \tag{2.16}$$

Balance of energy

Without external power the total energy $E = K + U$ within a closed system is constant. Therefore, the rate of the energy $\dot{E}$ has to be equal to the external power. This leads to

$$\frac{\mathrm{d}}{\mathrm{d}t}(K + U) = P + Q \tag{2.17}$$

where the kinetic energy K and the internal energy U are defined as

$$K = \frac{1}{2}\int_{\mathcal{B}} \rho \boldsymbol{v} \cdot \boldsymbol{v}\,\mathrm{d}v \quad ; \qquad U = \int_{\mathcal{B}} \rho u\,\mathrm{d}v \tag{2.18}$$

with the specific internal energy u.
The external power is given as the sum of the mechanical part P and the thermal part Q. The mechanical part includes body forces $\boldsymbol{b}$ and boundary tractions $\boldsymbol{t}$

$$P = \int_{\mathcal{B}} \boldsymbol{b} \cdot \boldsymbol{v}\,\mathrm{d}v + \int_{\partial\mathcal{B}} \boldsymbol{t} \cdot \boldsymbol{v}\,\mathrm{d}a. \tag{2.19}$$

Thermal power includes heat sources ρr within the body and the inwards boundary heat flux vector $\boldsymbol{q}$ on the surface of the body

$$Q = \int_{\mathcal{B}} \rho r\,\mathrm{d}v - \int_{\partial\mathcal{B}} \boldsymbol{q} \cdot \boldsymbol{n}\,\mathrm{d}a. \tag{2.20}$$

Inserting (2.18)-(2.20) into (2.17) leads to the global formulation for the balance of energy

$$\frac{\mathrm{d}}{\mathrm{d}t}\int_{\mathcal{B}} \rho\left(u + \frac{1}{2}\boldsymbol{v} \cdot \boldsymbol{v}\right)\mathrm{d}v = \int_{\mathcal{B}} \rho r + \boldsymbol{b} \cdot \boldsymbol{v}\,\mathrm{d}v + \int_{\partial\mathcal{B}} \boldsymbol{t} \cdot \boldsymbol{v} - \boldsymbol{q} \cdot \boldsymbol{n}\,\mathrm{d}a. \tag{2.21}$$

Applying the CAUCHY theorem and the GAUSS theorem to (2.21), the local formulation is written as

$$\rho\dot{u} + \rho\boldsymbol{v} \cdot \boldsymbol{a} = \boldsymbol{b} \cdot \boldsymbol{v} + \rho r + \operatorname{grad}\boldsymbol{v} : \boldsymbol{\sigma} + \boldsymbol{v}\operatorname{div}\boldsymbol{\sigma} - \operatorname{div}\boldsymbol{q}. \tag{2.22}$$

With the balance of linear momentum (2.10) the strong form of the balance of energy is

$$\rho\dot{u} = \rho r + \operatorname{grad}\boldsymbol{v} : \boldsymbol{\sigma} - \operatorname{div}\boldsymbol{q}. \tag{2.23}$$

Balance of entropy

The balance of entropy restricts possible directions of a thermomechanical process. The internal energy is a state variable and defined to depend on the current entropy density s and further mechanical variables $u = u(s, v_1, v_2, ..., v_n)$ (150) and is rewritten with the free energy density Ψ as $u = u(s) + u(v_1, v_2, ..., v_n) = \theta s + \psi$. For a homogeneous material, the differentiation of u in time leads to

$$\dot{u} = \dot{\theta}s + \theta\dot{s} + \dot{\psi}. \tag{2.24}$$

The internal energy can be seen as a potential for the temperature θ.
Substituting equation (2.24) into the local form of the balance of energy (2.23) leads to

$$\rho\dot{\theta}s + \rho\theta\dot{s} + \rho\dot{\psi} = \rho r + \operatorname{grad}\boldsymbol{v} : \boldsymbol{\sigma} - \operatorname{div}\boldsymbol{q}. \tag{2.25}$$

After integration over the body and some algebra, the global balance of entropy can then be written as

$$\begin{aligned}\int_{\mathcal{B}} \rho\dot{\theta}s \,\mathrm{d}v + \int_{\mathcal{B}} \rho\theta\dot{s} \,\mathrm{d}v = \int_{\mathcal{B}} \operatorname{grad}\boldsymbol{v} : \boldsymbol{\sigma} \,\mathrm{d}v - \int_{\mathcal{B}} \rho\dot{\psi} \,\mathrm{d}v \\ + \int_{\mathcal{B}} \rho r \,\mathrm{d}v - \int_{\partial\mathcal{B}} \boldsymbol{q}\cdot\boldsymbol{n} \,\mathrm{d}a - \int_{\mathcal{B}} \frac{1}{\theta}\boldsymbol{q}\cdot \operatorname{grad}\theta \,\mathrm{d}v.\end{aligned} \tag{2.26}$$

For a constant value of θ ($\dot{\theta} = 0$) and without external heat sources, the system can receive mechanical power but not provide it. Thus, the difference between the external mechanical power P_E and the internal mechanical power P_I is greater or equal to zero

$$P_E - P_I = \int_{\mathcal{B}} \operatorname{grad}\boldsymbol{v} : \boldsymbol{\sigma} \,\mathrm{d}v - \int_{\mathcal{B}} \rho\dot{\psi} \,\mathrm{d}v \geq 0. \tag{2.27}$$

Additionally, without changes in mechanical energy and without external heat sources, the heat flow is directed from the warmer to the colder part of the body which is

$$\int_{\mathcal{B}} \frac{1}{\theta}\boldsymbol{q}\cdot \operatorname{grad}\theta \,\mathrm{d}v \geq 0. \tag{2.28}$$

Consequently, the three mentioned terms in equations (2.27) and (2.28) are together always ≥ 0. Therefore, the global balance of entropy can be rewritten as the global entropy inequality, also known as CLAUSIUS-DUHEM inequality

$$\int_{\mathcal{B}} \rho\dot{s} \,\mathrm{d}v \geq \int_{\mathcal{B}} \frac{\rho r}{\theta} \,\mathrm{d}v - \int_{\partial\mathcal{B}} \frac{1}{\theta}\boldsymbol{q}\cdot\boldsymbol{n} \,\mathrm{d}a. \tag{2.29}$$

2.3 Constitutive Equations

Additional to the equations resulting from the balance principles, further equations are required to compute all unknowns of the mechanical problem. Constitutive equations give a phenomenological basis to describe the macroscopic qualities of a material. To develop constitutive equations, the general principles of continuum mechanics have to be considered. These principles couple independent (e.g. displacements) with dependent (e.g. stresses) variables within a physically admissible frame. Material models including large deformations or strong nonlinear material behavior, for instance damage, can be developed. The principles of continuum mechanics are explained and considered for the material models of small elastic and elasto-plastic deformations. The principles of continuum mechanics are:

- Principle of causality: The only independent variables are the displacement $\boldsymbol{u}$ and the temperature θ of a thermomechanical body. All other variables, which can be determined using $\boldsymbol{u}$ and θ, are constitutively dependent variables.

- Principle of determinism: The values of the independent variables at a material point only depend on the history of motion and temperature of all points of the body and are not influenced by future settings.

- Principle of equipresence: All constitutive equations consider the same set of independent variables.

- Principle of material frame indifference: The constitutive equations are invariant to rigid body motions and to the observer's position.

- Principle of material symmetry: The constitutive equations are independent for a transformation of the material coordinates relating to a symmetry group of the material.

- Principle of local effect: The independent variables further away from a material point do not influence the constitutive relations at that material point.

- Principle of fading memory: The actual constitutive quantities are only influenced by the actual loading and the near past and not by the constitutive quantities in a larger temporal range.

- Principle of consistency: The constitutive equations have to be consistent with the balance equations of section 2.2.

These principles are based on generalized experience with an axiomic character. Different material descriptions based on these principles exist in literature. For hyperelastic material models the constitutive behavior is often described by the strain energy function Ψ.
A well-known material model is the linear elastic isotropic HOOKE's law for small deformations. The strain energy function reads

$$\Psi = \rho\psi = \frac{\Lambda}{2}\mathrm{tr}^2(\boldsymbol{\varepsilon}) + \mu\mathrm{tr}(\boldsymbol{\varepsilon}^2). \tag{2.30}$$

The material parameters μ and Λ ($\mu > 0, \Lambda > 0$) are the LAMÉ constants, which are used instead of YOUNG's modulus E and POISSON's ratio ν for historic reasons. The material constants can be converted using

$$\mu = \frac{E}{2\,(1+\nu)} \qquad \Lambda = \frac{E\nu}{(1+\nu)(1-2\nu)}. \tag{2.31}$$

The differentiation of the strain energy density function with respect to the strain tensor leads to the stresses

$$\boldsymbol{\sigma} = \frac{\partial\Psi}{\partial\boldsymbol{\varepsilon}} = 2\mu\boldsymbol{\varepsilon} + \Lambda\mathrm{tr}(\boldsymbol{\varepsilon})\mathbf{1} = \mathbb{C}\colon\boldsymbol{\varepsilon} \tag{2.32}$$

with the linear elastic fourth order tensor for isotropic behavior which includes the fourth order symmetric identity tensor $\mathbb{I}^{sym}$

$$\mathbb{C} = \frac{\partial^2 \Psi}{\partial \boldsymbol{\varepsilon} \partial \boldsymbol{\varepsilon}} = 2\mu \mathbb{I}^{sym} + \Lambda \mathbf{1} \otimes \mathbf{1}. \tag{2.33}$$

Regarding the principles of continuum mechanics, HOOKE's law does not fulfill the principle of material frame indifference as rigid body motions lead to strains and stresses. Other principles of continuum mechanics are not violated. Independent variables within this material model are displacements which satisfy the principle of determinism. HOOKE's law is unique in the translation between strains and stresses and the fulfillment of the principle of equipresence is obvious. Furthermore, the constitutive variables of a linear elastic material behavior only depend on the actual loading and are independent of deformation history and time. Therefore, the principle of fading memory is fulfilled. The displacement gradient is the only variable which influences the material behavior at a specific point. As equation (2.32) represents an isotropic material behavior, all possible material symmetries are given. The balance of entropy is considered within HOOKE's law, as well.
Besides linear elasticity, linear elastic ideal plastic material behavior is applied in section 7.1. Plasticity is based on the irreversibility of the deformation process as energy dissipates. To reflect this material behavior, an additional inner variable is introduced, namely the plastic strain. The overall strain is additively split into an elastic and a plastic part

$$\boldsymbol{\varepsilon} = \boldsymbol{\varepsilon}^e + \boldsymbol{\varepsilon}^p. \tag{2.34}$$

By means of a stored energy function, the free energy density function now only depends on the elastic part of the deformation and is rewritten as

$$\Psi = \frac{\Lambda}{2} \mathrm{tr}^2(\boldsymbol{\varepsilon}^e) + \mu \mathrm{tr}(\boldsymbol{\varepsilon}^e \cdot \boldsymbol{\varepsilon}^e). \tag{2.35}$$

Within associated plasticity, the VON MISES flow rule may be used to define the flow rule:

$$\Phi(\boldsymbol{\sigma}) = \|\boldsymbol{s}\| - \sqrt{\frac{2}{3}}\sigma_0 \leq 0, \tag{2.36}$$

where σ_0 is the flow stress, $\sqrt{\frac{2}{3}}\sigma_0$ is the radius of the yield surface and $\boldsymbol{s}$ is the deviatoric stress tensor

$$\boldsymbol{s} = \boldsymbol{\sigma} - \frac{1}{3}\mathrm{tr}(\boldsymbol{\sigma})\mathbf{1}. \tag{2.37}$$

The flow rule itself is

$$\dot{\boldsymbol{\varepsilon}}^p = \gamma \boldsymbol{N}; \quad \gamma \geq 0, \tag{2.38}$$

with the plastic multiplier γ and the flow direction for the associated flow rule $\boldsymbol{N} = \frac{\mathrm{d}\Phi}{\mathrm{d}\sigma}$. The flow rule gives the evolution law for the plastic strain. With (2.36), the flow rule yields

$$\Phi < 0 \qquad \gamma = 0 \quad \text{for pure elastic material behavior} \tag{2.39}$$

$$\Phi = 0 \qquad \gamma > 0 \quad \text{for plastic material behavior} \tag{2.40}$$

which can be rewritten as the complementarity or KUHN-TUCKER conditions

$$\Phi \leq 0 \qquad \gamma \geq 0 \qquad \Phi\gamma = 0 \tag{2.41}$$

and the consistency requirement

$$\gamma\dot{\Phi} = 0. \tag{2.42}$$

For this material model the principles of continuum mechanics have to be considered, as well. The irreversibility of the plastic strain necessitates a closer look at the balance of entropy (2.29) in the local form. An isothermal process with a homogeneous temperature distribution is assumed for the mechanical computation. The mechanical behavior is modeled independent of temperature effects, which results in a constant elastic modulus and no change of the flow stress. Dissipated mechanical work leads to a change in temperature which should be negligible concerning the heat capacity of the material.
Neglecting temperature effects, the dissipation $\mathcal{D}$ has to be consistent with the balance of entropy and has to fulfill equation (2.27)

$$\mathcal{D} = \boldsymbol{\sigma} : \dot{\boldsymbol{\varepsilon}} - \dot{\Psi} \geq 0. \tag{2.43}$$

The first term includes elastic and plastic strains whereas the second term only depends on elastic strains. Thus, the dissipation can be rewritten as

$$\mathcal{D} = \boldsymbol{\sigma} : (\dot{\boldsymbol{\varepsilon}^e} + \dot{\boldsymbol{\varepsilon}^p}) - \boldsymbol{\sigma} : \dot{\boldsymbol{\varepsilon}^e} = \boldsymbol{\sigma} : \dot{\boldsymbol{\varepsilon}^p}. \tag{2.44}$$

With the plastic flow defined in equation (2.38), $\mathcal{D} \geq 0$ always holds true, i.e. the balance of entropy is valid for the applied material model.
Further and more complex plastic material descriptions can be found in e.g. (77; 133).
An extension of the material model to finite deformations, nonlinear material behavior, damage among others can be considered. In those cases computational costs have to be seen in contrast to the necessity of aspects which have to be implemented.

Chapter 3

Fracture Mechanics

Increasing the load on a physical system may induce fracture in parts of the system, which can lead to an overall failure. Therefore, fracture mechanics has to be taken into account. Even with a restriction to continuum mechanics, which excludes the nanometer scale, fracture has to be considered, because cracks lead to singularities in the stress field. Microdefects, such as pores or micro cracks, might lead to cracks in a solid. After crack initiation, crack propagation leads to an overall failure of different mechanical parts. Detailed information to crack initiation processes can be found in (5; 73; 93). In this work, a body with an initial crack of a defined length is assumed. The crack propagation process depends on the material, the temperature, the geometry and the loading velocity. For ductile materials, a distinct fracture process zone can be detected. Within this zone, the complex processes of material debonding takes place. If continuum mechanics is assumed for the overall body, this zone has to be infinitesimal small which is not the case e.g. for some concrete materials. For brittle materials, such as ceramics, the fracture process zone can be neglected because of its marginal size. Furthermore, stationary and propagating cracks have to be distinguished. For a given stationary crack, possible loading cases can be analyzed, before crack propagation occurs.
Detailed information on fracture mechanics can be found in (5; 73; 93). In this chapter an overview of the analytical solution of the stress field resulting from cracks and an introduction to crack propagation criteria is given in section 3.1. Thereafter, cracks on different length scales are explored in section 3.2 where first a reference to earlier studies is given and afterwards recent experimental results are presented.

3.1 Analytical Description of Cracks

A crack consists of a crack surface and a crack tip in 2D or rather a crack front in 3D. The crack surfaces are assumed to be traction free. For planar cracks within the concept of linear elastic fracture mechanics, three different crack opening modes exist. Mode I is obtained by tension perpendicular to the crack surfaces, sketched in figure 3.1a. Shearing normal to the crack front within the plane of the crack surfaces induces mode II crack opening, displayed in figure 3.1b. Mode III is achieved with loading tangential to the crack front in the plane of the crack surfaces, illustrated in figure 3.1c. Every crack opening can be described with a

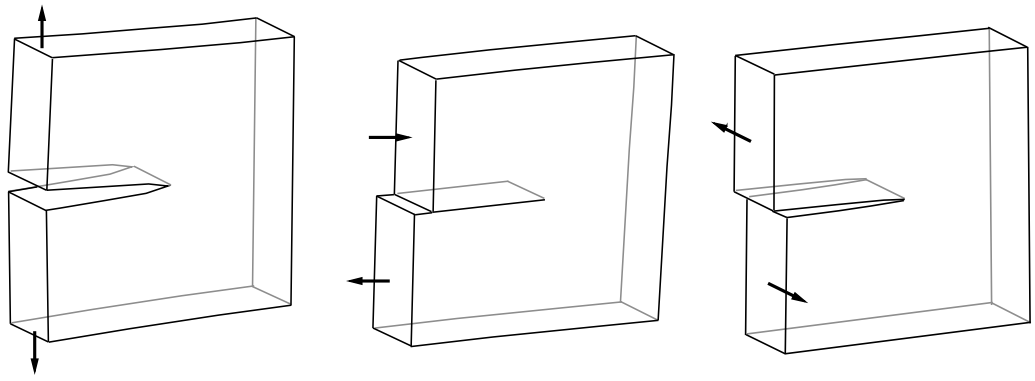

a) Mode I b) Mode II c) Mode III

Figure 3.1: Different types of crack opening.

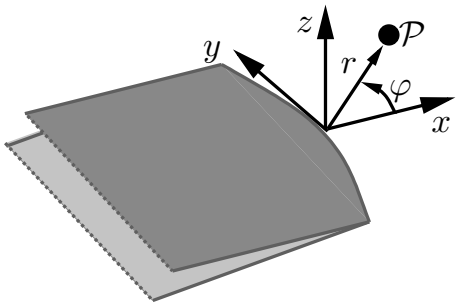

Figure 3.2: Cartesian coordinate system along the crack front and illustration of the distance r and the angle φ used for the analytical stress calculation around a crack front at a point $\mathcal{P}$ in the x-z plane.

superposition of these three crack opening modes due to linear elasticity.
Analytical solutions for fracture problems were already discovered in 1939. WESTERGAARD proposed complex stress functions for the description of the stress fields around the crack front (155). These functions are still used to represent the behavior of stress fields around crack fronts. For a point $\mathcal{P}$ next to a crack front the solution for the stresses depends on the distance r to the crack front and on the angle φ, illustrated in figure 3.2.
A first description for circular and elliptical cracks for 3D problems can be found in (136). These solutions are of the same type as for the 2D asymptotic analytical solution field and are a combination of all three modes as shown in (73; 76; 93; 136). The solutions can be generated using the stress solution for mode I and mode II plain strain and a cartesian coordinate system moved along with the crack front. The axes of the cartesian coordinate system are such that x is aligned with the tangential crack surface perpendicular to the crack front, y is tangential to the crack front line and z is perpendicular to the crack front and the crack surface at the crack front, as shown in figure 3.2. The figure and the following equations for the analytical solutions are similar to the fracture mechanics theory presented in (73).
The analytical solution for the stress fields is a combination of all three modes

$$\sigma_{ij} = \frac{1}{\sqrt{2\pi r}} \left[K_I \tilde{\sigma}_{ij}^{I}(\varphi) + K_{II} \tilde{\sigma}_{ij}^{II}(\varphi) + K_{III} \tilde{\sigma}_{ij}^{III}(\varphi) \right]. \tag{3.1}$$

$\tilde{\sigma}_{ij}^{m}$, $m = I, II, III$ are functions depending on the actual angle to the crack front and are given in table 3.1 for all modes.

Mode I	Mode II	Mode III
$\tilde{\sigma}^I_{xx} = \cos(\varphi/2)$ $[1 - \sin(\varphi/2)\sin(3\varphi/2)]$	$\tilde{\sigma}^{II}_{xx} = -\sin(\varphi/2)$ $[2 + \cos(\varphi/2)\cos(3\varphi/2)]$	$\tilde{\sigma}^{III}_{xx} = 0$
$\tilde{\sigma}^I_{yy} = \nu(\sigma_x + \sigma_z)$	$\tilde{\sigma}^{II}_{yy} = \nu(\sigma_x + \sigma_z)$	$\tilde{\sigma}^{III}_{yy} = 0$
$\tilde{\sigma}^I_{zz} = \cos(\varphi/2)$ $[1 + \sin(\varphi/2)\sin(3\varphi/2)]$	$\tilde{\sigma}^{II}_{zz} = \sin(\varphi/2)$ $\cos(\varphi/2)\cos(3\varphi/2)$	$\tilde{\sigma}^{III}_{zz} = 0$
$\tilde{\sigma}^I_{xy} = 0$	$\tilde{\sigma}^{II}_{xy} = 0$	$\tilde{\sigma}^{III}_{xy} = \sin(\varphi/2)$
$\tilde{\sigma}^I_{yz} = 0$	$\tilde{\sigma}^{II}_{yz} = 0$	$\tilde{\sigma}^{III}_{yz} = -\cos(\varphi/2)$
$\tilde{\sigma}^I_{xz} = \cos(\varphi/2)$ $\sin(\varphi/2)\cos(3\varphi/2)$	$\tilde{\sigma}^{II}_{xz} = \cos(\varphi/2)$ $[1 - \sin(\varphi/2)\sin(3\varphi/2)]$	$\tilde{\sigma}^{III}_{xz} = 0$

Table 3.1: Analytic solutions for stresses around a crack front for the three modes.

K_m, $m = I, II, III$ in equation (3.1) are the stress intensity factors belonging to each mode. They were first introduced by IRWIN in 1957 (86) based on a modification of GRIFFITH's theory (72). However, these solutions are not applicable to interface cracks between different materials. Solutions to interface cracks can be found in (126).
An exception to the use of the described type of solution for the 3D case are kinks in a crack front or the point where the crack front exceeds the domain surface. In these cases, the singularity at a crack front is modified. Within the presented work these exceptions are excluded. Thus, at every point of a crack front, the analytical solutions presented in table 3.1 are assumed.
Considering linear elasticity, mode I loading leads to a parabolic crack opening and a $r^{-1/2}$ singularity of the stress field at a crack front. For elastic-plastic material behavior the singularity at a crack front changes because the stresses are restricted by a yield stress. The strains still remain singular but the geometry of the crack front is blunted due to a transfer of strains and stresses caused by a plastic zone.
After analyzing strains and stresses in a part including one or more cracks, solutions for crack propagation are also available. Different criteria to determine the direction of crack propagation exist. A common criterion for crack propagation in linear elastic fracture mechanics based on stress intensity factors is the energy release rate. A precondition for the application of the energy release rate is a material description with the strain energy density function (e.g. equation (2.30)) based on an internal elastic potential formulation

$$\Pi^i = \int_{\mathcal{B}} \Psi \, \mathrm{d}V. \tag{3.2}$$

Additionally, the external surface or volume loads applied to the precracked elastic body have the potential Π^e. The crack is assumed to propagate from equilibrium state (A) to equilibrium state (B) with an extension of ΔA, displayed in figure 3.3. In the first equilibrium state the body is assumed to be already cut along ΔA and the stresses at the surface are assumed as

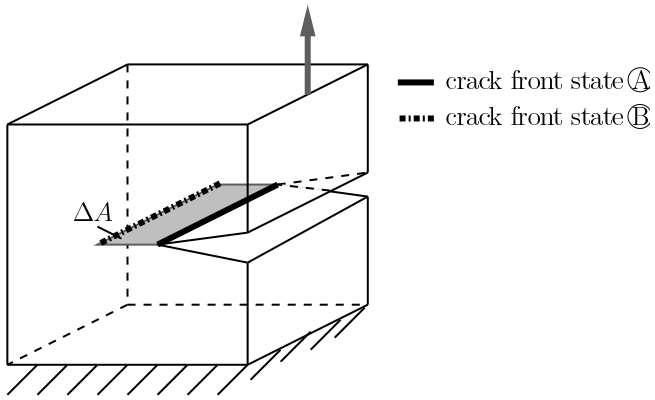

Figure 3.3: Propagation of a crack with an extension ΔA.

an external load such that the crack opening along ΔA is zero. Thereafter, these stresses are quasi-statically reduced to zero, which leads to equilibrium state Ⓑ. The work of the surface stresses from equilibrium state Ⓐ to equilibrium state Ⓑ is less or equal to zero, thus $\Delta W_\sigma \leq 0$. The work of the applied external forces can be seen as a difference of the external potential. The difference of the inner potential has to equilibrate the difference of the total external applied work

$$\Delta\Pi^i = \Delta\Pi^e + \Delta W_\sigma \quad \Rightarrow \quad \Delta\Pi = \Delta W_\sigma \leq 0. \tag{3.3}$$

The mechanical energy of the system is reduced during crack propagation and this energy is available for the crack propagation process. The released energy $-\,\mathrm{d}\Pi$ related to an infinite crack propagation step $\mathrm{d}A$ is then the energy release rate

$$\mathcal{G} = -\frac{\mathrm{d}\Pi}{\mathrm{d}A}. \tag{3.4}$$

Based on the criterion of GRIFFITH (72), the crack propagates if the energy release rate equals the material specific parameter $\mathcal{G}_c$. The energy release rate can be written in terms of the stress intensity factors for the linear elastic case

$$\mathcal{G} = \frac{1-\nu^2}{E}(K_I^2 + K_{II}^2) + \frac{1+\nu}{E}K_{III}^2. \tag{3.5}$$

Thus, knowing the stress intensity factors it can be evaluated whether the crack propagates. Additionally, the direction of crack growth φ_c has to be defined. Commonly, the maximum hoop stress (50), based on the stress intensity factors, is chosen to define the direction of crack propagation. The crack propagates in a direction perpendicular to the maximum hoop stress. For pure mode I loading, i.e. $K_{II} = 0$, this is in the plane of the crack surface. For mixed mode loading, the direction of growth yields

$$\varphi_c = 2\arctan\frac{1}{4}\left(\frac{K_I}{K_{II}} - \frac{K_{II}}{\|K_{II}\|}\sqrt{\frac{K_I^2}{K_{II}^2}+8}\right) \quad \forall\, K_{II} \neq 0. \tag{3.6}$$

As the crack propagation criterion as well as the direction of crack propagation depend on the stress intensity factors, the determination of those quantities is inevitable. An analytical

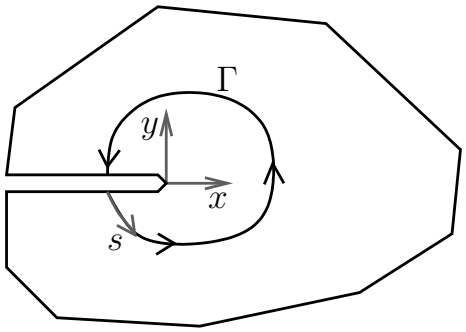

Figure 3.4: Contour for the J-integral.

way to evaluate the stress intensity factors is the so-called J-integral introduced by RICE in 1968 (125). Here, the strain energy density function has to be a potential function. The J-integral is a contour integral starting at one crack surface surrounding the crack tip and ending at the opposite crack surface, illustrated in figure 3.4. The J-integral is defined for crack propagation in x direction of a local coordinate system at the crack tip

$$J = \int_{\Gamma} (\Psi \, \mathrm{d}y - t_i u_{i,x} \, \mathrm{d}s) \tag{3.7}$$

with the tractions t_i on the contour Γ. Using this formulation, the J-integral equals the energy release rate in equation (3.5). Thus, J may also be written as

$$J = \frac{1-\nu^2}{E}(K_I^2 + K_{II}^2) + \frac{1+\nu}{E} K_{III}^2. \tag{3.8}$$

However, the path independence of J is restricted to traction free crack surfaces as well as to planar cracks with a straight crack front.
For further details concerning crack propagation see (5; 50; 73; 84; 93).

3.2 Cracks on Different Length Scales

Fracture may be considered on different scales. Domains including a lot of small cracks can be analyzed as a micro model including the cracks within a framework of continuum mechanics. The fact that these different length scales have to be considered in engineering parts is shown in literature as well as in recent experiments. If cracks get close to each other, they interact, i.e. crack shielding and crack amplification occurs. This is the case if the cracks are of different length scales, as well. Therefore, it is important that small cracks in the vicinity of a main crack are considered.

3.2.1 Earlier Studies about the Interaction of Cracks

In recent research, experiments with cracks in brittle materials, such as ceramics, and experiments about the interaction of cracks are presented as well as analytical solutions. In 1981 WU *et al.* used X-ray micro radiography and a scanning electron microscope to visualize micro cracking around a main crack. The effects of the micro structure on the crack

propagation behavior in ceramics (158) were analyzed. They figured out that micro cracks nucleate around the main crack front.
Analytical results for crack interaction were developed for 2D problems in 1986. RUBINSTEIN (131) analyzed the influence of microdefects near a crack tip on the stress intensity factors. Microdefects may influence the crack propagation direction or lead to crack arrest. ROSE (130) analyzed the effect of micro cracks on main cracks, while he used a point source representation for each micro crack. Analytical solutions for arbitrary crack arrangements in 3D are not available yet. FABRIKANT developed integral equations for coplanar penny-shaped cracks in 1987 (51). However, to solve these analytical solutions an iterative procedure to compute the results of the integral equations was necessary. The interaction of arbitrary penny-shaped cracks also modeled as main and micro cracks was analyzed by KACHANOV AND LAURES in 1989. To solve the problem with multiple cracks, a decomposition into subproblems concerning only one crack was performed (88). Additionally, HUANG AND KARIHALOO (82) modeled 3D crack problems, with restrictions to mode I. The publication of TAMUZS (147) is a review paper about crack shielding and amplification effects with many references.
Analytical solutions for fracture mechanics for arbitrary crack geometries and locations are not available in general 2D cases, even less in 3D. Therefore, numerical methods to analyze fracture mechanics problems need to be applied.

3.2.2 Recent Experimental Results

Recently, the nucleation and propagation of micro cracks in the vicinity of a macro crack within a ceramics material could be observed by bending experiments in a scanning electron microscope (Institute of Materials Science, Leibniz Universität Hannover, Germany). The Institute of Materials Science provides the pictures resulting of the experiments. These pictures are shown in this thesis as well as on the cover. The material data of the magnesium-stabilized zirconia Z-507, $MgZrO_2$, is given in table 3.2.

density	average grain size	Vickers hardness	compressive strength
5.7 $\mathrm{g/cm^3}$	50 μm	1200 $\mathrm{HV_{10}}$	1600 MPa
bending strength	fracture toughness	elastic modulus	Poisson ratio
500 MPa	7 $\mathrm{MPam^{1/2}}$	200 GPa	0.3

Table 3.2: Material Properties of Z-507.

The test specimen as shown in figure 3.5 is clamped into a μ-tensile/compression module with a three-point-bending-device, figure 3.6. The test specimen has a V-notch at the top to initiate propagation of the main crack. This V-notch is generated with a precision cut-off machine and a razor blade subsequently. The displacement of the bearing rolls of the bending machine is slowly increased, so that a force-displacement curve can be recorded. The force-displacement curves for two test specimens are illustrated in figure 3.7. They differ in the load for the nucleation of small cracks as well as in the applied displacement. This may be due to inhomogeneities of the material as well as due to non-centric clamping within the three-point-bending machine.

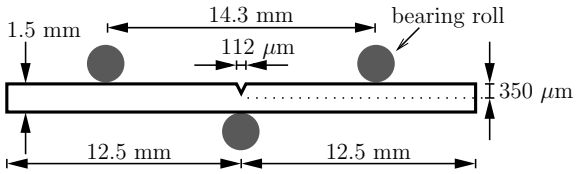

Figure 3.5: Test specimen for a three-point-bending test. The test specimen has a squared cross sectional area.

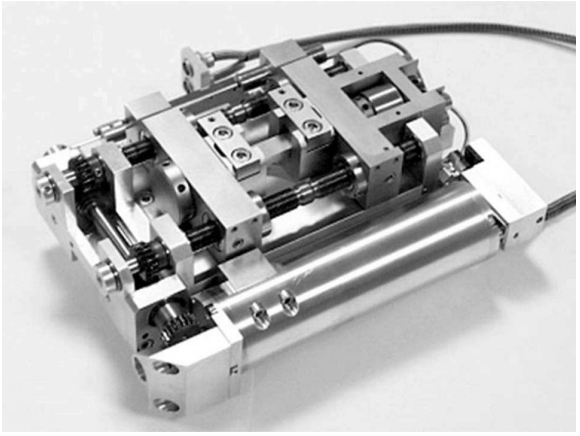

Figure 3.6: μ-tensile/compression module type Kamrath and Weiß.

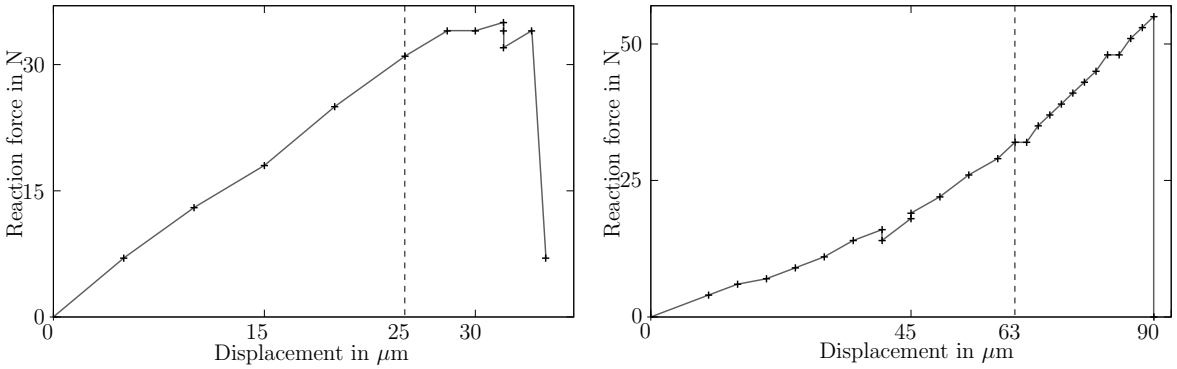

Figure 3.7: Force-displacement curves of the three-point-bending tests. The linear material behavior of Z-507 up to the point of total fracture can be seen. Cracks were initialized at a displacement of 25 μm in specimen 1 and at 63 μm in specimen 2.

At every load step, pictures are taken with the scanning electron microscope so that crack initiation and crack propagation can be seen. The results for specimen 1 are as follows: in figure 3.8, the initial main crack of a razor cut as well as grain boundaries, inclusions and holes are visible. With an increasing displacement of the bearing rolls of the bending machine, cracks of about 5-10 μm nucleate mainly along grain boundaries but also intracrystalline, displayed in figures 3.8 and 3.9. The cracks grow under further displacement until total fracture, i.e. crack propagation of the main crack, see figure 3.10.

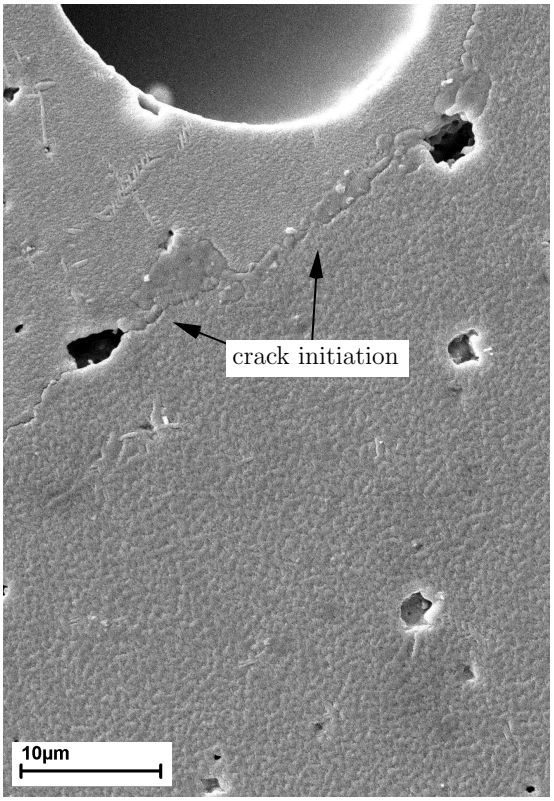

Figure 3.8: Nucleating cracks at grain boundaries. Displacement: 25 μm.

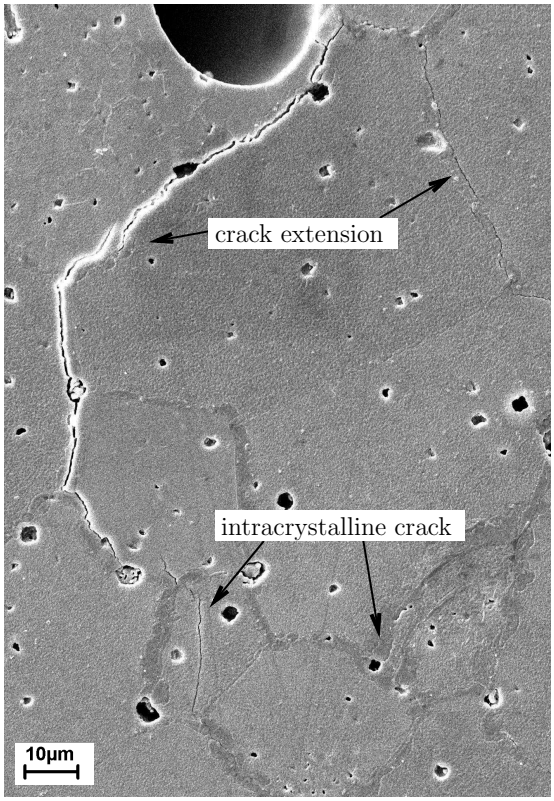

Figure 3.9: Crack propagation. Displacement: 32 μm.

Specimen 1 breaks at a total displacement of 34 μm. A closer look at the developed main crack visualizes the influence of small cracks in the vicinity of the main crack. The crack propagation at the initialized razor cut crack front is intracrystalline and does not coincide with the first nucleated smaller cracks at the grain boundaries, figure 3.10a. Also smaller cracks around the main crack, both, intracrystalline and at the grain boundaries, exist along the whole main crack, figure 3.10b and c. At the new crack front, crack branching develops, displayed in figure 3.10d.

This complex behavior of fracture cannot be described by any analytical model as they are presented in section 3.1. Therefore, numerical methods such as the finite element method should be used to analyze fracture mechanics problems. The finite element method will be introduced as well as methods to model main cracks and smaller cracks around them.

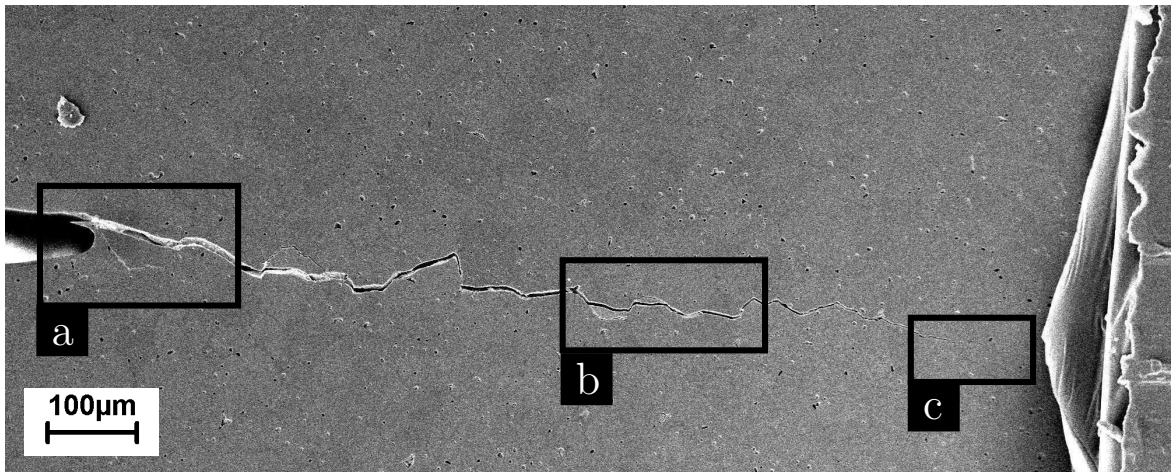

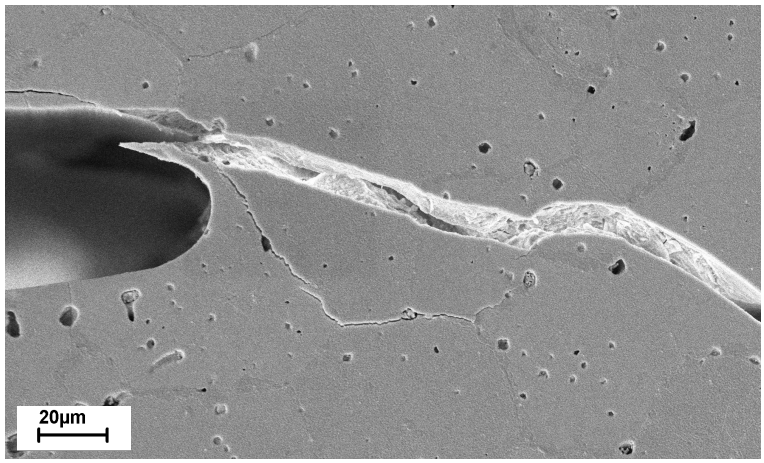

a) The main crack grows from the initialized main crack front.

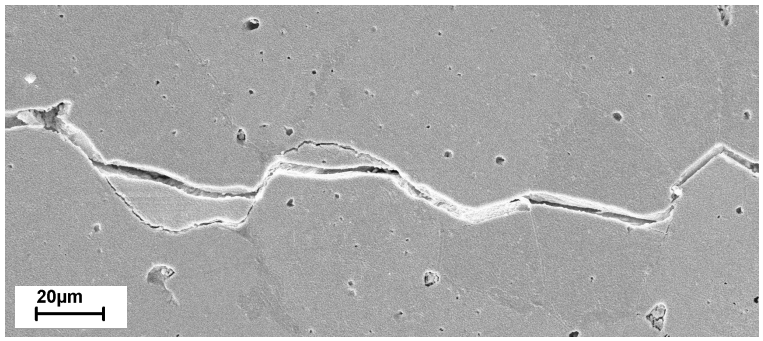

b) The main crack is intracrystalline.

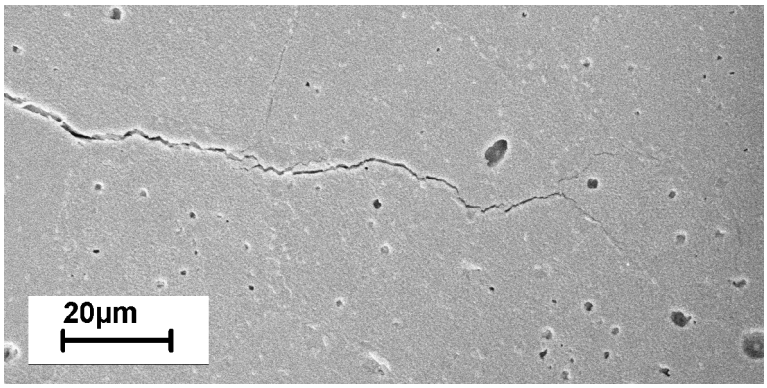

c) Crack branching at the crack front.

Figure 3.10: Total fracture of the specimen at a displacement of 34 μm. Additionally some details of the crack path are given.

Chapter 4

Finite Element Formulation

The finite element method (FEM) is a well-known method to solve systems of partial differential equations. The classical procedure to solve such systems of equations is firstly to formulate the weak form of equilibrium. There, an ansatz is made for the unknowns, i.e. the displacements in this work. Afterwards, the body is discretized with finite elements to approximate the solution. General applications for the FEM as well as details and further references can be found e.g. in (20; 83; 157; 160; 161). Here a short overview of the method is presented. Then some special applications to model cracks within the FEM are introduced. A historical overview of the FEM and its evolution is given in (161).

4.1 The Finite Element Method

For static or quasi-static processes the time independent mechanical boundary value problem consists of the strong form of the balance of linear momentum (2.11)

$$\operatorname{div}\boldsymbol{\sigma} + \boldsymbol{b} = \mathbf{0} \quad \text{in}\, \mathcal{B}$$

and displacement boundary conditions (also referred to as DIRICHLET boundary conditions) with prescribed displacements $\bar{\boldsymbol{u}}$

$$\boldsymbol{u} = \bar{\boldsymbol{u}} \quad \text{on}\, \partial\mathcal{B}_u \tag{4.1}$$

and traction boundary conditions (also referred to as NEUMANN boundary conditions) with prescribed tractions $\bar{\boldsymbol{t}}$

$$\boldsymbol{t} = \bar{\boldsymbol{t}} = \boldsymbol{\sigma} \cdot \boldsymbol{n} \quad \text{on}\, \partial\mathcal{B}_t. \tag{4.2}$$

The whole boundary is therefore split into the displacement and the traction boundary part which do not overlap

$$\partial\mathcal{B} = \partial\mathcal{B}_u \cup \partial\mathcal{B}_t \qquad \partial\mathcal{B}_u \cap \partial\mathcal{B}_t = 0. \tag{4.3}$$

For general applications, no direct solution is computable. Thus, within the FEM the balance of linear momentum and the equation for NEUMANN boundary conditions are not enforced

to be fulfilled in the strong form but reduced to zero in a weak sense, i.e. in integral form. Therefore, the equations are multiplied with a weighting function $\delta\boldsymbol{u}$ (also referred to as test function or virtual displacement function). The weighting function is chosen to be arbitrary but to fulfill the DIRICHLET boundary conditions exactly. Now the integrals on the overall domain and on the traction boundary are applied

$$\int_{\mathcal{B}} (\operatorname{div}\boldsymbol{\sigma} + \boldsymbol{b})\delta\boldsymbol{u}\,\mathrm{d}v = 0 \quad \wedge \quad \int_{\partial\mathcal{B}_t} (\bar{\boldsymbol{t}} - \boldsymbol{\sigma}\cdot\boldsymbol{n})\delta\boldsymbol{u}\,\mathrm{d}a = 0. \tag{4.4}$$

After the application of the GAUSS theorem (2.8) and partial integration the resulting weak form of equilibrium can be written as

$$\int_{\mathcal{B}} \boldsymbol{\sigma} : \operatorname{grad}\delta\boldsymbol{u}\,\mathrm{d}v - \int_{\mathcal{B}} \boldsymbol{b}\cdot\delta\boldsymbol{u}\,\mathrm{d}v - \int_{\partial\mathcal{B}_t} \bar{\boldsymbol{t}}\cdot\delta\boldsymbol{u}\,\mathrm{d}a = 0. \tag{4.5}$$

As the solution space of the weak form of equilibrium is not known for every material point, an ansatz for the displacements is made. Thus, the displacements are only computed at special points and the solution for the displacements at the points in between are interpolated via the known displacements. One possibility to define the points for which the displacements should be computed is the decomposition of the domain into finite elements e, displayed in figure 4.1. The total number of applied elements is n_e. The approximated body is the sum of all elements

$$\mathcal{B} \approx \Omega = \bigcup_{e=1}^{n_e} \Omega_e. \tag{4.6}$$

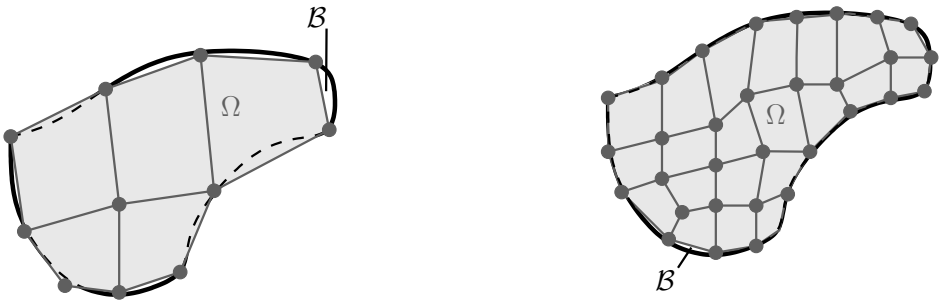

a) Coarse discretization b) Fine discretization

Figure 4.1: Approximation of the body $\mathcal{B}$ using finite elements. The finer the mesh, the better is the approximation of the geometry. A better approximation can also be reached if curved element boundaries are allowed.

The nodes of the elements are the specific points for which the solution is computed by solving equation (4.5). The ansatz for the approximated displacements $\boldsymbol{u}^h$ reads

$$\boldsymbol{u}^h = \sum_{I=1}^{n_n} N_I \boldsymbol{u}_I, \tag{4.7}$$

with n_n as the number of nodes per element and the nodal displacement $\boldsymbol{u}_I$ of node I.

The interpolation function N_I for the displacements of points within the elements is commonly chosen to be a LAGRANGian polynomial. Alternative concepts and further details to LAGRANGian finite elements can be found in (160). To define the shape functions N_I for every finite element in the same way, the isoparametric concept is introduced. Every element e of the discretized configuration of the body $\mathcal{B}$ is mapped into a reference element $\square$ of defined standard geometry and size. The results are then projected back to the original element as illustrated in figure 4.2. The reference element of a general hexahedral element typically is a cube with an edge length of 2. For such a reference element, the shape function of node I reads

$$N_I(\xi, \eta, \zeta) = \frac{1}{8}(1 + \xi_I \xi)(1 + \eta_I \eta)(1 + \zeta_I \zeta). \tag{4.8}$$

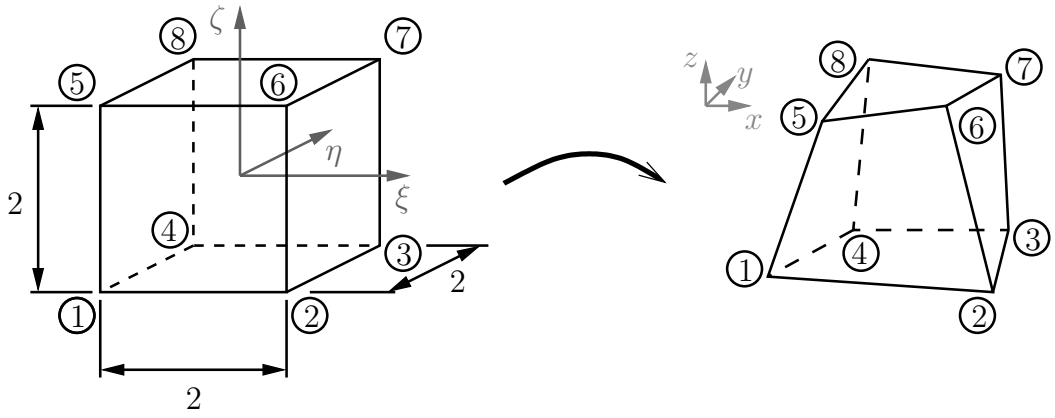

Figure 4.2: Isoparametric mapping of the reference element to a finite element.

With the BUBNOV-GALERKIN approach summarized in (53) among others, the same ansatz as for the displacements is used for the coordinates $\boldsymbol{x}$ and for the test function $\delta\boldsymbol{u}$. Applied to the weak form of equilibrium and assembling over all elements e, the discretized weak form of equilibrium is evaluated as

$$\bigcup_{e=1}^{n_e} \sum_{I=1}^{n_n} \delta \boldsymbol{u}_I^T \left[\int_{\Omega_e} \boldsymbol{B}_I^T \cdot \boldsymbol{\sigma}^h \, \mathrm{d}v - \int_{\Omega_e} N_I \cdot \boldsymbol{b}^h \, \mathrm{d}v - \int_{\partial\Omega_{et}} N_I \cdot \bar{\boldsymbol{t}}^h \, \mathrm{d}a \right] = 0, \tag{4.9}$$

with the discretized approximated stresses $\boldsymbol{\sigma}^h$ and the element quantities of the volume force $\boldsymbol{b}^h$ and the tractions $\bar{\boldsymbol{t}}^h$. The matrix $\boldsymbol{B}_I$ includes the derivatives of the shape functions according to the coordinates $\boldsymbol{x}$ to achieve the gradient operator.
The integral equation has to be fulfilled for arbitrary nodal values of $\delta\boldsymbol{u}_I$, as the weighting function is arbitrary, except the restriction that DIRICHLET boundary conditions have to be fulfilled exactly. Thereby, any term has to vanish separately and a system of generally nonlinear equations is created. In this work, the system of equations is only nonlinear for the part considering nonlinear (plastic) material behavior, cf. (133) for details. To solve this nonlinear system of equations the NEWTON-RAPHSON scheme can be used. For a historic

development cf. (32). The assumption for the nonlinear system of equations is that it is not solved exactly. Therefore, the result of the discretized weak form is not equal to zero, but equals a residual $\boldsymbol{G}(\boldsymbol{u}) = \boldsymbol{R}(\boldsymbol{u}) - \boldsymbol{P}$ which has to converge to zero during an iterative process. Here, $\boldsymbol{R}(\boldsymbol{u})$ is the vector of inner nodal forces and $-\boldsymbol{P}$ the load vector

$$\boldsymbol{R}(\boldsymbol{u}) = \bigcup_{e=1}^{n_e} \sum_{I=1}^{n_n} \left[\int_{\Omega_e} \boldsymbol{B}_I^T \cdot \boldsymbol{\sigma}^h \, \mathrm{d}\Omega \right] \tag{4.10}$$

$$-\boldsymbol{P} = \bigcup_{e=1}^{n_e} \sum_{I=1}^{n_n} \left[-\int_{\Omega_e} N_I \cdot \boldsymbol{b}^h \, \mathrm{d}\Omega - \int_{\partial\Omega_{et}} N_I \cdot \bar{\boldsymbol{t}}^h \, \mathrm{d}\partial\Omega_t \right]. \tag{4.11}$$

With a first-order TAYLOR series approximation for $\boldsymbol{u}$ a linear system of equation follows for every iteration step k, which is symmetric for hyperelastic materials if the BUBNOV-GALERKIN approach is applied

$$\left. \frac{\partial \boldsymbol{G}(\boldsymbol{u}^h)}{\partial \boldsymbol{u}^h} \right|_{\boldsymbol{u}^h = \boldsymbol{u}_k^h} \cdot \left(\boldsymbol{u}_{k+1}^h - \boldsymbol{u}_k^h \right) = -\boldsymbol{G}(\boldsymbol{u}_k^h). \tag{4.12}$$

The discretized form of the first part of (4.12) is usually referred to as the element stiffness matrix $\boldsymbol{K}^e$. The displacement vector is updated

$$\boldsymbol{u}_{k+1}^h = \boldsymbol{u}_k^h + \Delta \boldsymbol{u}^h \tag{4.13}$$

based on the incremental solution $\Delta \boldsymbol{u}^h$ of the last iteration step.
For both, the linear and the nonlinear equation system, the resulting integral formulation of the discretized weak form can usually not be solved analytically. Hence, numerical integration methods need to be used as for instance GAUSSian quadrature, summarized in (1) among others. To perform the numerical integration, the integral is first transferred to an integral over reference elements. Within each reference element, the integration points are at defined positions and do not have to be recomputed for different element shapes of the original element. The integral is then converted into a summation using GAUSSian quadrature. For an arbitrary function $\boldsymbol{f}$ the integration follows

$$\int_{\Omega} \boldsymbol{f}(\boldsymbol{x}) \, \mathrm{d}v \approx \bigcup_{e=1}^{n_e} \int_{\Omega_e} \boldsymbol{f}(\boldsymbol{x}) \, \mathrm{d}v = \bigcup_{e=1}^{n_e} \int_{\Omega_\square} \boldsymbol{f}(\boldsymbol{\xi}) \det \boldsymbol{J}_e \, \mathrm{d}v \approx \bigcup_{e=1}^{n_e} \sum_{i=1}^{n_{int}} \boldsymbol{f}(\boldsymbol{\xi}_i) \det \boldsymbol{J}_e w_i \tag{4.14}$$

with the determinant of the element JACOBIan matrix $\det \boldsymbol{J}_e$, which includes the derivatives of the coordinates $\boldsymbol{x}$ with respect to $\boldsymbol{\xi}$, the number of integration points n_{int} for one element and the weighting w_i of the integration points.

4.2 Numerical Methods for Fracture Mechanics

Applying numerical methods to fracture mechanics necessitates a special treatment. If the finite element mesh is aligned with the crack faces, special elements to represent the singularity at a crack front have to be chosen. Apart from the finite element methods other

numerical methods such as the boundary element method or meshless approaches like the element free GALERKIN method or the *h-p* cloud method can also be applied to solution processes including fracture. Furthermore, extensions of the FEM to model fracture within finite elements and thus independent of the mesh geometry are developed, i.e. enriched finite elements with additional degrees of freedom, damage models, phase-field models among others. Firstly, different methods with the finite element boundaries aligned with the crack are discussed. Thereafter, methods besides the application of finite elements are pointed out. Finally, methods with a mesh independent of existing cracks are assessed in the context of fracture mechanics.

Numerical methods to model cracks aligned with finite element boundaries

For the FE mesh aligned with the crack faces, the crack surfaces can be seen as a boundary of the body with zero traction. Thus, in the initial pre-cracked state with a closed crack, element nodes are at the same position on both sides of the crack surfaces. To reflect the stress singularity at the crack front, elements next to the crack front are often modified. After the analytical analysis of the stress singularities around the crack front (86; 155), special finite elements which include the stress singularity description emerged in the 1970s. These special crack tip elements, which include the singular field and as additional unknown variables the stress intensity factors, are presented in (26; 149) among others. Modified displacement descriptions are applied in these crack elements. These elements are not compatible with elements with LAGRANG shape functions and they cannot represent rigid body motions. Thus, in further studies two other types of special crack elements were devised, namely hybrid crack elements and quarter point elements. The hybrid elements, cf. e.g. (6; 153), do not include the continuity of the displacements a priori. Therefore, the stiffness matrix of the system is enlarged with additional unknowns, namely the stress intensity factors. The crack elements are compatible to the surrounding finite elements and can reflect rigid body motions as well. On the other hand, quarter point elements as presented in (15; 16; 78) among others are modifications of serendipity elements, i.e. elements with midside nodes at the element edges but without center nodes. The midside nodes next to the crack front are moved to the quarter position next to the crack front. Hence, the analytically required singularity at the crack front can be obtained. Developments to model ideal plastic material behavior are presented in (16). Common for all mentioned methods is a refined mesh around the crack front necessary to represent the stress behavior in a correct manner. Thus, in case of crack propagation, remeshing is required. This is one of the most important disadvantages of such methods.

Another method with the crack path restricted to the FE mesh is the application of cohesive zones. Interfacial cohesive elements are introduced and can represent the debonding effect within the material. The basis for the cohesive zone model was laid in the 1960s (13; 48) and further developments and experiences have been gained until now, cf. e.g. (120; 159). The main drawback of the application of the cohesive zone model in its original description is the restriction to crack propagation along element edges in 2D and element surfaces in 3D within the interfacial elements.

Numerical methods for fracture mechanics besides the FEM

A method similar to the FEM is the boundary integral equation method (37; 102). This method considers only the boundary of the domain. Thus, the domain integrals are transferred to boundary integrals which are solved numerically analogously to GREEN's boundary formula in potential energy. Considering cracks, singular equations occur. This problem can be solved either by modeling the crack by a gap with a rounded closure or by replacing one crack by a boundary with special traction and displacement conditions (36). The boundary integral equation method leads in general to non-symmetric and fully populated systems of equations which can only be solved in an acceptable time with special solution algorithms. Nevertheless, the main drawback of the boundary integral equation method is the poor extensibility regarding large deformations or inelastic material behavior. Further methods for fracture mechanics besides the FEM are e.g. the element-free GALERKIN method (EFGM) or the *h-p* cloud method, which belong both to meshless methods. For the EFGM (22) nodes at the boundary as well as in the interior of a body are introduced. For the trial and test functions at each node moving least squares (MLS) functions are applied. Around each node a domain of influence is needed to achieve the MLS parameters. The influence of the domain radius is studied e.g. in (22). The main advantage of the EFGM is that no mesh is needed and therefore no mesh refinement has to be applied, if a concentration of nodes is needed in the vicinity of e.g. cracks or other regions where steep gradients are expected. Additionally, the field variables as well as their gradients are smooth within the domain. Disadvantages are the necessity of an algorithm to detect all neighboring relations for the MLS fitting and the necessity of an underlying mesh for integration purposes. Furthermore, the DIRICHLET boundary conditions are not fulfilled exactly *a priori*. Thus, LAGRANGE multipliers have to be introduced to enforce the essential boundary conditions. A further meshfree method based on the EFGM is the *h-p* cloud method of DUARTE AND ODEN (42). Within this method, the polynomial functions are extended to radial basis functions of varying size supports. Thus, the class of functions is more general. This method has a higher convergence rate than classical *h-p* adaptive FE simulations, but the same drawbacks as for the EFGM occur. A review to meshless methods apart from fracture mechanics is given in (41; 56).

Numerical methods which extend the FEM for a mesh independent of cracks

During the 1990s, different extensions to the FEM emerged. These methods allow for a mesh description independent of the crack geometry. In this category, two different types arose. The first type models the mesh independent of the crack with special finite elements, which may include different constitutive equations. The second type uses additional enrichments of nodes. There, degrees of freedom are added directly at some nodes of the finite element mesh.

The strong discontinuity approach of 1993 (134; 116; 117) belongs to the first type. Here, a strain softening effect has to be included in the constitutive equations as well as strong discontinuity kinematics have to be considered. Thus, a jump in the displacement field can be realized with the aid of the HEAVISIDE function. The strong discontinuity approach leads to a crack without dependencies on the mesh size or some mesh alignment, but the crack cannot

end within one element and the singularities at the crack front cannot be represented. Thus, this method is moderately convenient for fracture analysis, which should focus on an accurate stress representation at the crack front. Especially in the case with a discretization based on error estimation techniques the accuracy of the solution is quite important. Moreover, a crack front which cannot end within one element may lead to mesh dependent crack front behavior if the front is curved in a 3D analysis.

Another method of the first type is a damage model, which is a method already considered within discussions to the strong discontinuity approach and which may be considered therein (116). A gradient damage model in one possible description includes continuum damage mechanics within the framework of virtual power (55). The assumption that the power of internal forces depends on the damage rate is underlying. Thereby, the damage rate is correlated to microscopic movements and the gradient of the damage rate is correlated to interactions on the microscale. If the scalar damage variable D, which can be seen as a stiffness reduction factor, is equal to one, the material is defined to be totally damaged. Thus, total fracture as well as cracks can be modeled with this method. The fracture is then independent of the mesh size and also of the orientation of the mesh (121).

A third method using an additional system matrix is a phase-field model (89; 107). The balance of the quasi-static stress equilibrium and a gradient-type phase-field evolution in the argument of virtual power are coupled. The scalar phase-field variable Φ in the context of fracture mechanics is re-interpreted as a phenomenological measure of damage. The scalar field is then used to distinguish between broken and non-broken behavior which is coupled to the displacements. With the application of a scalar crack phase-field a diffuse crack modeling is realizable. A decrease of the length scale for the evolution of Φ enables the representation of sharp crack geometries. Due to a local model crack branching as well as complex crack paths can be realized easily. The main drawback of this phase-field model is the required mesh density for the resolution of diffuse crack patterns (107).

The second type for the FE mesh independent of cracks makes use of enrichments of nodes introducing additional degrees of freedom. The basic theory is in this case the partition of unity method (PUM) (9). Approximation spaces with a priori known aspects of the solution are added to the finite element solution space. Thus, re-entrant corners, cracks, heterogeneities, contact formulations, fluid structure interactions among others can be modeled using the FEM, but without geometric restrictions to the FE mesh based on special solution properties. Two basic methods are the generalized finite element method (GFEM) and the extended finite element method (XFEM). Both combine the FEM and the PUM. The GFEM (141; 142) enriches nodes with additional functions detected during the simulation, while in the XFEM (18; 110), the a priori known solution space has to be given by the user. Thus, the enrichment functions are specified in advance. Some applications besides fracture for GFEM/XFEM are dislocations (69), holes and inclusions (144), solidification (34), the application to grain boundaries (23; 135), the application to phase interfaces (35) or to multi-field problems (163) among others. Enlarged overviews to these and further applications including theoretical details are given in (19; 59). During the last years the GFEM and the XFEM have approached.

Summing up, for linear elastic fracture mechanics and small deformations, the damage model as well as the phase-field model introduce additional equations which lead to a non-

symmetric and non-linear system of equations. The GFEM and the XFEM also introduce additional equations, but the system of equations stays symmetric and linear. Therefore, the XFEM is chosen in this work to model cracks within the FEM.

4.3 The Extended Finite Element Method

The XFEM includes a priori known solution properties such as stress singularities around crack fronts. The XFEM for cracks was first introduced by BELYTSCHKO *et al.* in 1999 (18; 110). Since then the method has proven to be a well-known method to model cracks within the context of linear elastic fracture mechanics as well as for further applications. The method will be described for small deformations. As shown in (96) for 2D and in (100) for 2D and 3D the influence of large deformations in the context of elastic fracture mechanics is negligible. In the case of large deformations other aspects as e.g. inelastic material behavior should be considered to retain the right assumptions.
For cracks, a local partition of unity is introduced. Local means here, that only some nodes, those around the crack, are enriched, cf. e.g. figure 4.3. Each enrichment is coupled with the introduction of additional degrees of freedom. Every node belonging to an element con-

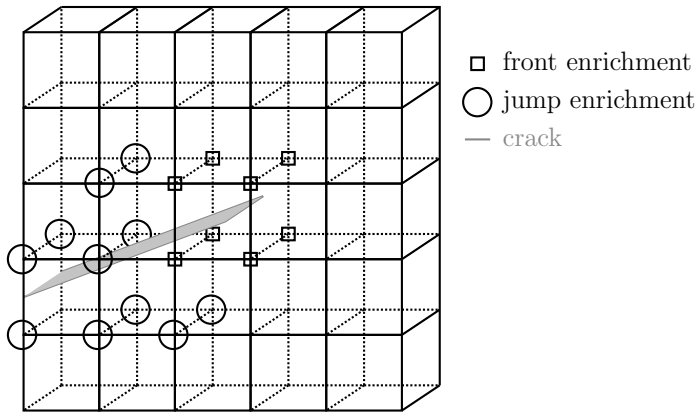

Figure 4.3: Enrichment scheme for the XFEM.

taining the crack front or part of it is enriched with front enrichment functions and belongs to the node set $S_2 \subseteq S_1$ where the set S_1 includes the total number of nodes n_n. The node set S_2 includes the number of n_K nodes. All nodes belonging to a cut element and not to the node set S_2 belong to the number of n_J jump enriched nodes, summarized in the node set $S_3 \subseteq S_1 \setminus S_2$. Due to the enrichments, additional degrees of freedom are introduced. Thus, the vector of unknowns is enlarged, which leads to a new formulation for the displacement field. The extended discretized displacement field reads

$$\begin{aligned}\boldsymbol{u}^h(\boldsymbol{x}) &= \sum_{I=1}^{n_n} N_I(\boldsymbol{x})\boldsymbol{u}_I + \sum_{J=1}^{n_J} N_J(\boldsymbol{x})H(\boldsymbol{x})\boldsymbol{b}_J + \sum_{K=1}^{n_K} N_K(\boldsymbol{x})\left(\sum_{M=1}^{4} f_M(\boldsymbol{x})\boldsymbol{a}_{KM}\right) \\ &= \sum_{I=1}^{n_n} \hat{N}_I \hat{\boldsymbol{u}}_I. \end{aligned} \tag{4.15}$$

N_J and N_K form a partition of unity as already mentioned. They are chosen to build the same partition of unity as N_I but also other shape functions are possible. $\boldsymbol{b}_J$ and $\boldsymbol{a}_{KM}$ are additional degrees of freedom belonging to the enrichments. Thus, the degrees of freedom $\boldsymbol{u}_I$ of an enriched node do no longer have the physical meaning of displacements for the presented type of XFEM. $f_M(\boldsymbol{x})$ are crack tip enrichment functions representing the first order asymptotic solution at a crack tip for 2D problems, cf. equation (3.1) and table 3.1. The functions are known as WESTERGAARD functions (155) or as the asymptotic solution field of WILLIAMS (156). The derivatives of these functions are singular so that the singular behavior in the strain and stress fields can be achieved. The four functions can be written as

$$\begin{aligned}\boldsymbol{f}(\boldsymbol{x}) &= \boldsymbol{f}(r,\varphi) \\ &= \sqrt{r}\left\{\sin\left(\frac{\varphi}{2}\right), \cos\left(\frac{\varphi}{2}\right), \sin\left(\frac{\varphi}{2}\right)\sin(\varphi), \cos\left(\frac{\varphi}{2}\right)\sin(\varphi)\right\}\end{aligned} \tag{4.16}$$

with the local polar coordinates r and φ of a coordinate system located at the crack tip as shown in figure 4.4. The four functions are illustrated in figure 4.5 for a 2D reference ele-

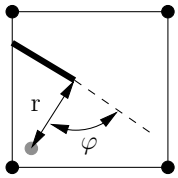

Figure 4.4: Definition of local polar coordinates r and φ at a crack tip.

ment. The first function of $\boldsymbol{f}(r,\varphi)$ is discontinuous along the crack faces and thus important to reflect crack opening. Of course, the crack tip functions represent the behavior at a crack tip in a 2D environment. An extension to 3D is given by SUKUMAR *et al.* (145). Following them, the 2D crack tip functions are applicable to the 3D case if the plane with the crack tip functions is moved along the line of the crack front. Hence, they are entitled front enrichments. H in equation (4.15) is the modified HEAVISIDE function which is 1 at one side of the crack and the crack surface and -1 on the other side of the crack and is applied further away from the crack front (110). The function H is also known as a step function and introduces a strong discontinuity in the solution. The combination of the application of the

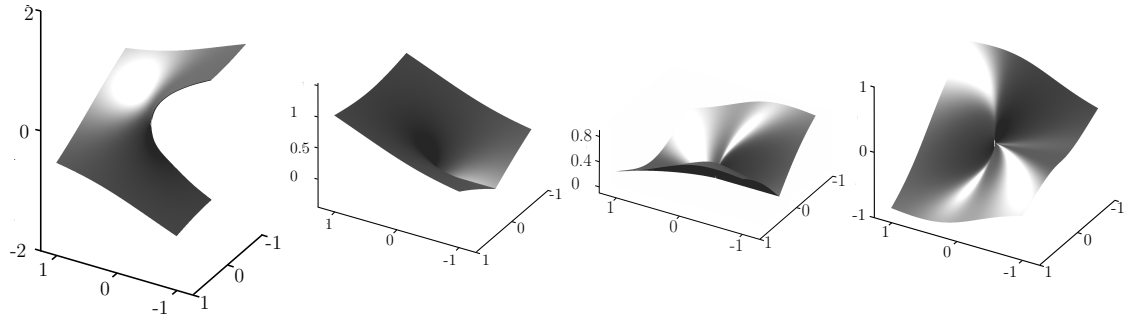

a) $\sqrt{r}\sin\left(\frac{\varphi}{2}\right)$ b) $\sqrt{r}\cos\left(\frac{\varphi}{2}\right)$ c) $\sqrt{r}\sin\left(\frac{\varphi}{2}\right)\sin(\varphi)$ d) $\sqrt{r}\cos\left(\frac{\varphi}{2}\right)\sin(\varphi)$

Figure 4.5: The four functions of the WESTERGAARD solution field plotted for a 2D reference element.

front enrichment together with the step function was first used by MOËS *et al.* (110) and is nowadays standard for XFEM simulations.
To determine the position of cracks within elements, different descriptions for crack representation exist. One possibility is the use of direct polynomial description as in the first XFEM papers (18; 110). This representation type is restricted to simple polynomial descriptions. A more flexible formulation is the application of non-uniform rational B-splines (25) which is a rather new method. Both methods are explicit crack descriptions. With explicit crack descriptions the accuracy of the crack path is independent of the discretization size although the evaluation of the crack path within the elements may be complicated. A common implicit way to represent cracks is the application of signed distance functions, i.e. level sets (23; 111; 140). For the crack representation of a single crack two signed distance functions are sufficient. These functions are referred to as level set functions. The first level set function Ψ represents the distance to the crack surface and the second level set function Θ the distance to the crack front, respectively. The two functions are perpendicular to each other and plotted in figure 4.6 for a planar crack with a straight crack front. The values of

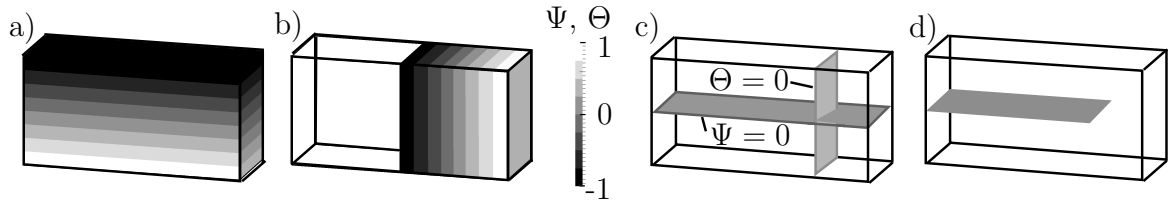

Figure 4.6: Representation of the level set functions Ψ (a) and Θ (b) required for the description of a crack. c) Planes with $\Psi = 0$ and $\Theta = 0$. d) Resulting plane crack. The crack front is the line where both level set functions equal zero.

the level sets are stored at the FE nodes and interpolated within each element using the same shape functions as for the displacement, coordinate and weighting function interpolation. The interpolation of the level sets in one element with the nodal level set values Ψ_I, Θ_I reads

$$\begin{pmatrix} \Psi_e^h \\ \Theta_e^h \end{pmatrix} = \sum_{I=1}^{n_{en}} N_I(\boldsymbol{x}) \begin{pmatrix} \Psi_I \\ \Theta_I \end{pmatrix}. \tag{4.17}$$

Using level sets, the step function H can be evaluated at each integration point easily

$$H(\boldsymbol{x}) = \begin{cases} 1 & : \quad \Psi(\boldsymbol{x}) \geq 0 \\ -1 & : \quad \Psi(\boldsymbol{x}) < 0 \end{cases}. \tag{4.18}$$

Additionally, the distance r and the angle φ to the crack front can be obtained if the level sets are known. Their evaluation reads

$$r = \sqrt{\Psi^2 + \Theta^2} \qquad \varphi = \arctan\left(\frac{\Psi}{\Theta}\right). \tag{4.19}$$

Using the WESTERGAARD enrichment functions together with the level set method, the XFEM enables the inclusion of the stress singularity resulting of a crack within finite elements. There are some main aspects which have to be analyzed to decide whether the XFEM is a useful method leading to reasonable results and efficient simulations. Some of these aspects are the numerical integration and the convergence of the results for refined meshes.

4.3.1 Accuracy and Convergence Rate of the XFEM

A convergence study for problems solved with the XFEM is given by LABORDE *et al.* in (94) and by BÉCHET *et al.* (17). The rate of convergence in the global energy norm is given as $\mathcal{O}$ depending on the mesh parameter h. The mesh parameter describes the element edge length of a regular mesh with uniform element size. An optimal rate of convergence for a problem including a singularity is of order $\mathcal{O}(\sqrt{h})$. The rate of convergence cannot be increased to the rate of convergence for smooth problems solved with the standard FEM just by applying the XFEM. But, if additionally the integration scheme at the crack front is modified to capture the singularity and a fixed area for the front enrichment is used, the rate of convergence can be improved and nearly reach the optimal rate of order $\mathcal{O}(h^k)$, with k as the polynomial order of the shape functions (17; 94).

Quadrature aspects

As already mentioned, the integrals within the weak form of equilibrium (4.9) are usually approximated with a quadrature scheme. For the XFEM the integrands of the weak form are generally non-polynomial but singular or discontinuous within an element. Thus, the GAUSSian quadrature, which is able to solve polynomials exactly, does not lead to the exact solution anymore. Different possibilities to solve the integral equations are developed. Especially for crack front elements the treatment of the integration is quite different and influences the convergence rate.

For integration purposes the elements may be subdivided into cells. The integrands for these subcells are then usually continuous and differentiable. Within these subcells either GAUSSian integration schemes may be used (see (18; 110; 145) or (141) for the GFEM) as well as an improved solution using almost polar integration (94) or the application of a mapping algorithm from triangular subcells to reference squares (17). In these methods the subcells are aligned with the crack surfaces. A robust and fast integration method using the subcells, is the application of GAUSSian quadrature in each subcell as proposed by MOËS *et al.* (110) for 2D and by SUKUMAR *et al.* (145) for 3D. More accurate results are achieved with the methods of BÉCHET *et al.* (17) or LABORDE *et al.* (94). With their integration methods the singularity can be approximated more accurately. A method which does not restrict the subcells to be aligned with the crack surfaces is the adaptive subcell integration scheme of GANDER AND GAUTSCHI (61). The subcells are divided into further smaller subcells until an integration error tolerance is reached for each subdomain. To accomplish this method, two different integration schemes have to be applied for each subcell, their difference is compared to reach the given tolerance. The disadvantage of this method is that the tolerance has to be adopted for each problem otherwise it may happen that no solution beneath the given tolerance can be reached.

A method without subcell generation was devised by VENTURA in 2006 (151). He split each element stiffness matrix into parts with continuous and differentiable functions and parts with piecewise continuous and differentiable functions. The piecewise continuous functions are then replaced by equivalent polynomials. The polynomials are able to represent the location of the discontinuity in the element. Thus, no subcell structure has to be applied but the same results can be obtained. However, the presented technique is restricted to crack descriptions

with straight lines (2D) or planar surfaces (3D) in the reference element.

For 2D XFEM fracture mechanics simulations a possibility to transform the domain integral into a contour integral exists, cf. VENTURA 2009, (152). This method is effective for singular integrands since then the numerical quadrature is relatively far from the singularity. This method cannot be extended to 3D since the resulting surface integral would still include the singularity.

A different approach was proposed by DUFFY in 1982. The DUFFY integral (44) leads to improved accuracy for singularities of order $1/r$. Using a generalization, the accuracy for $1/\sqrt{r}$ singularities with r as the distance of the integration point to the crack front, cf. figure 4.4, can be improved. This method is applied by MOUSAVI AND SUKUMAR in 2010 (113) for piecewise polynomials within finite elements that are intersected by kinked cracks. The method works for 2D as described in the following. The elements, which include a singularity, have to be subdivided into triangles which have the singularity at one vertex of each triangle. These triangles are mapped to standard triangles for which the generalized DUFFY transformation, i.e. the transformation to a unit square, is applied. Thus, a smooth function without a singularity is obtained, which can be integrated with a standard GAUSS quadrature rule. For further details cf. (113). As a disadvantage it can be mentioned that for ill-shaped triangles the accuracy of the generalized DUFFY transformation is reduced. An extension of the DUFFY transformation to 3D problems with a distinction if the subtetrahedron has the singularity at a vertex or an element edge is given recently by MINNEBO (108). There, an overview of the different convergence rates in relation to the computational time is given as well.

Furthermore the convergence rate related to the quadrature depends on the enrichment scheme. It can be distinguished between so called “topological” and “geometrical” enrichment. Topological enrichment means that only the nodes of the elements directly cut or semi-cut are enriched. Geometrical enrichment is the enrichment with front enrichments within a fixed domain around the crack front during mesh refinement. Further away from the crack front, the front enrichment functions behave in a smooth and nearly constant way, which can lead to linear dependencies of the non-enriched and enriched degrees of freedom. The worse condition number for geometrical enrichment is shown in 2005 (17; 94). Additionally to the worse condition number, the geometrical enrichment leads to a larger number of degrees of freedom which enlarges the global system of equations drastically. In (17) the global error for different types of enrichments is shown as well. In contrast to simulation results without an enrichment, the global error can be decreased for the XFEM with topological enrichment . However, the rate of convergence does only improve for geometrical enrichment. Nevertheless, a further drawback of a geometrical enrichment arises if multiple cracks are considered, especially if crack propagation in a domain with multiple cracks is considered. The enriched domains are usually not allowed to overlap to ensure a unique identification to which crack an enrichment belongs. Thus, the best enrichment to realize crack propagation with the possibility of crack coalescence would be an enrichment which has only an influence in the elements cut or semi-cut. An idea for such a solution is given in (30; 80) for 2D and in (62) for 3D.

Within this work the robust and efficient integration scheme of the group of BELYTSCHKO is used (110; 145) with slight modifications for the construction of the subcells, see LOEHNERT

et al. (100). As enrichment scheme the topological enrichment is chosen, because it avoids problems like high condition numbers (17; 94). Hence, the optimal rate of convergence is of order $\mathcal{O}(\sqrt{h})$ as it is typically for FEM problems including a singularity.

Problems in blending elements

The partition of unity should be fulfilled in the overall domain. However, due to the local enrichment, a lack of the partition of unity exists in the elements with some enriched and some non-enriched nodes. Regarding the types of enrichments, two types of these elements exist. One type pertains to elements with non-enriched and jump enriched nodes. As the jump enrichment is a constant function in the surrounding elements, the constant value can be reproduced by the standard element shape functions. Therefore, no problems concerning the partition of unity in that type of elements exist, if the shape functions used for H are of the same degree as the shape functions used for the standard degrees of freedom (94). All nodes of one element are summarized in the set S_4. Elements with some front enriched nodes and some non-enriched or jump enriched nodes, i.e. with

$$S_4 \cap S_2 \neq S_4 \quad \wedge \quad S_4 \cap S_2 \neq \emptyset \tag{4.20}$$

are referred to as blending elements belonging to Ω_B. Within these elements the partition of unity is not fulfilled:

$$\sum_{I=1}^{n_{en}} N_I(\boldsymbol{x}) \neq 1 \quad \text{for } \boldsymbol{x} \in \Omega_B. \tag{4.21}$$

This lack of partition of unity leads to several problems such as spurious displacement jumps along element edges. Especially regarding error estimation processes, the fulfilling of the partition of unity in the overall domain is quite important. The significance of the error in the blending elements is shown in (35; 144). This error leads to a reduction of the convergence rate (35; 94; 57). Thus, for an improvement of the rate of convergence the error within the blending elements has to be reduced. One possibility is the introduction of special enhanced strain elements as done by CHESSA *et al.* (35). Thereby, additional shape functions for the enhanced strain part in the blending elements are necessary. The determination of the shape functions is difficult and they have to be constructed for each type of enrichment. Another possibility is the discontinuous GALERKIN method as proposed by GRACIE *et al.* (70). They split the domain into enriched and non-enriched patches and enforced the continuity conditions between the patches with an interior penalty method. Thus, local patches are fully enriched and no blending elements occur. However, with the application of the penalty method the continuity between the patches is only enforced in a weak sense. Nevertheless, this approach is better applicable to different types of enrichments as the method of CHESSA *et al.*. A method which proceeds similarly to that of GRACIE *et al.* (70) is proposed by LABORDE *et al.* (94). There, the domain is subdivided into an enriched and a non-enriched domain which overlap. The method is called pointwise matching XFEM and leads to optimal convergence rates but with non-conforming finite elements in the overlapping domain. For the application of higher order elements, LEGAY *et al.* figgured out that the problems in the

blending elements can be reduced if the shape functions premultiplied with the enrichments are of one order less than the shape functions used for the displacements (95). Another version of the XFEM, namely the intrinsic XFEM (58), has no additional unknowns and thus gets rid of the blending elements. However, within the intrinsic XFEM mesh based moving least squares are constructed near discontinuities to construct new shape functions. These shape functions are evaluated for subdomains of the entire domain. Thus a coupling between the domains is necessary.
A further possibility to reduce the error within the blending elements and to fulfill the partition of unity in the overall domain is the corrected XFEM introduced by LABORDE *et al.* in 2005 (94) in the context of quadrature within the XFEM, more detailed by FRIES in 2008 (57) with a convergence study. Both (57; 94) enrich all nodes $n_K^*$of the blending elements. Thus, the partition of unity is fulfilled in those elements. A ramp function $R(\boldsymbol{x})$ is introduced. The ramp function holds true $R_K = 1$ at the original front enriched nodes belonging to S_2 and $R_K = 0$ for the additional enriched nodes. Thus, the ramp function does not touch the enrichment functions in the crack front elements. Additionally, $R_K = 0$ at the additional front enriched nodes leads to a fulfilled partition of unity in the elements which have only some front enriched nodes. In consequence, the partition of unity is fulfilled in the overall domain. The enrichment scheme is sketched in figure 4.7. With these assumptions the ramp

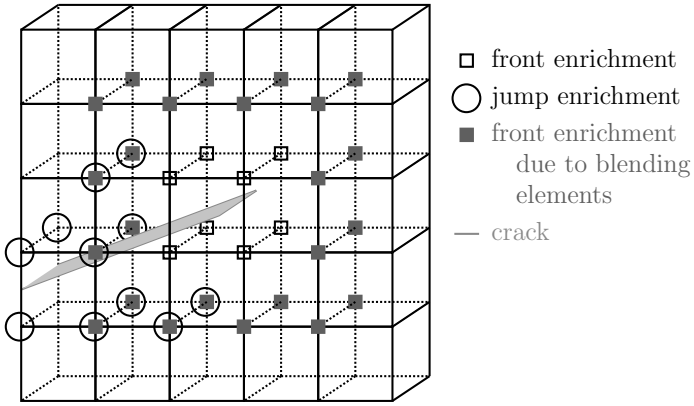

Figure 4.7: Enrichment scheme if the corrected XFEM of FRIES (57) is applied.

function is a linearly decreasing weight function which is interpolated using LAGRANGian shape functions

$$R(\boldsymbol{x}) = \sum_{K=1}^{n_K^*} N_K(\boldsymbol{x}) R_K. \tag{4.22}$$

Following FRIES (57), the application of the ramp function to the standard XFEM with the WESTERGAARD functions used for the front enrichment, leads to a singular system of equations even if the WESTERGAARD functions themselves are linearly independent. In 2D the linear dependent equations can be identified in the global system of equations and thus, these equations can be dropped. For 3D problems, as the geometry gets more complex, this is not straight forward as pointed out by LOEHNERT *et al.* in (100). They extended the corrected XFEM to 3D and tried different enrichment functions to get rid of the problem of a singular global system of equations which is even worse in the 3D case. It turned out that

the exclusion of the fourth branch function leads to the best results for the corrected XFEM (100). Especially in 3D, dropping of the fourth enrichment function is supposed to be of less significance compared to using all four enrichment functions only for special cases, as the four enrichment functions lead to the analytic solution. In (152) an overview about the handling of blending elements is given as well as a further approach is proposed. The method is called the weighted XFEM and uses a ramp function over a domain of some element layers going to zero. This method requires a larger domain of front enrichments around the crack front. Within the front enriched domain the results are influenced in accuracy due to the ramp function.
Within this work it is important that the partition of unity is fulfilled in the overall domain as error estimation techniques are applied. Additionally, a small domain of enrichments around each crack is desired. Thus, the corrected XFEM approach according to FRIES (57) is applied for the presented simulations, with a drop of the fourth enrichment function, otherwise mentioned.

Stabilization of barely cut elements

Special care has to be taken, if the ratio of the smaller part of the intersected element to the overall element is very small. The result is an ill-conditioning of the element matrices. Different possibilities including a slight change in the crack path or the mesh exist. Figure 4.8 shows the original crack path. Four possibilities to modify either the crack geometry directly (figures 4.8a, b) or to move a node of the mesh are shown (figures 4.8c, d). In all four cases

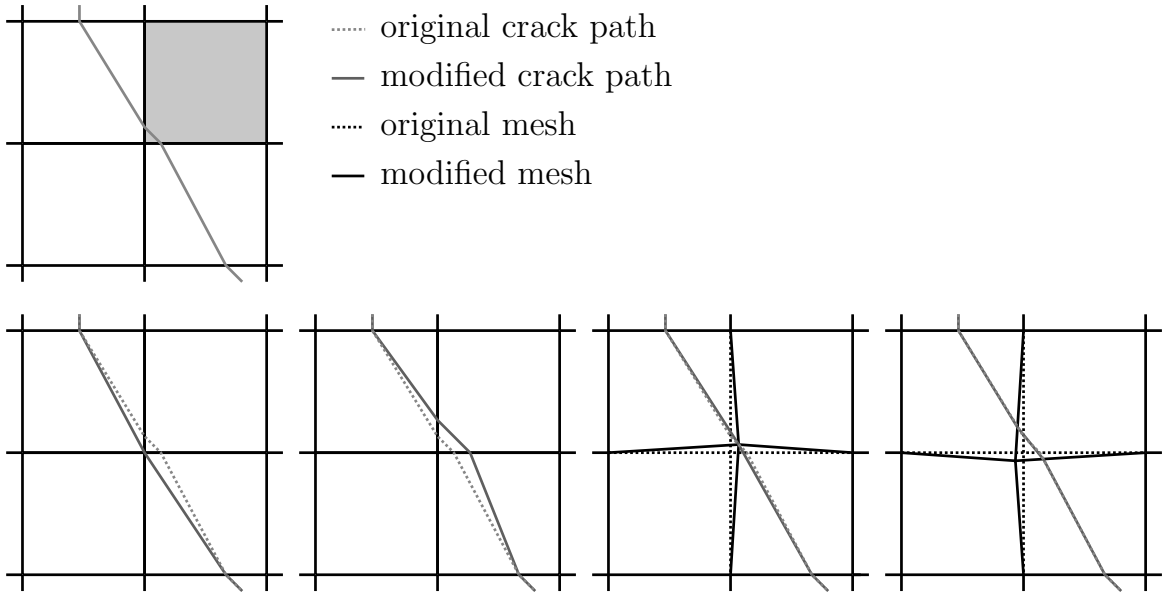

a) The crack is moved to the node.

b) The crack is moved away from the node.

c) The node is moved onto the crack.

d) The node is moved away from the crack.

Figure 4.8: Modification of the crack path or the mesh.

the crack geometry and sometimes additionally the mesh geometry are modified. The appli-

cation of these methods may lead to a different crack propagation path as the propagating path depends on the current geometry of the crack. Further problems can arise if the fracture problem is analyzed on multiple scales. Then the representation of the crack within the different scales should be the same which does not hold true for the presented scenarios. This aspect is discussed in more detail in section 5. If the possibilities of figure 4.8 are excluded to solve the problem of the ill-conditioned matrices a preconditioning or stabilization of the system of equations is required.

The problem was handled within the context of GFEM by STROUBOULIS *et al.* in 2000 (141). They directly modify the global stiffness matrix for a linear solver using a perturbation technique. Recently BABUŠKA AND BANERJEE (7) presented a stable GFEM realized by the modification of the local approximation space. For the XFEM, the first studies for preconditioners are given in (17) by BÉCHET *et al.*. They introduced a preconditioner which allows the use of standard preconditioners and iterative solvers. A local CHOLESKY decomposition is introduced which keeps the structure of the classical degrees of freedom, but only works on the enriched degrees of freedom. In 2011 MENK AND BORDAS (104) developed a preconditioning technique based on a matrix decomposition for enriched degrees of freedom. Their subdivision technique works similar to the finite element tearing and interconnecting method (FETI) where the subdomains are treated as independent structures. Within the work of MENK AND BORDAS (104) the subdomains are coupled with additional constraints as they exist only for the enriched degrees of freedom. Using the CHOLESKY decompositions for each subdomain a lower condition number of the system of equations can be reached. With this method, which is well-suited for parallel computations, the computation time can be reduced by a factor of two. Even so, it might be possible that for non-linear material behavior the preconditioner has to be updated during the computation. Within this work elasto-plastic material is considered as well. Thus, a more general preconditioning technique is desired.

Within this work, a stabilization technique for the element matrices as proposed by LOEHNERT in (97) is implemented. The idea of the stabilization will be shortly explained in the next paragraphs. Every (symmetric) element stiffness matrix $\boldsymbol{K}_e$ is analyzed with an eigenvalue decomposition

$$\boldsymbol{K}_e = \boldsymbol{V} \cdot \boldsymbol{D} \cdot \boldsymbol{V}^T \tag{4.23}$$

with the eigenvalues included in the diagonal matrix $\boldsymbol{D}$ and the contributing eigenvectors gathered column by column in $\boldsymbol{V}$. Each of those diagonal matrices includes $\bar{m}$ physically or numerically reasonable zero eigenvalues. These result due to different properties of the XFEM. Rigid body modes of standard or enriched degrees of freedom respectively lead to numerically reasonable zero eigenvalues. Further zero eigenvalues result from linear dependencies between standard and enriched degrees of freedom. Additionally, due to a multiplication with a zero ramp function, in case the corrected XFEM is used, zero eigenvalues are generated. An overview of the number of those eigenvalues is given in (97) for 2D quadrilaterals, 3D trilinear bricks and 3D quadratic tetrahedra. The eigenvectors belonging to these physically or numerically reasonable eigenvalues can be calculated directly because they only depend on the enrichment pattern and the shape of the element. But, additional m zero or nearly zero eigenvalues may exist due to e.g. cut elements with a very small ratio between

the smaller part of the intersected element and the overall element volume. The relating eigenmodes clustered in $\tilde{\boldsymbol{V}}$ need to be stabilized. For the stabilization, different substeps to separate the physically and numerically meaningful zero eigenspace of the non-physical zero eigenspace have to be implemented. First of all, the eigenvalue decomposition of the element stiffness matrix has to be split into a part corresponding to the non zero eigenvalues diagonalized in $\bar{\boldsymbol{D}}$ and the m_0 zero eigenvalues

$$\boldsymbol{K}_e = \begin{pmatrix} \bar{\boldsymbol{V}} & \boldsymbol{V}_0 \end{pmatrix} \cdot \begin{pmatrix} \bar{\boldsymbol{D}} & \boldsymbol{0} \\ \boldsymbol{0} & \boldsymbol{0} \end{pmatrix} \cdot \begin{pmatrix} \bar{\boldsymbol{V}}^T \\ \boldsymbol{V}_0^T \end{pmatrix}. \tag{4.24}$$

The $\bar{m}$ physically and numerically zero eigenmodes $\bar{\boldsymbol{v}}_0$ only depend on the element geometry and the enrichment scheme and are thus directly computable. They can be filtered out with an orthogonalization technique

$$\hat{\boldsymbol{v}}_0^i = \boldsymbol{v}_0^i - \sum_{j=1}^{\bar{m}} (\boldsymbol{v}_0^i \cdot \bar{\boldsymbol{v}}_0^j) \bar{\boldsymbol{v}}_0^j \qquad \forall \quad i \in [1, m_0] \tag{4.25}$$

followed by a normalization. Now an $\bar{m}$-fold linear dependence exists within the zero eigenspace $\hat{\boldsymbol{V}}_0$. This can be eliminated with another orthogonalization

$$\hat{\hat{\boldsymbol{v}}}_0^i = \hat{\boldsymbol{v}}_0^i - \sum_{j=1}^{i-1} (\hat{\boldsymbol{v}}_0^i \cdot \hat{\boldsymbol{v}}_0^j) \hat{\boldsymbol{v}}_0^j \qquad \forall \quad i \in [1, m_0]. \tag{4.26}$$

The vectors $\hat{\hat{\boldsymbol{v}}}_0^i \; \forall \; i \in [1, m_1]$ with $m_1 = m - \bar{m}$ span the zero eigenspace which leads to an ill-conditioning of the global stiffness matrix and thus has to be stabilized. Additionally m_2 nearly zero eigenvalues within $\bar{\boldsymbol{D}}$ may exist. If these nearly zero eigenvalues are also stabilized, the condition number of the global system of equations can be reduced drastically which leads to a reduction in computational time, see (97). The eigenvectors which need to be stabilized are

$$\tilde{\boldsymbol{V}} = \{\bar{v}_\epsilon^1, \ldots \bar{v}_\epsilon^{m_2}, \hat{\hat{v}}_0^1, \ldots, \hat{\hat{v}}_0^{m_1}\}. \tag{4.27}$$

Hence, the modified element stiffness matrix can be written as

$$\tilde{\boldsymbol{K}}_e = \boldsymbol{K}_e + \sum_{k=1}^{m} \gamma_k \tilde{\boldsymbol{v}}_k \otimes \tilde{\boldsymbol{v}}_k \tag{4.28}$$

$$\tilde{\boldsymbol{R}}_e = \boldsymbol{R}_e + \sum_{k=1}^{m} \gamma_k \tilde{\boldsymbol{v}}_k \otimes \tilde{\boldsymbol{v}}_k \cdot \boldsymbol{u}^e \tag{4.29}$$

with the stabilization factor $\gamma_k = \epsilon d_1 - d_k$ depending on an eigenvalue tolerance ϵ given by the user, but independent of the element size (d_1 is the largest eigenvalue and d_k is the eigenvalue related to the eigenvector $\tilde{\boldsymbol{v}}_k$). The influence of the eigenvalue tolerance is studied by LOEHNERT in more detail (97). The stabilization method is a robust method applicable to XFEM simulations for cracks, where a change of the crack path has to be avoided.

4.3.2 XFEM for Plasticity

Combining the XFEM for cracks with elasto-plastic material behavior necessitates a modification of the front enrichment functions. If plastic material behavior is considered, the order of the singularity induced by the crack front changes. Usually the singular stress field at the crack front indicates a non-physical behavior, which can be avoided by the application of a cohesive fracture law (see e.g. (109; 154)). A further method is the combination with plastic material behavior. ELGUEDJ *et al.* (49) developed a solution for elastoplasticity captured by the enrichment functions. They modeled confined plasticity around the crack tip in 2D. As a plastic description the HUTCHINSON-RICE-ROSENGREEN (85; 127) fields for power-law hardening material are used. The enrichment functions are resolved of a truncated expansion of the HUTCHINSON-RICE-ROSENGREEN fields on Fourier harmonics. As a result, six functions for 2D mixed mode fracture are applied to model the stress field at the crack tip (49). In the case of plastic material behavior it is also possible to use a modified version of the 'classical' front enrichment functions. Within the context of cohesive crack growth modified front enrichment functions are applied by MOËS AND BELYTSCHKO (109). If ideal plastic material behavior is applied no stress singularity occurs at the crack front, i.e. the front enrichment functions do not depend on $\sqrt{r}$ but on r^β with $\beta \geq 1$. The exponent β is changed in the context of a cohesive crack model in (109). MOËS AND BELYTSCHKO chose $\beta = 1$, $\beta = 1.5$ and $\beta = 2$. As a result nearly no difference in the solution fields were obtained. The new front enrichment functions read

$$\begin{aligned} \boldsymbol{f}_{pl}(\boldsymbol{x}) &= \boldsymbol{f}_{pl}(r,\varphi) \\ &= r^\beta \left\{ \sin\left(\frac{\varphi}{2}\right), \cos\left(\frac{\varphi}{2}\right), \sin\left(\frac{\varphi}{2}\right)\sin(\varphi), \cos\left(\frac{\varphi}{2}\right)\sin(\varphi) \right\} \end{aligned} \tag{4.30}$$

where $\beta = 2$ is chosen for the ideal plastic case. As proposed by (109), this choice is reasonable as the influence of different values for β larger than one is not that significant.

4.3.3 XFEM and Hanging Nodes

Even when using the XFEM, the simulation results are more precise the finer the mesh, especially in regions with high stress gradients. Thus, an adaptive refined mesh within domains of interest should be used. An application of mesh refinement just by subdividing elements leads to incompatible *hanging* nodes, see figure 4.9. First studies for hanging nodes with

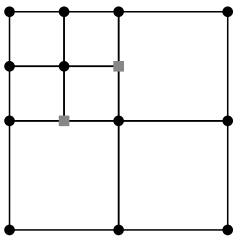

Figure 4.9: Mesh with incompatible *'hanging'* nodes, marked in gray.

additional degrees of freedom were accomplished by GUPTA in 1978 (75). In this 2D approach the hanging nodes lie at the middle of an element edge. Special ansatz functions for the hanging nodes are developed. For modifications of the positions or for more than

one hanging node per element edge these ansatz functions have to be modified. Additionally, special quadrature schemes have to be applied within elements with hanging nodes. An extension of this theory to the XFEM was proposed by FRIES *et al.* in 2011 (60). Thus, special ansatz functions have been developed to ensure the partition of unity for elements with enriched hanging nodes. Allready without the XFEM, the quadrature scheme in elements with hanging nodes has to be modified (75) because some of the spezial ansatz functions have a kink on axis in the reference element. Thus, the element with hanging nodes has to be devided into subcells for quadrature purposes. For hanging node elements which are cut by a crack further subcells are requirded as already subcells are necessary for cut XFEM elements (60). FRIES *et al.* investigated other approaches using constraints for the hanging nodes instead of additional degrees of freedom. These are constraint conditions which are realized using a projection matrix or enforcing the constraints with LAGRANGE multipliers. In both cases, special care has to be taken for enriched hanging nodes as the hanging nodes have constraints for the degrees of freedom which are evaluated with the degrees of freedom of the surrounding nodes.
Within this work, a different approach is applied to avoid the special treatment of enriched hanging nodes. Therefore, hanging nodes are not allowed to be enriched or to depend on enriched nodes. Thus, in every refinement step all elements cut by a crack or including the crack front have to be refined. Thereafter, additional refinements may be necessary in the case of enriched hanging nodes or an enrichment of the nodes the hanging node depends on, as depicted in figure 4.10. Nevertheless, hanging nodes have to be enforced to remain on the

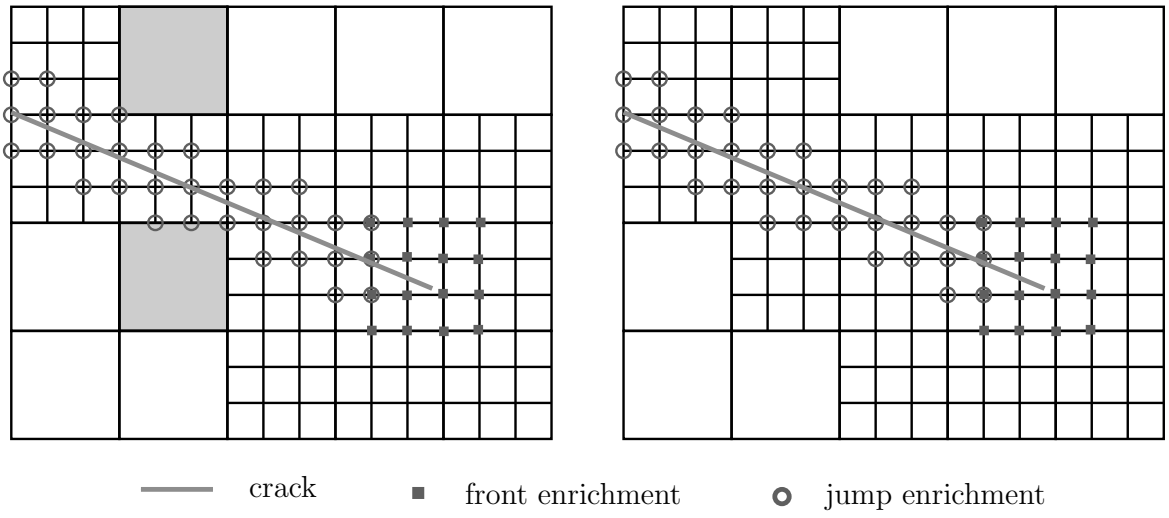

Figure 4.10: Resulting enrichments after mesh refinement. *left*: first resulting mesh with already all XFEM elements refined. Hanging nodes adjacent to the gray-shaded elements are enriched (lower element) or depend on enriched nodes (upper and lower element). *right*: final resulting mesh. Hanging nodes are not enriched and do not depend on enriched nodes.

element edge of the connected element, i.e. the implicit vector function

$$\boldsymbol{h}(\boldsymbol{u}) = \boldsymbol{u}_{hn} - \sum_{I=1}^{n_S} N_I(\boldsymbol{\xi}_{hn})\boldsymbol{u}_I = \boldsymbol{u}_{hn} - \sum_{I=1}^{n_S} \alpha_I \boldsymbol{u}_I = \boldsymbol{0} \tag{4.31}$$

has to be fulfilled. Here, n_S is the number of surface nodes, the hanging node depends on. As the function is implicit and in general non-linear, it cannot be solved directly. One possibility is the application of a projection matrix which reduces the system of equations with a coupling of degrees of freedom. This option leads to a huge projection matrix which has to be storred additionally. Another option is the application of penalty parameters, which work as springs between each hanging node and the surface the hanging node lies on. For penalty parameters the system has to be modified only slightly but the solution depends on a proper choice of the penalty parameter, i.e. the constraints are not fulfilled exactly. A third possibility to ensure the fulfillment of (4.31) is the use of LAGRANGE multipliers. LAGRANGE multipliers lead to zero entries on the main diagonal of the system of equations. Thus, a special solver which can handle these zero entries has to be used.
Here, LAGRANGE multipliers are chosen to enforce the constraint equations as they lead to the exact solution. The LAGRANGE multipliers are introduced using a mixed formulation to obtain the weak form of equilibrium. Hence, the weak form of equilibrium (4.5) and the variation of the constraint equation (4.31) have to be fulfilled. The constrained equation using LAGRANGE multipliers $\boldsymbol{\lambda}$ can be formulated as a potential

$$\Pi_\lambda = \boldsymbol{\lambda}\boldsymbol{h}(\boldsymbol{u}) \equiv 0 \tag{4.32}$$

which leads to a variational formulation written as

$$\delta\Pi_\lambda = \delta\boldsymbol{\lambda}\boldsymbol{h}(\boldsymbol{u}) + \boldsymbol{\lambda}\frac{\partial \boldsymbol{h}(\boldsymbol{u})}{\partial \boldsymbol{u}}\delta\boldsymbol{u} = 0. \tag{4.33}$$

Thus, the LAGRANGE multipliers as additional unknowns enlarge the system of equations. The mixed formulation of the weak form of equilibrium (cf. equation (4.5)) using LAGRANGE multipliers to enforce the hanging node constraints reads

$$\int_{\mathcal{B}} \boldsymbol{\sigma} : \operatorname{grad}\delta\boldsymbol{u}\,\mathrm{d}\mathcal{B} - \int_{\mathcal{B}} \boldsymbol{b}\cdot\delta\boldsymbol{u}\,\mathrm{d}\mathcal{B} - \int_{\partial\mathcal{B}_t} \bar{\boldsymbol{t}}\cdot\delta\boldsymbol{u}\,\mathrm{d}\partial\mathcal{B}_t + \delta\boldsymbol{\lambda}\cdot\boldsymbol{h}(\boldsymbol{u}) + \boldsymbol{\lambda}\cdot\frac{\partial \boldsymbol{h}(\boldsymbol{u})}{\partial \boldsymbol{u}}\cdot\delta\boldsymbol{u} = 0. \tag{4.34}$$

The needed differentiations of $\boldsymbol{h}(\boldsymbol{u})$ are

$$\frac{\partial \boldsymbol{h}(\boldsymbol{u})}{\partial \boldsymbol{u}_I} = \mathbf{1} \tag{4.35}$$

if I is the index of a hanging node and

$$\frac{\partial \boldsymbol{h}(\boldsymbol{u})}{\partial \boldsymbol{u}_I} = -\alpha_I\mathbf{1} \tag{4.36}$$

if I is the index of a regular node the hanging node depends on.
To summarize, a lot of aspects regarding the XFEM have been presented. The XFEM combined with a stabilization for barely cut elements and with the introduction of special quadrature schemes, is a useful method for fracture analysis. However, special care has to be taken for blending elements as the partition of unity has to be fulfilled in the overall domain. To improve the solution especially in areas with high stress gradients as they are expected around

crack fronts, mesh refinement is reasonable. Therefore, hanging nodes in the context of XFEM are introduced. The constraint equations are enforced with LAGRANGE multipliers. Additionally, regarding material behavior, an extention to elastoplasticity is presented. However, as the XFEM is a common method for different applications a number of modifications and extensions exist, which are not discussed here. Special treatments for branched and intersecting cracks can be found e.g. in (38; 80). An extension to special crack tip functions for cohesive cracks is given in (109), among others. The treatment of quadratic elements within the XFEM can be found in (137). These are only some extensions without any demand on completeness.

Chapter 5

Multiscale Simulation

As already shown in section 3.2, small cracks in the vicinity of a main crack front should be considered. The presented XFEM enrichment scheme requires non-enriched nodes between crack fronts but does not offer the possibility of a single crack beginning and ending in the same element. Thus, the mesh size must be adapted to the size of the cracks. As small cracks are orders of magnitude smaller than the main crack, the mesh size has to be reduced drastically in the vicinity of a crack front. Within a single scale simulation, extremely local adaptive mesh refinements would be necessary. The high ratios between the element sizes result in a poorly conditioned system of equations, which leads to high computational costs. Thus, a decomposition of the mesh for the main crack representation and for the representation of the small cracks is reasonable regarding efficiency. Different methods exist to perform this decomposition. A few of them will be mentioned in section 5.1. Thereafter, a closer look at a multiscale technique designed for XFEM fracture applications, namely the multiscale projection method of LOEHNERT AND BELYTSCHKO (98), is taken in section 5.2. The transition of the field variables between the scales, the necessity for the stabilization technique of section 4.3.1 and the quantities of influence on the method are given in detail.

5.1 Overview about Multiscale Approaches

Single scale solutions which include the effects of the micro structure often lead to large computational costs. Usually, the solution has to be found in a defined time and on standard computers. Thus, multiscale techniques which enable the consideration of the given micro structure while keeping low computational costs are developed. Different techniques such as multiscale simulations based on homogenization methods or the use of overlapping structures exist. Other possibilities are domain decomposition techniques or the application of locality assumptions on the fine scale. Multiscale methods within the XFEM/GFEM exist.These are based on multigrid technique, a global-local approach or the multiscale projection method, respectively. Different aspects of these methods are discussed in the next paragraphs.
Within homogenization based FE^2 methods, a fine scale model is solved at every coarse scale integration point. Both the coarse scale model and the fine scale model are defined to be separate boundary value problems. The type of continuum equations applied on the coarse

scale defines the order of homogenization which is necessary on the fine sclae. Nevertheless, all homogenization methods make use of averaging theorems, i.e. averaged quantities are projected from the fine scale onto the coarse scale. The fine scale boundary value problem is usually a representative volume element (RVE) under certain boundary conditions. The RVE represents the fine scale structure of the underlying material within FE^2 methods, cf. (52). The fine scale boundary value problem is solved at every integration point of the coarse scale domain. The coarse scale deformations enter the fine scale boundary value problem by means of boundary conditions for the representative volume element. Stress responses as well as tangential stiffness matrices are averaged on the fine scale and given back to the coarse scale continuum mechanical model. Within this type of homogenization the coarse scale and the fine scale are solved with finite elements. An extension to this method, which allows for a different behavior of the RVE, is e.g. given in (91) and is subordinated to higher order homogenization methods. Furthermore, homogenization methods which lead to effective material parameters on the coarse scale exist, cf. e.g. (106). An overview of computational homogenization methods is given in (63). Computational homogenization methods which make use of averaging on the fine scale RVEs, are not suitable for fracture mechanics because they usually cannot upscale localization phenomena onto the coarse scale. Nevertheless, extensions which are able to take fracture processes into account are developed. One of these possibilities is the technique of multiscale aggregating discontinuities (21), which aggregates discontinuities of the RVE. The discontinuity direction as well as the magnitude of the displacement of the discontinuity are upscaled. However, the interaction of fine scale cracks cannot be represented, as a detailed analysis of the fine scale structure, which is reflected in the coarse scale solution, is not possible. As pointed out in (63) as well, if localization effects have to be included in the simulation, usually other types of multiscale approaches are applied.

A multiscale method which uses the Arlequin method for overlapping substructures is presented by BEN DHIA AND RATEAU (24). The method is based on the superposition of mechanical states with an energy averaging. The averaging parameter is problem dependent but the method can also be used for fracture analysis. The mesh superposition method (s-version) of FISH (54) enables the representation of cracks without the XFEM. He uses overlapping FE meshes with a patch of higher-order hierarchical elements in the regions where high gradients indicated by the solution exist.

A domain decomposition method with local enrichments has been developed by GUIDAULT *et al.* (74) without the consideration of smaller cracks but with an efficient treatment of local and global effects. Another domain decomposition method was developed by KRAUSE AND RANK (92) in 2003. They include a priori known information and enable a combination of *h*- and *p*-FEM within a hierarchical formulation.

A multiscale method including a coupling of the scales with LAGRANGE multipliers is devised by MERGHEIM (105). Within this method the discontinuities are only present on the fine scale. Thus, considering fracture, the whole crack path has to be included in the fine scale domain, which can enlarge the fine scale drastically for 3D simulations.

The multigrid method combined with the XFEM as presented by RANNOU *et al.* (124) contains prolongation vectors for the degrees of freedom for the transfer between the different scales. KIM *et al.* (90) proposed a twoscale technique for GFEM with a global-local

approach to introduce partition of unity enrichments on the coarse scale, which are based on the fine scale solution. LOEHNERT AND BELYTSCHKO (98) proposed a multiscale projection method in an XFEM context with a weak coupling between the coarse and the fine scale.
Accurate and efficient simulations especially for 3D simulations are in the focus of this work. Therefore, a multiscale technique which enables accurate solution with low computational effort is desired. The multiscale projection method (98) has no need of problem dependent variables as e.g. in (24) and is able to capture influences of cracks on each other in an efficient way. In contrast to (105) only the domain around the main crack front can be included in the fine scale domain. The effects of the fine scale structure influence the coarse scale, as stresses are projected from the fine scale solution onto the coarse scale domain. Further fine scale effects are not taken into account in the presented application of the multiscale projection method. A possibility to include microstructural effects is presented by AHMAD AKBARI *et al.* (2). They implemented an FE^2 approach in the region without localization phenomena. If localization appears a domain decomposition scheme is applied.
In this thesis, the fine scale cracks are assumed to be orders of magnitude smaller than the coarse scale cracks. This separation of scales enables efficient simulations which can be done in parallel for multiple fine scale domains. As the combination with the XFEM enables crack propagation without remeshing and (nearly) arbitrary crack paths, the multiscale projection method (98) is applied to accurately include the effects of the micro structure.

5.2 Multiscale Projection Method

The applied multiscale projection technique was developed by LOEHNERT AND BELYTSCHKO in 2007 (98). The method was extended to 3D in 2008 (99). A short overview of the method is given in the next paragraphs. For clarity all figures are sketched in 2D even if the equations are given for 3D applications.
Let Ω^0 be the discretized body for a multiscale analysis. Cracks or geometrical features leading to stress singularities are included in Ω^0. Thus, regions with high strain/stress gradients exist. Within these regions the possibility for crack propagation or crack initiation is increased. Therefore, the underlying structure concerning fine scale cracks may significantly influence the crack propagation behavior and has to be considered. As the fine scale cracks are a few orders of magnitude smaller than the cracks considered on the coarse scale, the necessary discretization to represent the fine scale cracks cannot be included in a single scale simulation. An adaptive refined mesh in a single scale simulation would reach a large ratio between the coarsest and the finest elements, which results in an ill-conditioned system of equations and high computational costs. Therefore, the proposed multiscale projection technique is applied. Thus, $\Omega^1 \subset \Omega^0$ is defined to be the necessary part for a fine scale analysis, see figure 5.1. Within the fine scale domain the mesh resolution is significantly increased to represent fine scale cracks whereas the coarse scale cracks remain unchanged. For the projection method it is important that the coarse scale crack has the same geometry in both the coarse and the fine scale domain. The same crack geometry is ensured by applying an interpolation of the level set functions of a coarse scale element to the enriched nodes of the fine scale domain. The trilinear interpolation within the fine scale elements leads to the

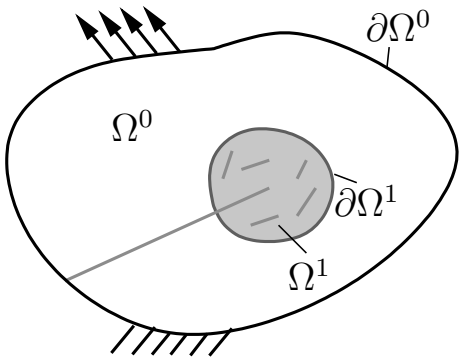

Figure 5.1: Definition of the domain $\Omega^1 \subset \Omega^0$ for the fine scale analysis.

same crack geometry as on the coarse scale domain. As the crack geometries have to be the same barely cut elements need to retain their shape as well as the geometry of the crack path. Hence, to avoid ill-conditioned global stiffness matrices none of the stabilization techniques of the crack geometry can be used. But instead a special preconditioner or the proposed stabilization technique for the XFEM (section 4.3.1) should be applied in the context of the multiscale projection method (section 5.2.2).

5.2.1 Scale Coupling

Different methods exist to couple the scales within multiscale simulations. A coupling procedure with LAGRANGE multipliers as studied by MERGHEIM (105) enlarges the system of equations. The constraint equations have to be included in the stiffness matrices to enforce the scale coupling. A different method which couples the scales in a weaker sense is the separation of the fine scale simulation from the coarse scale (98). After the application of DIRICHLET boundary conditions from the coarse scale to the fine scale domain boundary, the fine scale can be solved independently. Thus the simulations of multiple fine scale domains can be done in parallel. The results are projected back from the fine scale domain to the coarse scale in terms of stresses. The coarse scale can thereafter be solved again. Thus, an iterative process has to be performed until equilibrium on both scales is achieved. This type of scale coupling enables an efficient simulation. The scale coupling process is described in more detail in the following.
The multiscale projection method (98), (99) allows for NEUMANN and DIRICHLET boundary conditions on Ω^0. The XFEM displacement field is assumed to be

$$\boldsymbol{u}^h = \boldsymbol{u}^{0h} + \bar{\boldsymbol{u}}^{1h} \tag{5.1}$$

with the approximated coarse scale displacement field $\boldsymbol{u}^{0h}$ and the approximated fine scale fluctuation field $\bar{\boldsymbol{u}}^{1h}$ resulting from the features only included in the fine scale. The weak form of equilibrium for the coarse scale then reads

$$\int_{\Omega^0} \boldsymbol{\sigma}(\boldsymbol{u}^{0h} + \bar{\boldsymbol{u}}^{1h}) \colon \operatorname{grad} \delta\boldsymbol{u}^{0h} \,\mathrm{d}\Omega^0 - \int_{\Omega^0} \boldsymbol{b}^h \cdot \delta\boldsymbol{u}^{0h} \,\mathrm{d}\Omega^0 - \int_{\partial\Omega_t^0} \bar{\boldsymbol{t}}^h \cdot \delta\boldsymbol{u}^{0h} \,\mathrm{d}\partial\Omega_t^0 = 0 \tag{5.2}$$

containing the coarse scale test function $\delta\boldsymbol{u}^0$. The fine scale fluctuations are assumed to vanish at the fine scale boundary and to be negligible in the rest of the coarse scale domain,

i.e. in $\Omega^0 \setminus \Omega^1$ (98; 99). Thus, the boundary conditions for the fine scale can be given as pure DIRICHLET boundary conditions

$$\boldsymbol{u}^{1h} = \boldsymbol{u}^{0h} \quad \text{on} \quad \partial\Omega^1. \tag{5.3}$$

The fine scale displacement field in the rest of the fine scale domain is defined to be a summation of the coarse scale displacement field and the fine scale fluctuation field

$$\boldsymbol{u}^{1h} = \boldsymbol{u}^{0h} + \bar{\boldsymbol{u}}^{1h}. \tag{5.4}$$

The weak form of equilibrium for the fine scale is therefore written as

$$\int_{\Omega^1} \boldsymbol{\sigma}(\boldsymbol{u}^{1h}) : \operatorname{grad}_{sym} \delta\boldsymbol{u}^{1h} \, \mathrm{d}\Omega^1 - \int_{\Omega^1} \boldsymbol{b}^h \cdot \delta\boldsymbol{u}^{1h} \, \mathrm{d}\Omega_1 = 0 \tag{5.5}$$

with the fine scale test function $\delta\boldsymbol{u}^1 \in \mathrm{H}^1$ on Ω^1.
In a first step, the overall coarse scale is solved without consideration of the fine scale. After the definition of the fine scale domain, the fine scale elements are constructed. Every coarse scale element is divided into fine scale elements, with the result that the fine scale mesh represents a conforming discretization of the coarse scale elements, cf. figure 5.2. The conforming mesh is needed within the presented multiscale projection method to enable the integration of the fine scale domain on the coarse scale. The second step is the calculation

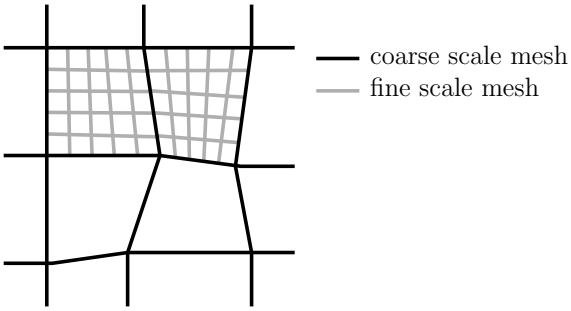

Figure 5.2: The fine scale mesh represents a conforming discretization of the coarse scale elements.

of the fine scale boundary conditions provided by the coarse scale displacement field. The application of DIRICHLET boundary conditions is only possible for traction free crack surfaces, i.e. no cohesive forces and no crack closure on the coarse scale crack. If a coarse scale crack cuts the boundary of the fine scale, nodes on the coarse as well as on the fine scale have to be enriched. For enriched nodes the displacement field is no longer represented only by the standard degrees of freedom for the presented type of XFEM. To make sure that all the degrees of freedom of all fine scale nodes on the fine scale boundary can be determined correctly, a projection of the coarse scale displacement field onto the fine scale mesh is required. This projection can be achieved with e.g. the BUBNOV-GALERKIN method, the least squares method or the collocation method. For the XFEM the extended discretized displacement fields $\hat{\boldsymbol{u}}_I^1$ of the fine scale domain and $\hat{\boldsymbol{u}}_I^0$ of the coarse scale domain are used. The collocation method is a method which introduces weighted residuals. The DIRAC function as weighting function enforces the fine scale displacement to be exactly the same as

the coarse scale displacements at the so-called collocation points. As a drawback it should be mentioned that the error cannot be controlled at further points. In the present work, a least squares projection is used, which leads to the same result as the BUBNOV-GALERKIN approach. These methods lead to fine scale displacements which fulfill the displacement projection in a weak sense. A multiplication with the fine scale test function and an integration over the fine scale domain leads to an averaged equilibrium

$$\int_{\Omega^1} \left(\sum_{I=1}^{n^1} \hat{N}_I^1 \hat{\boldsymbol{u}}_I^1 - \sum_{J=1}^{n^0} \hat{N}_J^0 \hat{\boldsymbol{u}}_J^0 \right) \cdot \left(\sum_{K=1}^{n^1} \hat{N}_K^1 \hat{\boldsymbol{\eta}}_K^1 \right) \mathrm{d}v = 0 \tag{5.6}$$

with n^1 as the total number of fine scale nodes and n^0 as the number of coarse scale nodes located in the fine scale domain. Solving this equation for $\hat{\boldsymbol{u}}_I^1$ leads to the required DIRICHLET boundary conditions for the boundary nodes of the fine scale domain. Equation (5.6) has to be solved as an integral on the overall fine scale even if only the nodes at the surface of Ω^1 need a prescribed boundary condition. As sketched in figure 5.3 the fine scale boundary between nodes (1) and (2) is not cut by the coarse scale crack but both nodes have to be enriched. The additional degrees of freedom of the jump enrichments and the standard degrees of freedom are linear dependent in the considered case if the integral is evaluated solely on the boundary $\partial\Omega^1$. If the integral is chosen on the first row of elements along the boundary, the problem is transferred to other nodes, e.g. nodes (3) and (4). Thus, the integral is evaluated in the entire domain Ω^1. As non-enriched nodes need only the boundary conditions

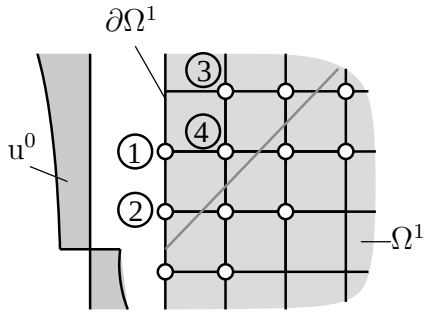

Figure 5.3: Enrichments at the fine scale boundary resulting from a coarse scale crack (98).

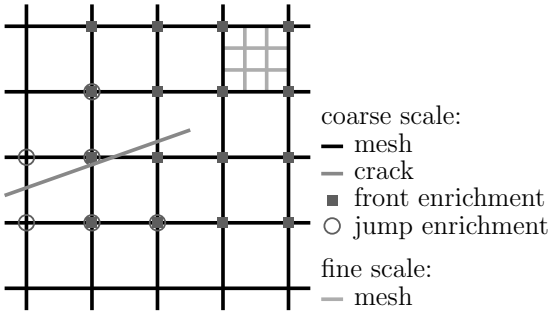

Figure 5.4: Provided displacements of the coarse scale domain for the fine scale domain are influenced by the ramp function.

for the standard degrees of freedom, it is sufficient to directly evaluate the displacements at these positions and thus significantly reduce the computational effort. Hence, the projection is only applied for the enriched nodes.

A coarse scale crack front cutting the fine scale boundary leads to small errors for the projected boundary conditions. In this case, the displacement field on the coarse scale is evaluated with front enrichments including the ramp function. Thus, the displacement field on the coarse scale is influenced by the ramp function. These errors are applied to the fine scale boundary with the projection method. A coarse scale element, including the described effect for the fine scale elements, is sketched in figure 5.4.

With the DIRICHLET boundary conditions provided by the coarse scale, the fine scale problem can be solved. Within the fine scale domain the coarse scale cracks and also smaller cracks are modeled explicitly using the XFEM. The next step is the projection of the fine scale results onto the coarse scale. Therefore, the fine scale stresses at the fine scale integration points are projected onto the coarse scale. Thus, the fine scale features are considered only implicitly at the coarse scale. After some iterations, equilibrium on both scales is reached (98; 99).
Of course, more than one coarse scale crack can be included in the coarse scale simulation. Multiple fine scale domains may be considered, as well. In such cases the fine scale boundary value problems can be solved in parallel. Thus, an efficient simulation regarding the computational time can be realized.

5.2.2 Necessity of Stabilization

As mentioned above, special care has to be taken if the ratio of the volume of the smaller part of the intersected element to the overall element volume is very small. Especially within the multiscale projection method it is very important that the crack path of the coarse scale crack is the same on both scales especially in terms of error estimation. Since all possibilities presented in figure 4.8 to avoid ill-conditioning lead to a modification of the crack path, here only the possibility of node movement away from the crack (subfigure 4.8d)) is chosen for the ilustration of the problem. The results at the integration points of the fine scale are projected from the fine scale onto the coarse scale. Thus, it is important, that the considered point lies in the same coarse scale element before and after the movement of the node. Unfortunately, a problem can arise if the main crack cuts only a small edge of a fine scale element at a coarse scale element boundary. The node of that fine scale element will be moved and the integration point does not lie in the same coarse scale element as before. The same problem arises if the node movement is caused by a fine scale crack. Both cases are shown in figure 5.5 for points located in the gray areas. These cases can only be avoided for straight crack geometries

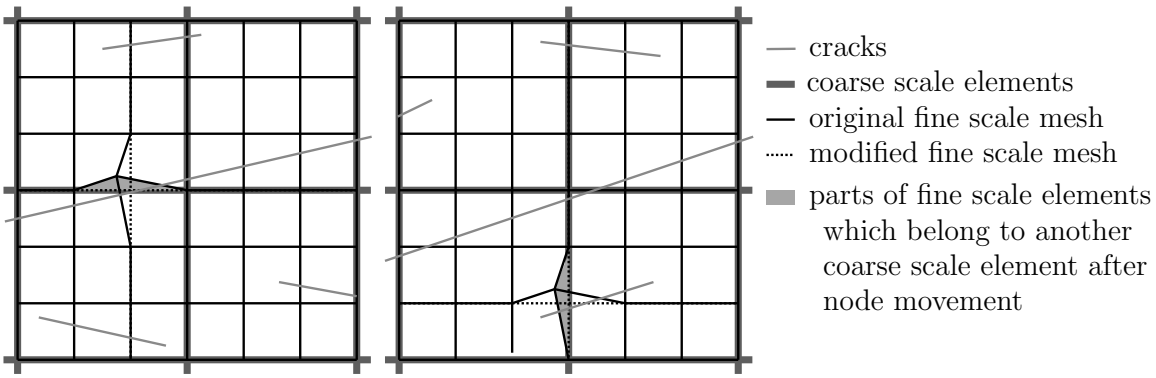

Figure 5.5: Node movements within a multiscale simulation, which lead to difficulties during the simulation. A fine scale node which lies on the boundary of a coarse scale element is moved into another fine scale element due to the main crack (left) or a fine scale crack (right).

and well structured meshes. Thus, if the multiscale projection method (98) is applied, the

implementation of the stabilization technique of LOEHNERT (97) enables robust multiscale simulations with arbitrary crack and mesh geometries.

5.2.3 Numerical Example Referring to Efficiency

The main benefit of applying the multiscale projection method is the highly accurate simulation with drastically reduced computational costs. In the following example a single scale simulation including a small crack and a larger crack is compared to a multiscale simulation and a coarse scale simulation without the small crack. The small and the larger crack will be defined as a fine scale crack and a coarse scale crack respectively.
A linear elastic material with a YOUNG's modulus of $E = 210\,\mathrm{GPa}$ and a POISSON ratio of $\nu = 0.3$ is chosen. The setup is displayed in figure 5.6 with the coordinate system placed in the center of the block. The block is fixed at the bottom and deformed with a prescribed

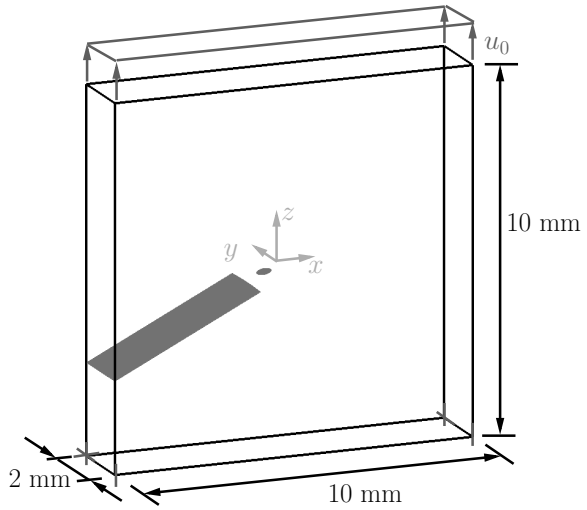

Figure 5.6: Setup to analyze the convergence of the multiscale method compared to the single scale solution.

displacement of $u_0 = 1\,\mathrm{mm}$ at the top. Both cracks can be described with planar ellipses with a center point $\boldsymbol{c}^j$ and two perpendicular basis vectors $\boldsymbol{b}_i^j$ where $j = 0, 1$ refers the scale and $i = 1, 2$ the basis, respectively:

$$\boldsymbol{c}^0 = \begin{pmatrix} -5.0 \\ 0.0 \\ -2.48887321 \end{pmatrix} \boldsymbol{b}_1^0 = \begin{pmatrix} 4.1002418 \\ 0.0 \\ 2.00073 \end{pmatrix} \boldsymbol{b}_2^0 = \begin{pmatrix} 0.0 \\ 10.0 \\ 0.0 \end{pmatrix} \tag{5.7}$$
$$\boldsymbol{c}^1 = \begin{pmatrix} -0.436072 \\ 0.0 \\ -0.25137 \end{pmatrix} \boldsymbol{b}_1^1 = \begin{pmatrix} 0.193185 \\ 0.0 \\ 0.051764 \end{pmatrix} \boldsymbol{b}_2^1 = \begin{pmatrix} 0.0 \\ 0.2499998 \\ 0.0 \end{pmatrix}.$$

For the single scale simulation the discretization is $225 \times 45 \times 225$ elements. As a result, the total reaction force at the top of the block is evaluated. Within the multiscale approach, different coarse scale discretizations are chosen, but the fine scale mesh resolution is kept constant with the same resolution as in the single scale simulation. For comparison, the coarse scale is simulated without any fine scale consideration. The fine scale is chosen to be a tubular domain with a radius of $1.7\mathrm{mm}$ around the coarse scale crack front. The

discretization of the coarse and fine scales are summarized in table 5.1. Additionally, the resulting number of degrees of freedom of the respective fine scale simulation is given. As a result it can be seen that the fine scales of all multiscale simulations have nearly the same number of degrees of freedom. Thus, the results are shown only depending on the coarse scale degrees of freedom.

coarse scale elements	number of coarse scale degrees of freedom	fine scale elements per coarse scale element	number of fine scale degrees of freedom
$15 \times 3 \times 15$	3,733	$15 \times 15 \times 15$	748,632
$25 \times 5 \times 25$	13,257	$9 \times 9 \times 9$	744,684
$45 \times 9 \times 45$	65,617	$5 \times 5 \times 5$	708,396
$75 \times 15 \times 75$	281,437	$3 \times 3 \times 3$	662,988

Table 5.1: Discretization and number of degrees of freedom for a twoscale efficiency study.

The results are presented in figure 5.7. The coarse scale simulations without a fine scale consideration converge to a different solution as the fine scale crack is not considered. Final convergence is not reached in this study but the trend to different solution to the simulation result with the modeled fine scale crack can be determined. However, for the twoscale simulation the single scale result can be reached closely with a coarse scale mesh of $25 \times 5 \times 25$ or more elements while the computational costs are reduced drastically accoriding to the number of degrees of freedom. Each twoscale simulation needs an iteration between the coarse and the fine scale, but with four iteration steps the computational time is still less than for the single scale simulation. Additionally, as the number of degrees of freedom is reduced, the simulation needs less memory space. The single scale simulation with $225 \times 45 \times 225$ elements leads to 7,079,329 degrees of freedom and a reaction force of 269.12 N. The twoscale simulation with a coarse scale mesh of $45 \times 9 \times 45$ leads to $65,617 + 708,396 = 774,013$ degrees of freedom and a reaction force of 269.10 N. The curves of the coarse scale and the multiscale simulation in figure 5.7 are not totally converged with an increasing number of degrees of freedom. However, a further refinement of the coarse scale is not taken into account, as the number of degrees of freedom is reduced by factor 9 and the reaction force approximates the single scale solution with 99.99 %.

5.2.4 Size Effects within the Multiscale Projection Method

The accuracy of the multiscale projection method is influenced by three parameters: the coarse scale mesh resolution, the fine scale mesh resolution and the size and shape of the fine scale domain.

The coarse scale discretization influences the stiffness of the coarse scale solution as well as the stiffness of the fine scale boundary conditions due to the displacement projection. The discretization of the coarse scale leads at the fine scale boundary to displacements matching the coarse scale solution field. The fine scale elements in the interior of the domain would be

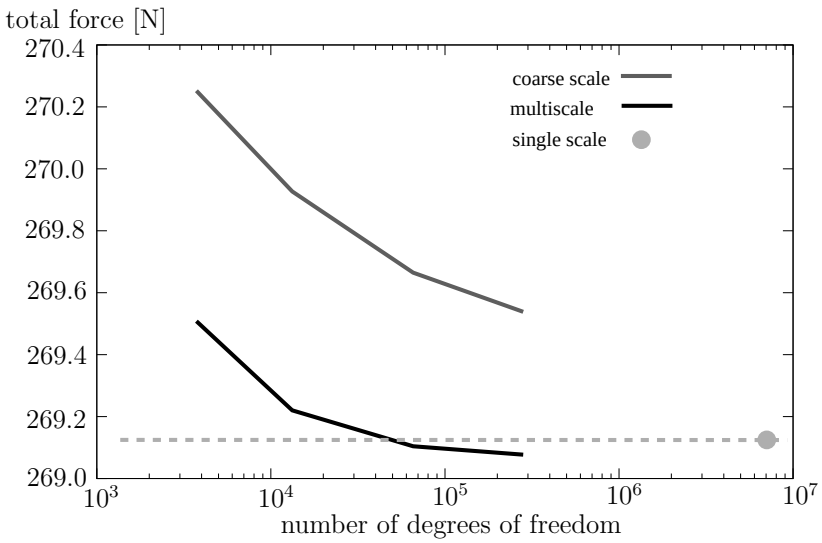

Figure 5.7: Reaction force at the top of the coarse scale domain. For the coarse scale simulation and the multiscale simulation the reaction force is related to the degrees of freedom of the coarse scale. The additional number of degrees of freedom for the fine scale simulation is $\approx 700,000$.

able to represent a softer solution, but they are restricted at the fine scale domain boundary. Therefore, large coarse scale element sizes in the domain for fine scale simulations should be avoided (98). Thus, a discretization error indicator should lead to adaptive mesh refinement strategies to improve the accuracy of the results and to enable the use of a refined coarse scale in the domain where a fine scale simulation is reasonable.

In the original publication on the multiscale projection method, the fine scale domain is chosen to be a circle with the center point at the coarse scale crack tip respectively a circular tube around the crack front (98; 99). The influence of varying radii was studied in (98). The fluctuation $\bar{\boldsymbol{u}}^{1h}$ on the fine scale decreases rapidly with the distance of the main crack front to the fine scale cracks. It has been shown that even a fine scale of only twice the size of a typical fine scale crack leads to acceptable results. Within this assumption, the fine scale domains are solely localized around coarse scale crack fronts. In (98) the shape of the fine scale domain is not varied. To optimize the fine scale domain with respect to computational effort while keeping the influence of the fine scale domain, a method to define the shape of the fine scale domain around each main crack front has to be applied. A model indicator gives the possibility to define the reasonable elements of the coarse scale domain, which should be included in the fine scale domain. Hence, a possible model indicator is applied to the multiscale projection method in section 6.4. Furthermore, additional criteria for taking fine scale cracks into account may be reasonable if e.g. crack initiation is expected. Thus, again a model indicator to detect reasonable fine scale domains for each multiscale simulation is advisable.

Just like the coarse scale discretization, the fine scale discretization has an influence on the accuracy of the solution (98). A discretization error controlled simulation of the fine scale enables the possibility for accurate stress representations especially around the crack fronts. Especially for 3D simulations, the computational time can be drastically reduced

using adaptive mesh refinements (see section 7.2). This motivates once more the need of adaptive mesh refinement based on error estimation techniques.

Chapter 6

Error Estimation

From a physical system to a numerical solution a lot of error sources exist. To mention only a few, errors can already be made by the choice of the mathematical model to represent the physical system. Other error sources are the limited precision of computers or the numerical approximation, e.g. integration errors. These and further types can e.g. be found in (132). The different error sources have different amounts of influence on the numerical results. If for instance the assumption of small deformations within the mathematical model is invalid for the physical system this error may not be detected during the simulation. Regarding the simulation results the legitimacy of the assumptions has to be examined.
Within this work the focus is put on two error sources, namely the discretization error and the model error. The discretization error is influenced by the chosen type of finite elements and the element sizes. Thus, a discretization error estimation technique leads to an adaption of the mesh size (*h*-refinement) or an adaption of the polynomial order of the finite elements (*p*-refinement) or a combination of both (*h*-*p*-refinement). An error estimation technique for *h*-refinement within XFEM simulations is presented in section 6.3. A model error indicates regions in which a more detailed analysis of the problem is reasonable, e.g. the use of a 3D model instead of a 2D approximation. With the application of a model indicator it is also possible to detect the fine scale domain for the multiscale projection method of chapter 5. A reasonable model indicator is presented in section 6.4 and a numerical validation for the model indication technique is given.

6.1 General Error Estimation Techniques

Error estimation techniques are subdivided into *a priori* and *a posteriori* error estimators. *A priori* error estimators are based on a behavior within the model, which is known in advance, e.g. close to re-entrant corners the strain gradients are rather high, such that a finer mesh in that domain should be applied. DUARTE *et al.* (43) used a priori knowledge for mesh refinement at the crack fronts. Additionally *a priori* error estimates were applied to estimate the exact solution for the strain energy. Further *a priori* error estimates can be found in e.g. (3; 146).
The *a posteriori* error estimation is based on the current approximated solution of the problem. First applications of *a posteriori* error estimation are presented by BABUŠKA AND

RHEINBOLDT in 1978 (10; 11). They provided an adaptive optimization of the finite element mesh. The different types of *a posteriori* error estimators are residual based, recovery based, interpolation type or goal oriented error estimators.
Residual based error estimators can be explicit or implicit. They make use of some norm of the residual of the governing equations associated with the boundary conditions (10). Two residuals are considered within this error estimation type, the interior residual and the boundary residual. Residual-type error estimators are e.g. used by STEIN AND RÜTER (139) based on the solutions of Neumann problems on the element level which are subjected to equilibrated residuals. Explicit residual error estimators lead to local error estimation but include an unknown constant. If the worst possible scenario is chosen to guess the constant, the error estimator leads to pessimistic results. An implicit residual based error estimator on element level gets rid of the unknown constant (3).
Recovery based error estimators are based on a higher-order post-processed solution. The solution may be recovered using nodal averaging, a global projection (79) or by using superconvergent points for the stress solutions (14). Knowing this higher-order post-processed solution, local and global error indicators can be computed (162). This error estimation technique is the basis for the applied discretization error indicator described in section 6.3 and was presented first by ZIENKIEWICZ AND ZHU in 1987 (162).
Interpolation type error estimators depend on the local displacements and the interpolation properties of the current finite element mesh (39). An important issue is the necessity of the second derivatives of the solution field to determine the element wise interpolation error.
Goal oriented error estimators focus on quantities of interest, e.g. stress intensity factors in case of fracture mechanics (65; 118). They are based on a dual solution of the problem and were first presented in 1984 (8). For the dual solution the problem is solved in terms of an influence function. This influence function measures the influence of external loads to the local quantity of interest. The error estimator can then be applied to improve the solution regarding the desired quantities.
This list is not intended to be complete, but already shows the diversity of *a posteriori* error estimators. Overviews of these estimators and further *a posteriori* error estimation techniques are given in (3; 71; 103).

6.2 Error Estimation for Fracture Mechanics

Regarding fracture mechanics problems *a posteriori* error estimation techniques for solutions without the XFEM were presented by JAYASWALL AND GROSSE in 1993 (87). Their 2D approach is based on the ZIENKIEWICZ AND ZHU error estimator (162). The FEM solution is derived with quarter point elements around the crack tip. To recover the enhanced stress field in elements around a crack tip, asymptotic analytical solutions are added. Another approach was developed by GINER *et al.* (66), who separated the discretization error appropriately to either mode I or mode II crack opening. Their proposed error estimation technique is related to the equivalent domain integral method to obtain the estimates for each mode.
Nowadays, the different error estimation techniques are also applied to FE simulations based on the PUM. In (9) the first considerations to *a posteriori* error estimates concerning the

PUM have been done. Within this first application an *a posterior* error estimator derived on element patches is presented. Following this approach an error estimation for the GFEM was presented by STROUBOULIS *et al.* in 2006 (143). They developed a two-sided estimate based on patch-wise residual indicators. A second residual type error estimation technique was proposed by PANNACHET *et al.* in 2009 (119). Within the PU-cohesive zone model the accuracy of the energy norm does not guarantee the accuracy of the local quantities of engineering significance. Thus, their error estimator is based on energy and goal oriented measures and used for *p*-refinement.
A very similar recovery based error estimation technique for the XFEM, as presented in section 6.3, was devised by DUFLOT AND BORDAS (47) in 2008 and is thus discussed in more detail in the referred section. Their recovering process is based on a strain smoothing technique. In addition BORDAS *et al.* devised an error estimator based on extended moving least squares (28; 29). The asymptotic solution field for the crack front is added to the moving least squares basis functions and an enhanced smoothed strain field is obtained. In 2008 RÓDENAS *et al.* investigated an error estimation technique based on a superconvergent patch recovery for the improved solution (129). A decomposition into a singular and a smooth part for the enhanced strain field is applied. The singular field is obtained by utilizing the analytical solution including the stress intensity factors. An extension of the method is published in (67). This method is compared to an equilibrated moving least squares recovery technique (called MLSCX) (128). The MLSCX needs no special treatment for hanging node elements and provides a continuous recovered stress field. BYFUT AND SCHRÖDER (31) presented a heuristic error estimator for *h*-*p*-refinement in 2012. To decide for *p*-refinement an error indicator based on the knowledge of *a priori* error estimation techniques is applied. Otherwise a reference solution with a fine mesh and a polynomial order of two is chosen for comparison, which induces large computational costs.
In 2009 PANETIER *et al.* (118) proposed constitutive relation error applied for goal oriented error estimation concerning the XFEM. They calculated strict bounds for the error estimation of stress intensity factors which are important for 2D crack propagation analysis using the XFEM. Another goal oriented error estimator developed as a residual type error estimation technique is proposed by GERASIMOV *et al.* (65). Different enrichment functions for the 2D near tip field to the original XFEM are chosen in (65). These new enrichment functions lead to a reduced error in the crack tip element as the divergence-free condition within the crack tip field is fulfilled a priori. However, further studies of these enrichment functions especially of their application to 3D simulations are missing. Nevertheless, within the presented 2D examples in (65) the new functions performed well.
In this thesis, an a posteriori recovery based error indicator is presented. As for XFEM simulations the proof of bounded error estimators is demanding, an error indicator will be studied and applied to XFEM simulations. A requirement for the error indicator is the application to general problems as e.g the application to different types of material behavior.

6.3 Mesh Adaptivity

Adaptive meshes based on *a posteriori* discretization error estimation within a FE mesh lead to higher accuracy of the simulation results while keeping low computational costs. The

discretization error can be expressed for displacements $\boldsymbol{e} = \boldsymbol{u}^h - \boldsymbol{u}$ or in terms of strains $\boldsymbol{e}_\varepsilon = \boldsymbol{\varepsilon}^h - \boldsymbol{\varepsilon}$ or stresses $\boldsymbol{e}_\sigma = \boldsymbol{\sigma}^h - \boldsymbol{\sigma}$. As for general setups the analytical solutions $\boldsymbol{u}$, $\boldsymbol{\varepsilon}$, $\boldsymbol{\sigma}$ are unknown, an estimation of the discretization error is required. Thus, an enhanced field for the considered variable is used to obtain an approximation of the analytical solution that usually is better than the numerical result. Using the enhanced solutions the approximated errors can be expressed as

$$\boldsymbol{e} \approx \boldsymbol{e}^* = \boldsymbol{u}^h - \boldsymbol{u}^* \tag{6.1}$$

$$\boldsymbol{e}_\varepsilon \approx \boldsymbol{e}_\varepsilon^* = \boldsymbol{\varepsilon}^h - \boldsymbol{\varepsilon}^* \tag{6.2}$$

$$\boldsymbol{e}_\sigma \approx \boldsymbol{e}_\sigma^* = \boldsymbol{\sigma}^h - \boldsymbol{\sigma}^* \tag{6.3}$$

with $(\bullet)^*$ as the enhanced solution fields. The enhanced solution fields can be determined either by local recovery or by global recovery. Local recovery uses an averaging of the rough solution fields on e.g. element patches. These fields can be derived at nodes, integration points or superconvergent points which improve the solution field. For industrial simulations, local recovering processes are preferred because global recovery, which is based on minimization problems, enlarges the computational costs.
As the XFEM introduces additional degrees of freedom, which have to be considered for a local patch-wise recovery process as well, difficulties arise. If the crack is not included in the patch but some nodes are enriched, the additional degrees of freedom cannot be handled to resolve an enhanced solution field. A possible solution is the extended moving least squares approach of BORDAS *et al.* (28; 29). Within this approach large moving least squares bases are considered. Thus, this approach also leads to rather large computational costs.
The applied recovery based error estimation technique (122; 101) is based on a global recovery process. Local and global error indicators for the measurement of the mesh quality and the quality of the error estimator are introduced. A mixed mode example with validation character for the stress recovery process is also given.

6.3.1 Recovery Based Error Estimation Technique

The applied discretization error estimation technique without guaranteed bounds is based on the method of ZIENKIEWICZ AND ZHU of 1987 (162). The difference lies in the stress smoothing technique. ZIENKIEWICZ AND ZHU projected the stresses onto the nodes and interpolated the nodal values within each element for the recovering process of the enhanced solution field. Other local smoothing methods to evaluate an enhanced stress field were proposed by HINTON AND CAMPBELL (79). They presented local as well as global stress smoothing based on a least squares approach. A local smoothing technique has not been applied to the XFEM, because a recovery technique based on patches is not applicable without a special treatment of the enriched nodes, cf.figure 6.1. There, in gray a patch of 2D elements for local stress recovering with some nodes of the patch enriched, but without the crack inside the patch is shown. The enrichments have to be interpreted for the stress smoothing within the patch which is not possible without a consideration of the crack evoking the enrichments. Therefore, the enhanced stresses will be recovered within a global procedure. Within this approach each stress component is smoothed separately. The stress recovering process presented in (162) is modified to include specialties of fracture mechanics as e.g. the

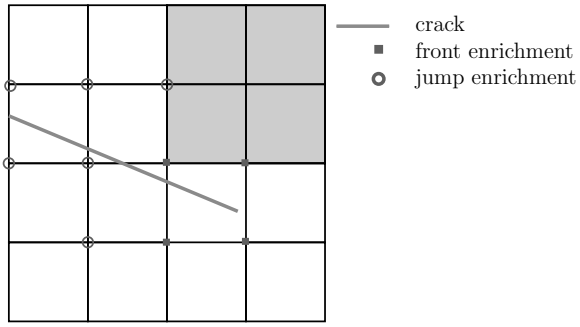

Figure 6.1: A patch of elements for local stress recovery with some enriched nodes, but without a crack inside the patch.

stress singularity at a crack front. For the enriched field new ansatz functions including the asymptotic analytical solution field are chosen. Thus, a linear combination of the asymptotic solution fields of mode I, mode II and mode III can be reproduced for linear elastic fracture mechanics. For fracture mechanics problems combined with ideal plastic material behavior the analytic solution field is unknown. Nevertheless, a similar ansatz as for the linear elastic case is implemented. As shown by MOËS AND BELYTSCHKO this assumption is reasonable for the ideal plasticity (109). The front enrichment functions $g_{ij,k}$, defined for each stress component ij and belonging to either mode I ($k = 1$), mode II ($k = 2$) or mode III ($k = 3$), are chosen to be

$$g_{11,1} = r^{\beta-1} \cos\left(\frac{\varphi}{2}\right) \left(1 - \sin\left(\frac{\varphi}{2}\right) \sin\left(\frac{3\varphi}{2}\right)\right) \tag{6.4}$$

$$g_{11,2} = r^{\beta-1} \sin\left(\frac{\varphi}{2}\right) \left(2 + \cos\left(\frac{\varphi}{2}\right) \cos\left(\frac{3\varphi}{2}\right)\right) \tag{6.5}$$

$$g_{22,1} = r^{\beta-1} \cos\left(\frac{\varphi}{2}\right) \tag{6.6}$$

$$g_{22,2} = r^{\beta-1} \sin\left(\frac{\varphi}{2}\right) \tag{6.7}$$

$$g_{33,1} = r^{\beta-1} \cos\left(\frac{\varphi}{2}\right) \left(1 + \sin\left(\frac{\varphi}{2}\right) \sin\left(\frac{3\varphi}{2}\right)\right) \tag{6.8}$$

$$g_{33,2} = r^{\beta-1} \sin\left(\frac{\varphi}{2}\right) \cos\left(\frac{\varphi}{2}\right) \cos\left(\frac{3\varphi}{2}\right) \tag{6.9}$$

$$g_{12,3} = r^{\beta-1} \sin\left(\frac{\varphi}{2}\right) \tag{6.10}$$

$$g_{23,3} = r^{\beta-1} \cos\left(\frac{\varphi}{2}\right) \tag{6.11}$$

$$g_{13,1} = r^{\beta-1} \cos\left(\frac{\varphi}{2}\right) \cos\left(\frac{\varphi}{2}\right) \cos\left(\frac{3\varphi}{2}\right) \tag{6.12}$$

$$g_{13,2} = r^{\beta-1} \cos\left(\frac{\varphi}{2}\right) \left(1 - \sin\left(\frac{\varphi}{2}\right) \sin\left(\frac{3\varphi}{2}\right)\right) \tag{6.13}$$

$$g_{11,3} = g_{22,3} = g_{33,3} = g_{12,1} = g_{12,2} = g_{23,1} = g_{23,2} = g_{13,3} = 0 \tag{6.14}$$

with $\beta = 1/2$ in the linear elastic case and $\beta = 2$ in the linear elastic ideal plasticity. The enhanced stress tensor $\boldsymbol{\sigma}^*$ at an arbitrary point within Ω is derived using an interpolation of nodal values $\boldsymbol{\sigma}_I^*$ with the standard FE shape functions N_I and the respective enrichment terms

$$\begin{aligned}\boldsymbol{\sigma}^* &= \sum_{I=1}^{n_n} N_I(\boldsymbol{x})\boldsymbol{\sigma}_I^* + \sum_{J=1}^{n_n} N_J(\boldsymbol{x})H(\boldsymbol{x})\boldsymbol{\tau}_J^* + \sum_{K=1}^{n_n} N_K(\boldsymbol{x}) \left(\sum_{M=1}^{3} \boldsymbol{g}_{,M}(\boldsymbol{x})\boldsymbol{\omega}_{KM}^* \right) \\ &= \hat{\boldsymbol{N}}_I^* \hat{\boldsymbol{\sigma}}_I^*. \end{aligned} \tag{6.15}$$

Here, $\boldsymbol{\sigma}_I^*$ are the nodal values connected to the standard stress field, $\boldsymbol{\tau}_J^*$ are additional nodal values belonging to the jump enriched parts and $\boldsymbol{\omega}_{KM}^*$ correspond to the front enriched nodes. To simplify the notation $\boldsymbol{\sigma}^* = \hat{\boldsymbol{N}}_I^* \hat{\boldsymbol{\sigma}}_I^*$ with

$$\hat{\boldsymbol{N}}_I^* = \begin{pmatrix} N_I \\ N_J H \\ N_K \boldsymbol{g}_{,1} \\ N_K \boldsymbol{g}_{,2} \\ N_K \boldsymbol{g}_{,3} \end{pmatrix}, \quad \hat{\boldsymbol{\sigma}}_I^* = \begin{pmatrix} \boldsymbol{\sigma}_I^* \\ \boldsymbol{\tau}_J^* \\ \boldsymbol{\omega}_{K1}^* \\ \boldsymbol{\omega}_{K2}^* \\ \boldsymbol{\omega}_{K3}^* \end{pmatrix} \tag{6.16}$$

is used in the following. Only the standard enrichment scheme is used instead of the enrichment scheme for the corrected XFEM.
The enhanced nodal stresses can be recovered with a least squares method and thus by solving the minimization problem

$$\int_\Omega \left(\boldsymbol{\sigma}^* - \boldsymbol{\sigma}^h\right) \cdot \left(\boldsymbol{\sigma}^* - \boldsymbol{\sigma}^h\right) \, \mathrm{d}\Omega \rightarrow \min. \tag{6.17}$$

For the interpolation of the stress fields the new ansatz functions $\hat{\boldsymbol{N}}^*$ are used. Thus, the minimization problem can be rewritten as

$$\int_\Omega \hat{\boldsymbol{N}}_J^{*T} \hat{\boldsymbol{N}}_I^* \, \mathrm{d}\Omega \, \hat{\boldsymbol{\sigma}}_I^* = \int_\Omega \hat{\boldsymbol{N}}_J^* \boldsymbol{\sigma}^h \, \mathrm{d}\Omega. \tag{6.18}$$

The components $\boldsymbol{g}_{,M}$ resulting from the asymptotic analytical solutions of the three opening modes differ for each stress component. Therefore, the left-hand side of equation (6.18) is different for the recovering process of each stress component. Thus, the matrix resulting from the left-hand side of equation (6.18) cannot be stored after the first evaluation, but has to be inverted for each stress component separately.
The already mentioned error estimation technique of DUFLOT AND BORDAS (47) operates in a similar way. Their error estimation is based on a strain smoothing technique instead of a stress recovering procedure. As new ansatz functions for the strain field near a crack front the derivatives of the branch functions (4.16) are considered. The matrix is the same for all strain components and has thus to be inverted only once. Nevertheless, the enhanced strains can be evaluated for every component successively. Thus, the applied stress recovery technique has, with the mixed mode ansatz, a subset of functions in the stress smoothing part, compared to

the strain smoothing in (47) for LEFM. However, the presented stress recovering technique can easily be extended to inelastic material models such as plasticity as shown in section 7.1 for a 2D example. A strain smoothing technique would not lead to the desired results if a strain decomposition into different parts is included in the material model description.

6.3.2 Local Error Measures

The goal of error estimation is to reduce the global error during the simulation while keeping the computational costs low. To achieve low computational costs adaptive mesh refinement strategies or an application of higher polynomial orders for the elements with a large error are reasonable. These strategies are usually based on local error measures. The element error based on the recovered enhanced stress field can be derived in the L_2 norm for stresses and is written as

$$\|\boldsymbol{e}_{\sigma}^{*}\|_{L_2(\Omega_e)} = \sqrt{\frac{1}{\Omega_e}\int_{\Omega_e} (\boldsymbol{\sigma}^h - \boldsymbol{\sigma}^*)^T \cdot (\boldsymbol{\sigma}^h - \boldsymbol{\sigma}^*)\,\mathrm{d}\Omega_e}. \tag{6.19}$$

This error does not allow a general criterion for mesh refinement as the maximum depends on the overall problem description. Thus, a fixed criterion for mesh refinement has to be adapted dependent on the current problem. A relative local error leads to comparable results of the discretization error indicator for different meshes and element sizes and enables a general mesh refinement criterion. The L_2 norm error can be reformulated as a relative local error indicator defined as

$$\eta_e = \frac{\|\boldsymbol{e}_{\sigma}^{*}\|_{L_2(\Omega_e)}}{\max\limits_{k}\|\boldsymbol{\sigma}^*\|_{L_2(\Omega_e^k)}} \times 100\% \qquad \forall \quad 1 \leq k \leq n_e, \tag{6.20}$$

where $\max\limits_{k}\|\boldsymbol{\sigma}^*\|_{L_2(\Omega_e^k)}$ is the maximum L_2 norm of the recovered stress field detected in all elements n_e of the mesh. With the local relative error a mesh refinement based on different criteria is possible. Some possibilities are

$a)$ The first i-elements with the largest local errors are refined.

$b)$ Refinement of a percental number of elements $n_{e\,ref}$.

$c)$ All elements j with a relative error larger than a threshold value η_{tol} are refined.

In case of refinement criterion $a)$ the number of elements to refine depends on an error criterion η_{sum} which defines the sum of the local errors for refinement $\eta_{sum} = \sum_i \eta_{e\,i}$. Even if the relative error distribution leads to comparable results of the error distribution for different meshes, the relative error within one element can be extremely high. Thus, $\eta_{sum} = 50\,\%$ could lead to a refinement of only a few elements with local errors near e.g. 20 %. This refinement criterion is thus excluded in the presented work.
The refinement of a percental number of elements $n_{e\,ref}$ beginning with the elements with the largest local errors based on refinement criterion $b)$ can also introduce further difficulties. If the initial mesh is chosen too coarsely, the number of elements which have to be refined may

not be large enough to resolve the stress distribution around the crack front. As for further refinement steps the amount of elements is restricted to a percental value, the non-refined elements will not be reduced in size. An advantage of the method is the a priori known number of elements within each refinement step. For comparison $n_{eref} = 15\%$ is chosen as a possibility within the mixed mode analysis, introduced in section 6.3.4.
Refinement criterion $c)$ is applied within this work where different threshold values are used. All elements j with $\eta_j \geq \eta_{tol}$ are refined. Within fracture mechanics the global minimum error which can be reached is restricted in correlation with the chosen threshold value. For large values η_{tol} only the crack front elements may be refined in each refinement step, but surrounding elements remain untouched. Results are given in section 6.3.4 for mixed mode analysis,.

6.3.3 Global Error Measures

The local mesh refinement leads to a decreasing global error. The global error analogously to the error estimator of ZIENKIEWICZ AND ZHU (162) extended to the XFEM is the estimated error in the energy norm and reads

$$\|\boldsymbol{e}^*\|_E = \sqrt{\frac{1}{\Omega}\int_\Omega (\boldsymbol{\sigma}^h - \boldsymbol{\sigma}^*) : \mathbb{C}^{-1} : (\boldsymbol{\sigma}^h - \boldsymbol{\sigma}^*)\,\mathrm{d}\Omega} \tag{6.21}$$

with the material tangent $\mathbb{C}$. For the XFEM no proof for an upper bound for this error estimation type is given. However, for the ZIENKIEWICZ AND ZHU error estimator for classical FE analysis an upper bound can be guaranteed (33). Within this work the global error measure will lead to an error indicator due to the missing proof of upper bound properties. Nevertheless, with the effectivity index Θ for examples with known analytical solutions, it can be shown that the error indication for the global measure performs in an acceptable range. The effectivity index is defined as

$$\Theta = \frac{\|\boldsymbol{e}^*\|_E}{\|\boldsymbol{e}\|_E}. \tag{6.22}$$

Thus, a value below one means an underestimation of the error and a value larger than one an overestimation. Following (146) a good error indicator is achieved if the effectivity index holds $0.8 \leq \Theta \leq 1.2$.

6.3.4 Numerical Example - Mixed Mode Loading

To analyze the usability of the local and global error measures for mesh refinement a mixed mode loading, i.e. a linear combination of mode I, mode II and mode III loading, is applied. For this example with $K_I = K_{II} = K_{III} = 1$ analytical solutions are known and thus, the effectivity index is computable. For the setup cf, figure 6.2a. A linear elastic material with a YOUNG's modulus of $E = 200$ GPa and a POISSON's ratio of $\nu = 0.3$ is used. The initial mesh is chosen to consist of $35 \times 10 \times 35$ elements. For the overall domain boundary DIRICHLET boundary conditions are prescribed. The evaluation of the boundary conditions

is achieved using the multiscale technique (chapter 5). Therefore only one element is defined to be a coarse scale element. This element is enriched with front enrichments using all four enrichment functions of equation (4.16). The boundary conditions for this coarse scale element are the analytically prescribed conditions for all degrees of freedom are defined. Thereafter, for the fine scale, all nodes on the fine scale boundary get prescribed boundary conditions equivalent to the coarse scale displacement field.

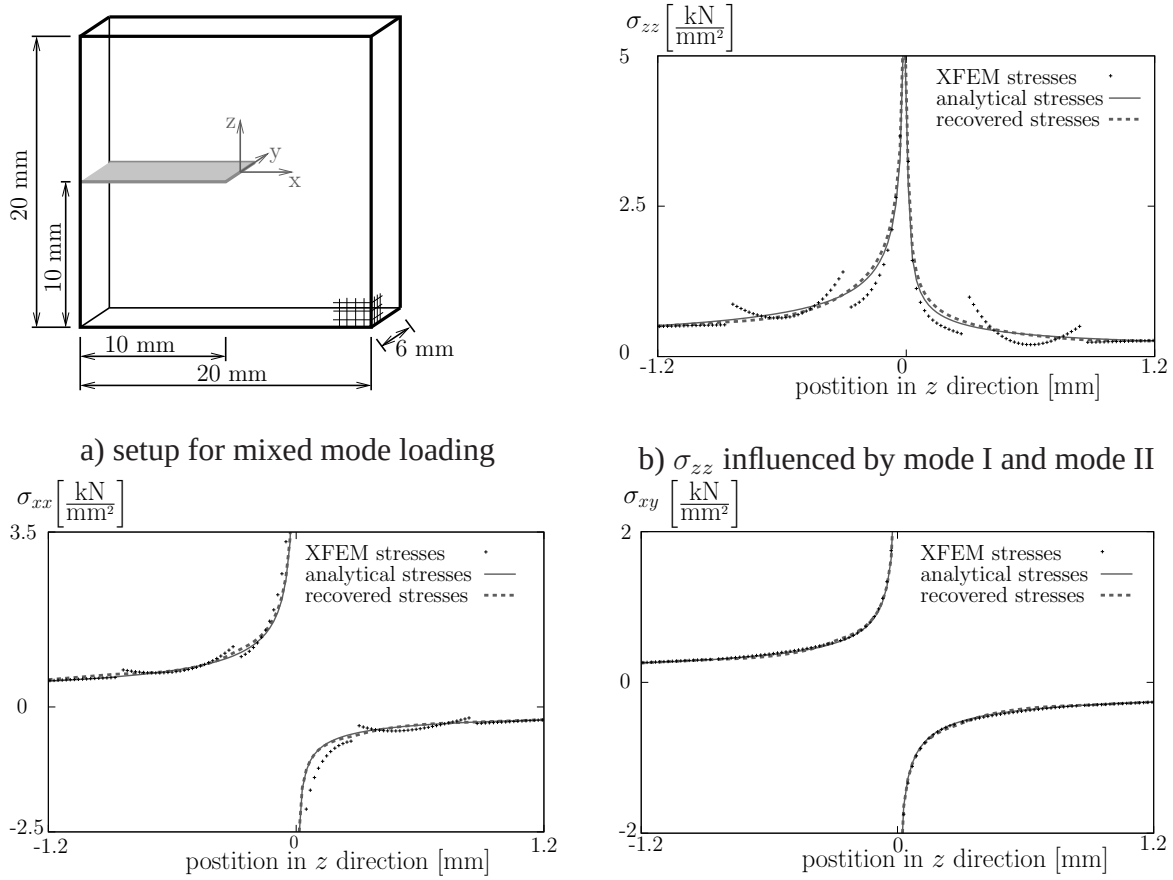

a) setup for mixed mode loading

b) σ_{zz} influenced by mode I and mode II

c) σ_{xx} influenced by mode I and mode II

d) σ_{xy} influenced by mode III

Figure 6.2: In a) the geometrical setup for the mixed mode loading is shown. On the entire surface of the domain DIRICHLET boundary conditions enforce a crack opening for a linear combination of mode I, II and III. The mesh has $35 \times 10 \times 35$ elements as indicated in the right corner in a). In b-d different stress components along a cut in z-direction perpendicular to the crack front ($x = 0.0$mm, $y = 0.003$mm) are shown. The XFEM stresses, the analytical stresses and the recovered enhanced stresses are plotted.

The different stress components are influenced by the different modes. σ_{11} and σ_{33} are influenced by mode I and mode II and e.g. σ_{12} is influenced by mode III. For these stress components the asymptotic analytical solution $\boldsymbol{\sigma}$, the XFEM solution $\boldsymbol{\sigma}^h$ and the recovered enhanced solution $\boldsymbol{\sigma}^*$ are shown in figures 6.2b-d. Especially for σ_{33} and σ_{11}, (figures 6.2b and 6.2c), the jumps in the XFEM stresses at the element edges are clearly visible. Additionally, the smoothness of the recovered solution can be recognized as well as the fact that

this solution is closer to the analytical solution than the XFEM solution.
For the initial mesh the approximated global error indicator in the energy norm as well as the effectivity index can be computed. As shown in figure 6.3 the effectivity index is 0.992 and thus indicates a slight underestimation of the exact error. But, as the effectivity index is close to one, the approximated error indicator may be useful for further simulations. The

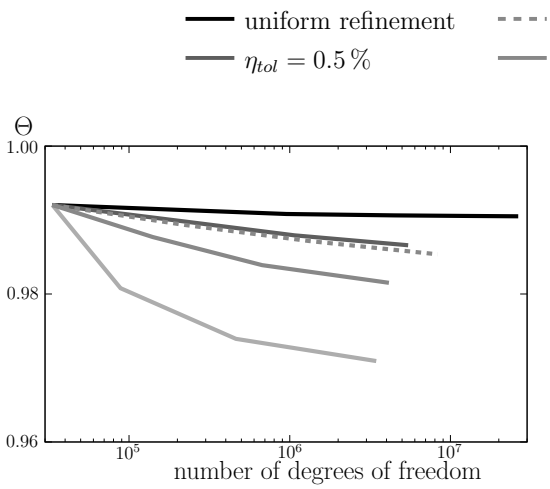

Figure 6.3: Effectivity index.

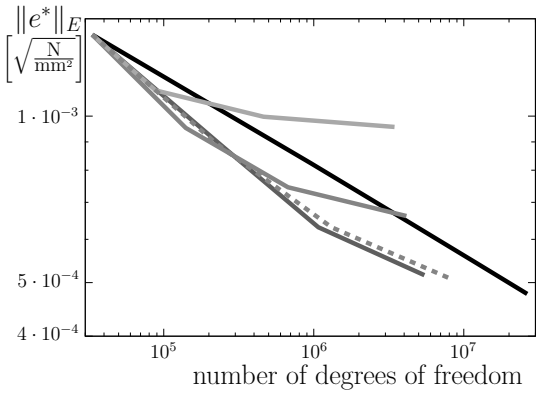

Figure 6.4: Approximated error in the energy norm for different refinements of the mixed mode initial mesh.

global estimated error in the energy norm for the initial mesh is $\|\boldsymbol{e}^*\|_E = 1.40 \cdot 10^{-3}\sqrt{\frac{\mathrm{N}}{\mathrm{mm}^2}}$. The resulting number of degrees of freedom for a simulation with the initial mesh is about 33,000 degrees of freedom. With a uniform refinement the global error in the energy norm can be reduced to $4.77 \cdot 10^{-4}\sqrt{\frac{\mathrm{N}}{\mathrm{mm}^2}}$. This requires solving for about 26,4 million degrees of freedom. Thus, the computational costs are drastically increased in terms of storage and computational time.
The goal of adaptive refinement is to improve the global error in the energy norm while keeping low computational costs. For comparison of the efficiency and accuracy of the adaptive mesh refinement, different refinement criteria based on the local error indicator η_e are chosen. In one simulation $n_{eref} = 15\%$ is chosen. Additionally, three simulations based on refinement criterion $c)$ with $\eta_{tol} = 3\%$, $\eta_{tol} = 1\%$ and $\eta_{tol} = 0.5\%$ respectively are enforced. For each of those simulations three refinement steps are performed. Regarding the effectivity index for all simulations (figure 6.3) an adaptive mesh refinement based on the defined error indicator is reasonable. All results for the effectivity index with a minimal value of $\Theta = 0.9709$ are still in an acceptable range. With the applied initial mesh the refinement based on criterion $b)$ with a refinement of 15 % of all elements leads to a reduction of the computational costs while the accuracy of the global solution is improved as can be seen by the convergence of the global error in the energy norm (figure 6.4). For refinement criterion $c)$, a threshold value of $\eta_{tol} = 3\%$ does not lead to an improved solution as the refined domain is only in the vicinity of the crack front. Both other threshold values reach a solution with the desired results: more precise results with low computational effort.

Based on these results, this discretization error indicator is used for further applications in chapter 7.

6.4 Model Adaptivity

The presented mesh adaptivity leads to a mesh with a nearly equally distributed relative discretization error indicated for a given physical problem. However, beside the main crack small cracks have to be considered. To model fine scale cracks computationally efficiently, the application of the multiscale projection technique (section 5) is reasonable. Thus, the fine scale cracks are ad hoc not inherent in the results of the discretization error estimation on the coarse scale. To accurately include the effect of the fine scale cracks, while keeping the computational effort on all scales reasonable, the fine scale domain for the multiscale simulation has to be defined in a smart way. One possibility is to choose the fine scale domain based on heuristic experiences, e.g. a tubular shape (circular in 2D) around the main crack front as applied in (98; 99). Another choice is the definition of the fine scale domain based on more physically motivated aspects such as regions of high stress gradients. This method is presented in the next paragraphs. The fine scale domain should depend on the overall geometry and the loads applied to the entire domain as well as on the considered material but not on the discretization of the system.

6.4.1 Model Indicator for the Fine Scale Domain

GRACIE AND BELYTSCHKO (68) proposed a coupling of XFEM and atomistic models using a bridging domain method. Around crack fronts and inclusions the atomistic model is introduced based on heuristic definitions. They already introduced the necessity of model adaptive schemes to enable crack propagation within their method. In a more general context of the FEM ,STEIN *et al.* (138) defined a model error in the energy norm for stresses. The model adaptivity is based on a nested sequence of models. A goal oriented model error for concurrent multiscale methods to improve some quantities of interest is proposed by ODEN *et al.* (114).
Regions with high strain or stress gradients, e.g. near crack fronts or re-entrant corners, are regions where crack initiation or crack propagation are most expected. To identify these regions the stress gradient for each finite element has to be evaluated. For trilenar hexahedral elements, which are applied in this work, the stress gradient cannot be evaluated directly, because the shape functions are not sufficient differentiable. One possibility to evaluate the stress gradient was presented by TEMIZER AND WRIGGERS (148) in 2011. They used cell-centered data achieved by a complementary triangulation between the cell center points. In the present work a smoothed stress field, cf. equation (6.15), which can be used for the evaluation of the stress gradient already exists. Thus, the recovered enhanced stress field is applied to achieve the stress gradient. As the stress gradient for each stress component differs, the L_2 norm of the stress gradient field is taken to detect elements that need to be included in the fine scale domain. The L_2 norm of the stress gradient for each element is evaluated at the center of the element except XFEM elements. For the evaluation of the L_2 norm of the stress gradient within an XFEM element all integration points ip used within

that element for the FE simulation are considered. Then the L_2 norm of the stress gradient is

$$\|\nabla\boldsymbol{\sigma}^*\|_{L_2} = \frac{\sum_{ip}\|\nabla\boldsymbol{\sigma}^*_{ip}\|_{L_2}\cdot w_{ip}}{\sum_{ip} w_{ip}} \tag{6.23}$$

with the weighting factors w_{ip} of the related integration point. All coarse scale elements with

$$\|\nabla\boldsymbol{\sigma}^*\|_{L_2} > \|\nabla\boldsymbol{\sigma}\|_{\mathrm{tol}} \tag{6.24}$$

are included in the fine scale domain. The L_2 norm of the stress gradient is chosen for the identification of the fine scale domain as these high gradients characterize regions where crack initiation and crack propagation are most expected. These regions are typically near crack fronts, close to localized contact or boundary loads or around re-entrant corners, among others. The threshold value $\|\nabla\boldsymbol{\sigma}\|_{\mathrm{tol}}$ is chosen according to heuristic values which were applied for the tubular radius chosen in the approach of LOEHNERT *et al.* (98; 99).
To reduce the influence of the discretization error on the model error the global discretization error should be less than the global model error (138). Here the elements exceeding the mesh refinement criterion for the discretization error indicator are expected to be included in the fine scale domain determined by applying the stress gradient norm criterion (6.24).

6.4.2 Numerical Validation

To analyze the model indicator a test setup as shown in figure 6.5a is analyzed. To show convergence rates with a simplified validation, a nearly plain stress setup is chosen. The linear elastic material parameters are $E = 200\,\mathrm{GPa}$ and $\nu = 0.3$. The reference mesh is 105×105 elements (one element in y direction). A load of $F = 400\,\mathrm{N}$ is applied evenly at the top and at the bottom distributed on all top and bottom surface nodes. DIRICHLET boundary conditions to avoid rigid body motions are applied (gray bars in figure 6.5a). The deformed configuration for the reference mesh, load and material and the stress σ_{33} are plotted in figure 6.5b.
For the reference model, the distribution of the local relative error is shown in figure 6.6a. The elements with a relative error larger than one percent are concentrated around the crack front and restricted to a rather small area. Thus, the setup is useful as a reference solution. $\|\nabla\boldsymbol{\sigma}^*\|_{L_2}$ is presented in figure 6.6b.
To visualize the discretization independence of the model indicator the L_2 norm of the stress gradient is evaluated along the z axis perpendicular to the crack for different discretizations. The results are presented in figure 6.7a. In 6.7b the effect of a modified block size in z direction with the same element size as in the reference setup is presented. For the same load case the model indicator leads to similar results for regions where a fine scale domain should be applied. As fine scale domain e.g. elements with $\|\nabla\boldsymbol{\sigma}^*\|_{L_2} > 20\frac{\mathrm{kN}}{\mathrm{mm}^3}$ should be selected. For different materials with other POISSON ratios the choice of elements may be different, see figure 6.7c. As expected a modification of the applied load figure 6.7d leads to a larger change in the quantity of $\|\nabla\boldsymbol{\sigma}^*\|_{L_2}$. Based on the results the model indicator seems to be reasonable for further simulations to determine the fine scale domain. Further examples are presented in chapter 7.

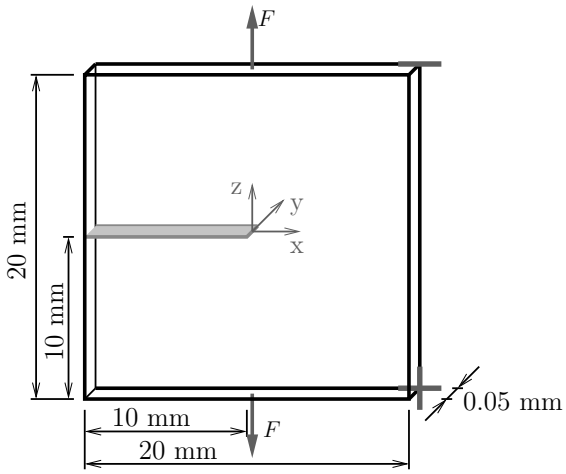

a) setup with boundary constraints, additional the back of the domain is fixed in y direction

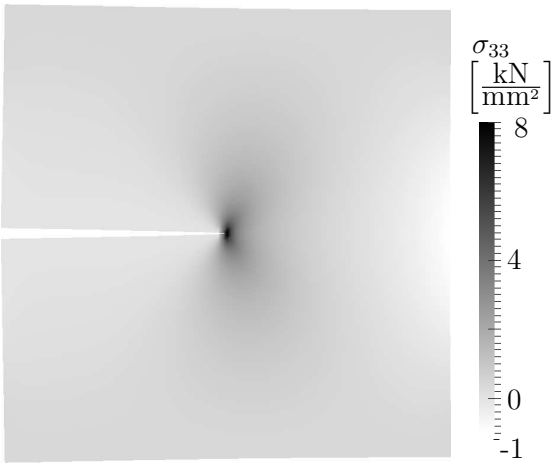

b) deformed configuration and distribution of σ_{33}

Figure 6.5: Setup for the numerical validation of the model indicator.

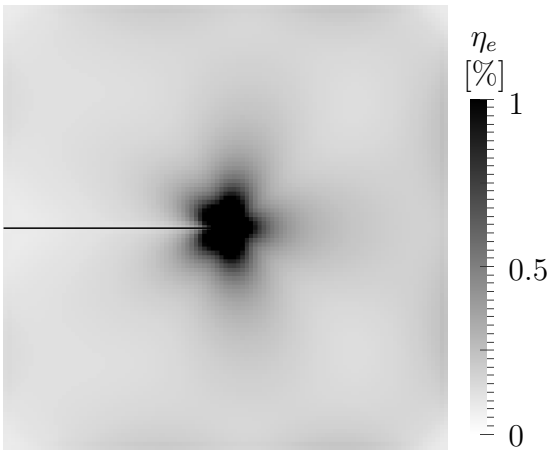

a) relative error η_e on element level

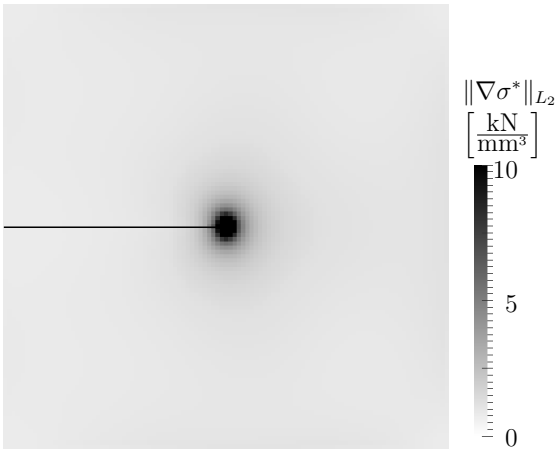

b) $\|\nabla\boldsymbol{\sigma}^*\|_{L_2}$ element wise

Figure 6.6: Local distribution of a) the relative discretization error and b) the L_2 norm of the stress gradient. Crack marked in black.

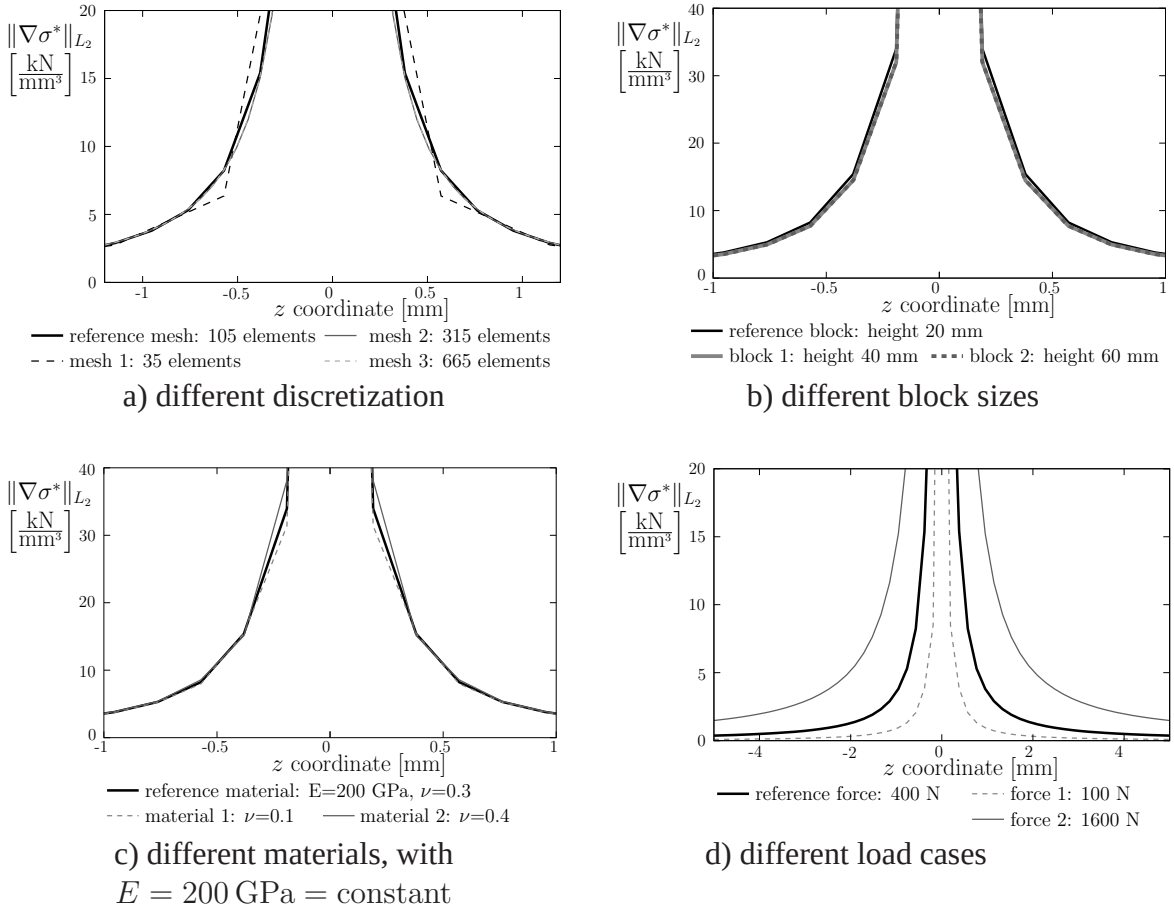

a) different discretization

b) different block sizes

c) different materials, with $E = 200\,\text{GPa} = \text{constant}$

d) different load cases

Figure 6.7: Distribution of the L_2 norm of the stress gradient considering different variations of the reference setup.

Chapter 7

Numerical Results

The presented extensions to the XFEM are applied to different examples. The discretization error estimation technique combined with inelastic material behavior is presented in section 7.1. In a further example the mesh adaptivity is applied to arbitrary meshes and arbitrary cracks in 3D in section 7.2. Thereafter, an application of the discretization adaptivity on two scales is presented. The fine scale domain is determined using the model indicator (section 7.3). In a final example (section 7.4) the application of the presented techniques to experimentally determined crack configurations (cf. 3.2.2) is shown. With a geometrical a priori mesh refinement the experimental setup can be modeled and the resulting discretization error helps to assess the a priori refinements. In combination with the model adaptivity, the influence of small cracks on a main crack is analyzed in a twoscale simulation with mesh adaptivity on both scales.

7.1 Mesh Adaptivity Applied to 2D Plasticity

The application of the adaptive mesh refinement based on the discretization error indicator of section 6.3 to generally inelastic material behavior is shown in (122) and presented in the following. The material description for the applied linear elastic ideal plastic material is according to section 2.3. The VON MISES flow rule is used to distinguish between pure elastic or plastic material behavior. The linear elastic ideal plastic material is given with a YOUNG's modulus of $E = 200\,\mathrm{GPa}$, a POISSON's ratio of $\nu = 0.3$ The yield strength $Y_0 = 104\,\mathrm{MPa}$ is chosen for the flow rule. A setup with two cracks in 2D as presented in figure 7.1 is analyzed with respect to the accuracy after adaptive mesh refinement.
Before doing so, the XFEM stress field and the enhanced recovered stress field need to be analyzed. As no analytic solution exists, only these two stress fields can be compared. Since the strain field is split into an elastic and a plastic part (equation (2.34)), and their resulting split is only known at the integration points, it is useful to analyze the stresses at the integration points. For this application this analysis is preferred instead of a projection of the strains onto a line segment as applied for the mixed mode loading example shown in figure 6.2. The stresses in vertical direction σ_{22} are visualized at the integration points in 7×7 elements around the lower crack tip for a discretization of 42×84 elements, displayed in figure 7.2. As expected, the XFEM stress field has some stress jumps at element edges,

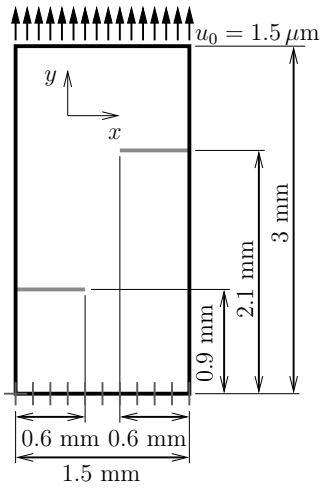

Figure 7.1: Setup for a 2D analysis to show the applicability of the discretization error indicator to generally nonlinear material behavior. Plain strain is assumed and a total displacement of $u_0 = 1.5\,\mu\text{m}$ is applied at the top. The bottom is fixed in y direction and the left bottom corner additionally in x direction to avoid rigid body motions. An initial mesh of 42×84 elements is chosen.

while the enhanced stress field (cf. equation (6.15)) is smooth with a stress concentration close to the crack tip.

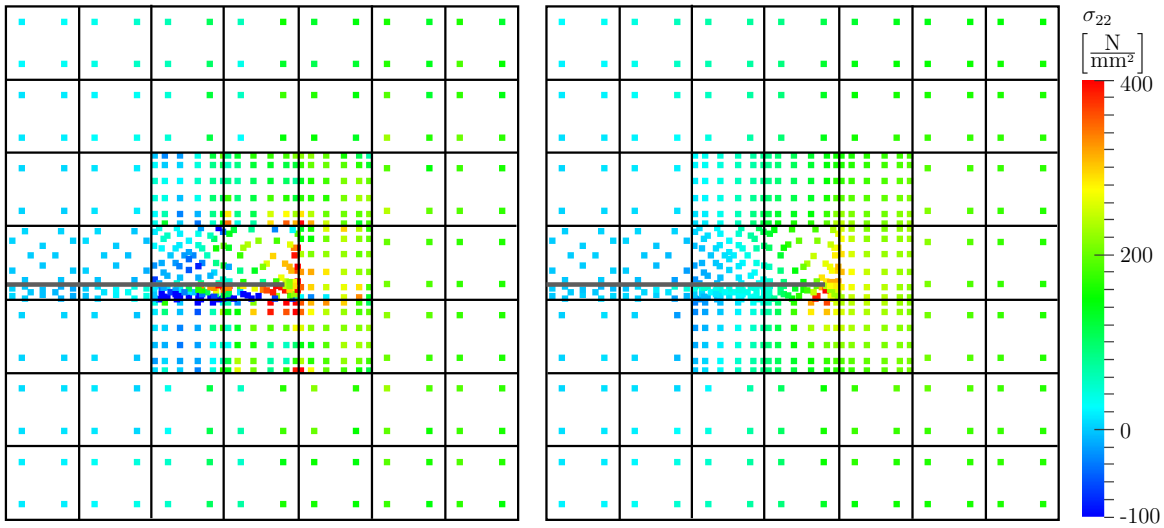

a) XFEM stress field b) recovered stress field

Figure 7.2: a) XFEM and b) recovered stress field at the integration points around the lower crack tip.

The results of a uniform fine mesh with 126×252 elements and a comparable adaptive refined mesh are shown in figure 7.3. For the adaptive refinement a starting mesh of 14×28 elements is chosen. In the first refinement step, nearly all elements have to be refined for a threshold value $\eta_{tol} = 1\%$. A refined element leads to 3×3 new elements. A second refinement step with the same threshold value and the same refinement is enforced. Regarding the stress σ_{22} as well as the local error distribution η_e, the simulation with the adaptively refined mesh leads to good results while having lower computational costs, which are proportional to the number of degrees of freedom. The simulation with the adaptively refined mesh has about 18,000 degrees of freedom while the uniform fine mesh has approximately 65,000 degrees of freedom, i.e. a factor of 3.6. Both simulations lead to similar global errors in the energy

norm (cf. equation (6.21)). The global error of the uniform refined mesh is

$$\|\boldsymbol{e}^*\|_E \approx 3.9 \cdot 10^{-3} \sqrt{\frac{\mathrm{N}}{\mathrm{mm}^2}}$$

while the global error of the adaptively refined mesh is

$$\|\boldsymbol{e}^*\|_E \approx 4.1 \cdot 10^{-3} \sqrt{\frac{\mathrm{N}}{\mathrm{mm}^2}}.$$

The results of the error in the energy norm are marked with crosses in figure 7.4. An analysis of the refined domains leads to the result that the mesh is refined in the domains where plastic strains are recognized. These results as well as the shape of the plastic zone are comparable to the results of RANNACHER AND SUTTMEIER presented in (123) where they analyzed a square disc with a crack. Thus the refinement strategy and the domain of the plastic zone are reasonable.
To show the improvement of the global solution the global error in the energy norm is presented in figure 7.4. The adaptive mesh refinement leads to precise global results while reducing the computational costs compared to a uniform refinement of the mesh.

7.2 Arbitrary Meshes and Cracks in 3D

Academic examples like straight cracks within a block or penny shaped cracks are often used to validate theoretical approaches. As in this work cracks are prescribed with level set functions, which are interpolated within the elements (equation (4.17)), the level sets have to be known at the nodes. The extension from academic examples to examples with arbitrary meshes and cracks is not straightforward. In (45) an update technique for level sets for propagating cracks is presented. Nevertheless, to create arbitrary examples, a level set creation tool has to be developed for this work. Arbitrary crack geometries can easily be created in an explicit way in commercial FE tools like ABAQUS. The crack surface can be meshed with linear triangles. Using this explicit description, the level set values for the nodes of a given FE mesh can be evaluated and thus assigned to an XFEM simulation. In this work the crack description is restricted to two signed distance functions. One is used to describe the crack surface, the other to describe the crack front. An alternative approach using multiple level sets is presented by MOUMNASSI *et al.* (112). Their method enables the representation of sharp edges of the crack surface also inside one element. These sharp edges are excluded here, as the crack representation is restricted to two level sets for each crack. The calculation of level set values according to a geometry prescribed by a surface mesh of triangles (figure 7.5 for the first level set) is possible in the following order. First of all, nodes directly above or below a triangle of the meshed crack surface get a first level set: The definition of whether the level set value should be positive or negative depends on the normal vector of the triangle. Therefore it is important that the normal vector of each triangle is defined such that there are no jumps in the orientation from one triangle to the next. Secondly, all nodes having the closest distance to a triangle edge and lie above or below it get a first level set value. Nodes close to a triangle surface point (=node of multiple

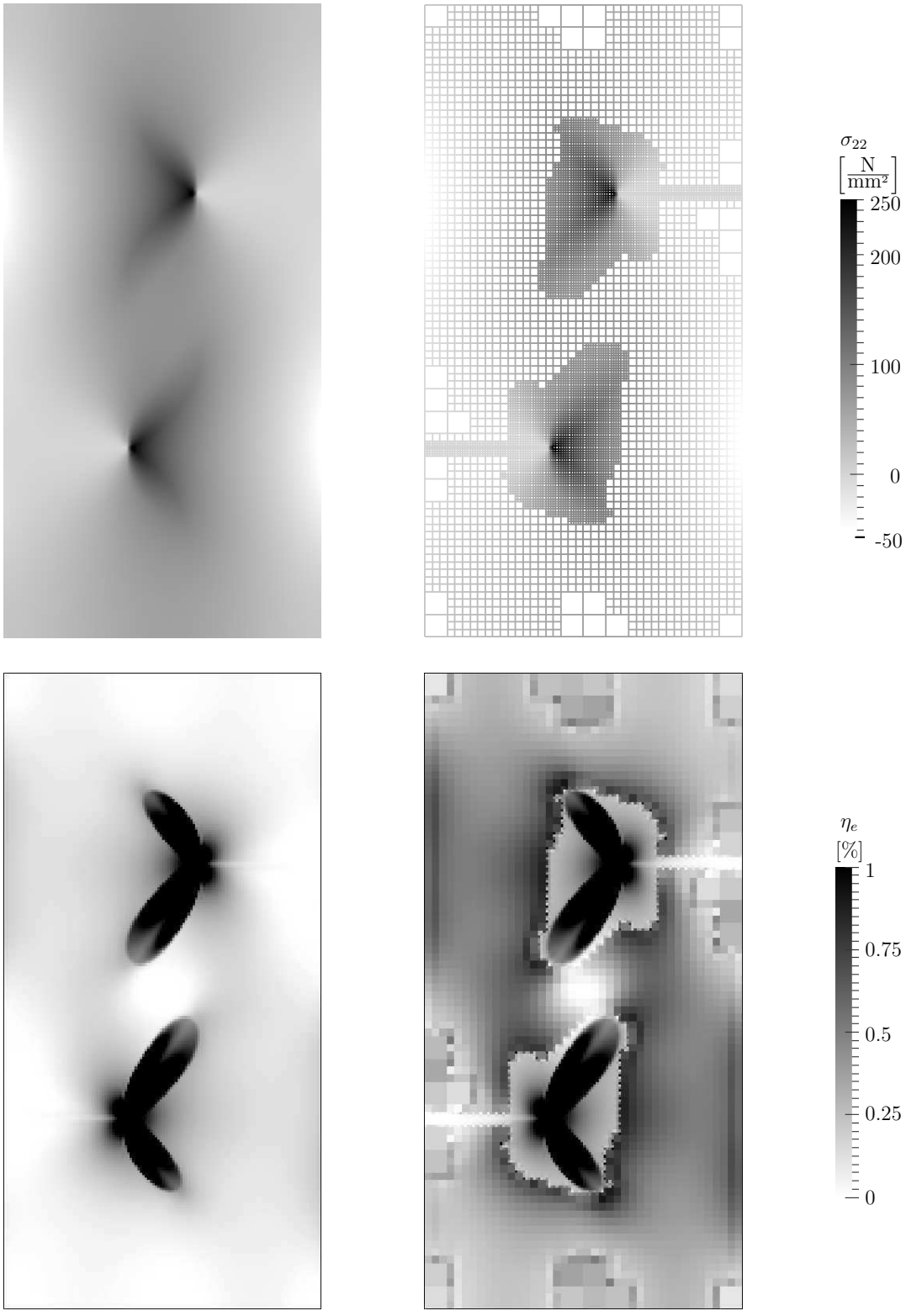

Figure 7.3: Comparison of the stress distribution and the local estimated error distribution in a uniformly refined (left) and an adaptively refined (right) mesh.

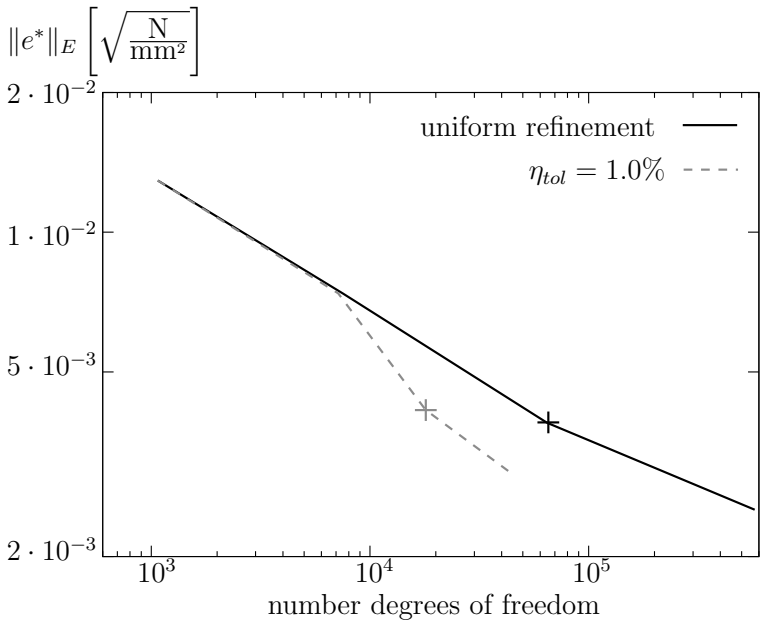

Figure 7.4: Global estimated error in the energy norm. The results presented in figure 7.3 are marked with crosses.

triangles) get a first level set. After these steps, all nodes of the FE mesh below or above the triangles have a first level set. For the XFEM simulation with level sets, all nodes of a crack front element need the first level set function. These missing values are computed during the steps to find the second level sets. The missing first level sets in the crack front elements indicate that the node lies behind the crack front. In the next step, all elements close to a triangle edge which belongs to the crack front get a second level set. If the node has already a first level set, this node lies in front of the crack front. Otherwise it lies behind the crack front. Then additionally, a first level set is evaluated. Finally, all nodes with the closest distance to a point of the crack front instead of a front line segment get a second level set. Again, if necessary, the first level set is also evaluated.

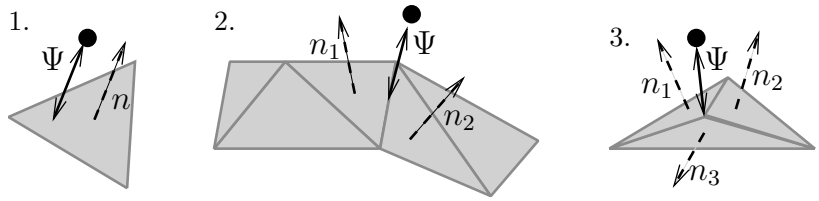

Figure 7.5: Evaluation of the first level set Ψ if the node lies (1.) above a crack surface triangle or (2.) close to a triangle edge or (3.) with the closest distance to a triangle node.

To demonstrate the generality of the proposed method, a mesh with general eight node brick elements and an arbitrary crack geometry are chosen. The setup is presented in figure 7.6 with the mesh sketched at the outer surface. The material parameters are given with $E = 200\,\mathrm{GPa}$ and $\nu = 0.3$. The prescribed displacement at the top of the domain is $u_0 = 0.02\,\mathrm{mm}$. A simulation with two refinement steps with a refinement based on the threshold value $\eta_{tol} = 1\%$ is accomplished. Every element which has to be refined is subdivided into $3 \times 3 \times 3 = 27$ elements. The XFEM enrichments around the crack front are

based on topological enrichment, i.e. only the crack front elements are enriched with the front enrichment functions and the blending elements are enriched to ensure to fulfill the partition of unity in the overall domain(57).

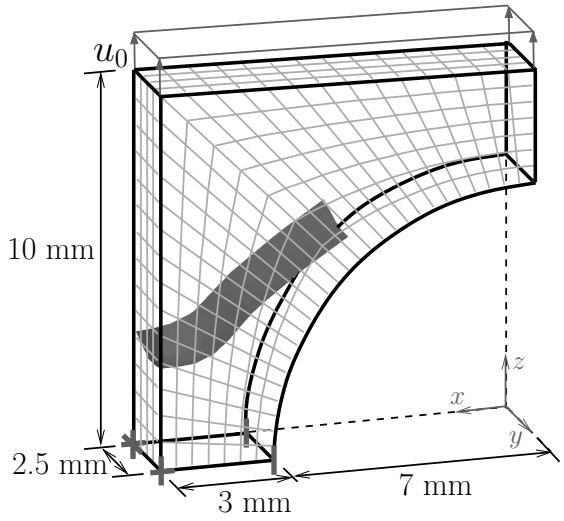

Figure 7.6: Setup with boundary constraints.

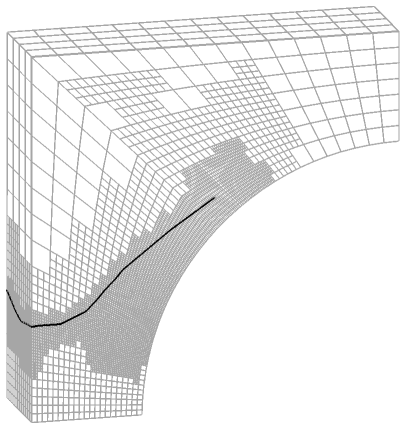

Figure 7.7: Mesh after two refinements for each element with $\eta_e \geq 1\%$.

The mesh at the surface of the body after two refinement steps is shown in figure 7.7. The resulting stress distribution σ_{zz} without mesh refinements is compared to the stress distribution after mesh refinement in figure 7.8. Both figures show the deformed domain scaled with factor 10. The reduction of elements due to adaptive mesh refinement compared to a uniform refinement can be seen in table 7.1. With each refinement step, the estimated global error in the energy norm can be reduced and thus, the results are improved with the adaptive discretization scheme. A refinement of the elements including the crack enables a more precise representation of the crack surface as the new level sets are based on the explicit description of the crack surface based on the triangle mesh.

number of elements (uniform refinement)	number of elements (adaptive refinement)	$\|e^*\|_E$ in $\sqrt{\frac{\mathrm{N}}{\mathrm{mm}^2}}$
784	784	$1.5579 \cdot 10^{-3}$
21,168	13,744	$9.0072 \cdot 10^{-4}$
571,536	163,066	$5.0613 \cdot 10^{-4}$

Table 7.1: Number of elements for uniformly and adaptively refined meshes. Global approximated error in the energy norm based on the recovered stress field for adaptively refined meshes.

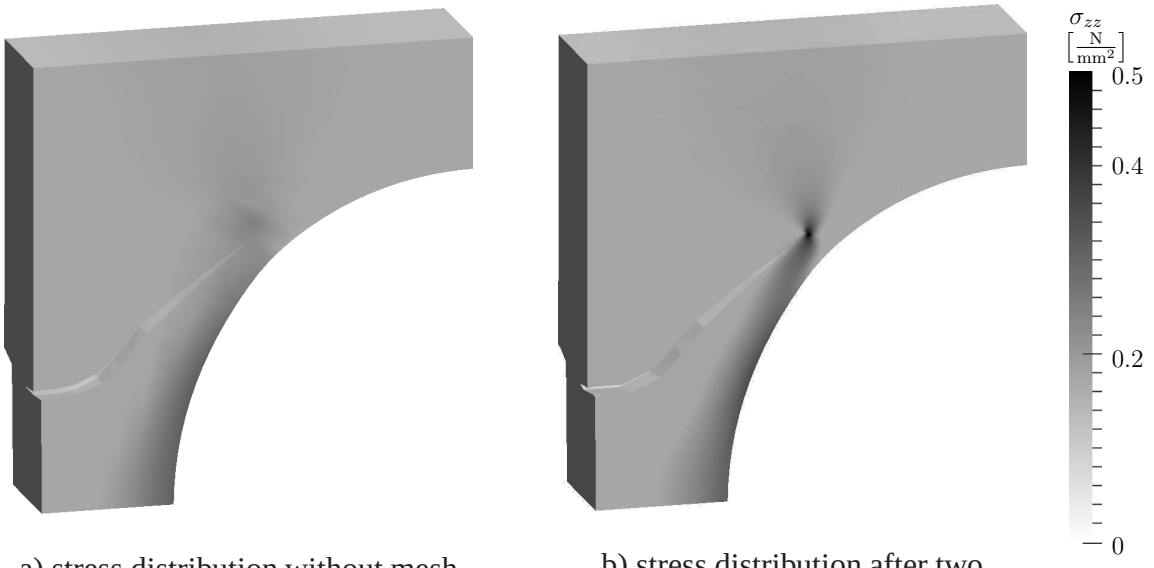

a) stress distribution without mesh refinement

b) stress distribution after two adaptivity steps

Figure 7.8: Distribution of σ_{zz} in the deformed state with the deformation scaled with factor 10.

7.3 Adaptive refinement on two scales

The efficiency resulting from discretization adaptivity on two scales is examplified on a simple test. The block shown in figure 7.9 is discretized with $21 \times 7 \times 21$ elements. The block is fixed at the bottom as indicated with the gray lines in figure 7.9 at the corner nodes. However, all bottom nodes are fixed in the z direction. A displacement of $u_0 = 0.03$ mm in z direction is applied at the top. Two elliptic cracks with a length of 155.50 μm in the y direction and a length of 21.8 μm in the x direction are placed above and below the midpoint of the main crack front. The distance of the ellipse center to the midpoint of the main crack front is 17.38 μm in z direction and $-z$ direction respectively. The material parameters are YOUNG's modulus $E = 82.5\,\frac{\mathrm{N}}{\mathrm{mm}^2}$ and POISSON's ratio $\nu = 0.25$. The following steps are applied during the simulation:

$a)$ Two refinement of the coarse scale with $\eta_{tol} = 3\%$.

$b)$ Estimation of the model indicator to define the fine scale domain.
In former studies the tube around the crack front which included the fine scale was based on heuristic experiments and numerical studies (98; 99). According to those results the fine scale domain is defined in the region with $\|\nabla\boldsymbol{\sigma}\|_{\mathrm{tol}} = 150\frac{\mathrm{N}}{\mathrm{mm}^3}$.

$c)$ One refinement of the fine scale domain with $\eta_{tol} = 3\%$.

The coarse scale explicitely includes the main crack. For the adaptive refinement based on the discretization error indicator (6.20) the results of the single coarse scale simulation are used. Every element, which has to be refined is divided into $3\times3\times3$ elements. The resulting refined coarse scale mesh with 54,000 elements is displayed in figure 7.10. The distribution of the local relative error indicator is shown in figure 7.11. A discretization of the coarse scale

with the mesh size of the smallest elements after the refinement, i.e. an element edge length of 10.9 μm, would lead to 2.25 million elements. Thus, the number of elements required for the coarse scale is reduced by a factor of 42. As the number of elements is approximately proportional to the required computational costs, the refinement of the coarse scale leads to significantly higher efficiency while improving the solution.

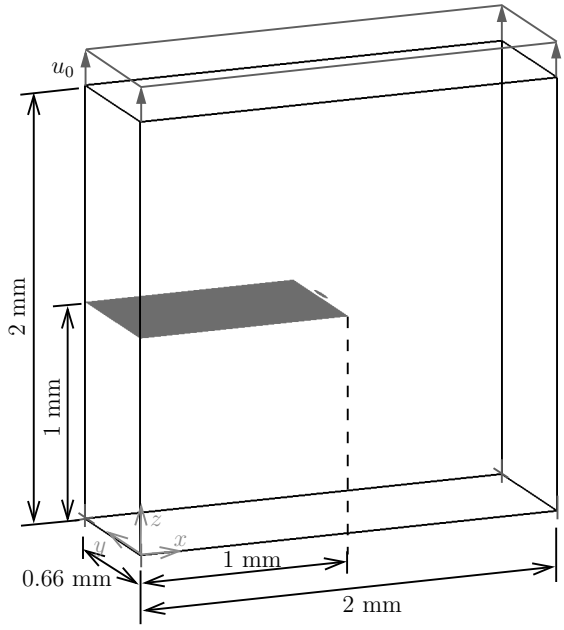

Figure 7.9: Setup for the simulation with discretization and model adaptivity.

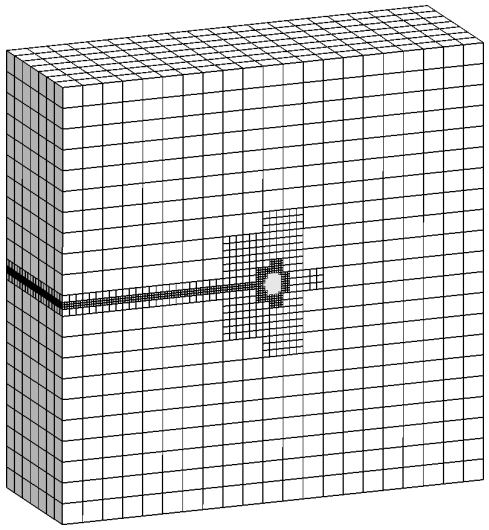

Figure 7.10: Resulting coarse scale mesh after two refinement steps with $\eta_{tol} = 3\%$. The light domain at the crack front is the fine scale domain based on the model indicator with $\|\nabla\boldsymbol{\sigma}\|_{\mathrm{tol}} = 150\frac{\mathrm{N}}{\mathrm{mm}^3}$.

The fine scale domain is based on the model indicator (6.23). As threshold value $\|\nabla\boldsymbol{\sigma}\|_{\mathrm{tol}} = 150\frac{\mathrm{N}}{\mathrm{mm}^3}$ is applied. On the fine scale, both the main crack and the elliptic fine scale cracks are explicitely included. The size of the fine scale cracks and the implemented possible XFEM enrichment schemes, lead to a minimal element edge length of 3.5 μm, which is achieved if every coarse scale element included in the fine scale domain is divided into $3 \times 3 \times 3$ elements. Using this discretization the fine scale simulation has 105,000 elements. A single scale analysis with a uniform mesh of a comparable resolution including the fine scale cracks requires 61 million elements. Thus, the adaptive discretization procedure on the coarse scale combined with the multiscale approach leads to a factor of 380 between the applied numbers of elements.

The fine scale cracks lead to a crack shielding effect at the crack front. For visualization effects, the zz-stress distribution is plotted at some slices cut through the fine scale domain. The slice positions are given in figure 7.12. The coordinates begining at the backmost slice are $y_1 = 0.33$ mm, $y_2 = 0.22$ mm, $y_3 = 0.11$ mm, $y_4 = 0.0$ mm.

The discretization lines in the slides (figure 7.13) assume triangles or tetrahedra for the elements. However, hexahedrals are used for the discretization and the lines are only post-processing artifacts. Nevertheless, the mesh size is indicated. The crack shielding effect

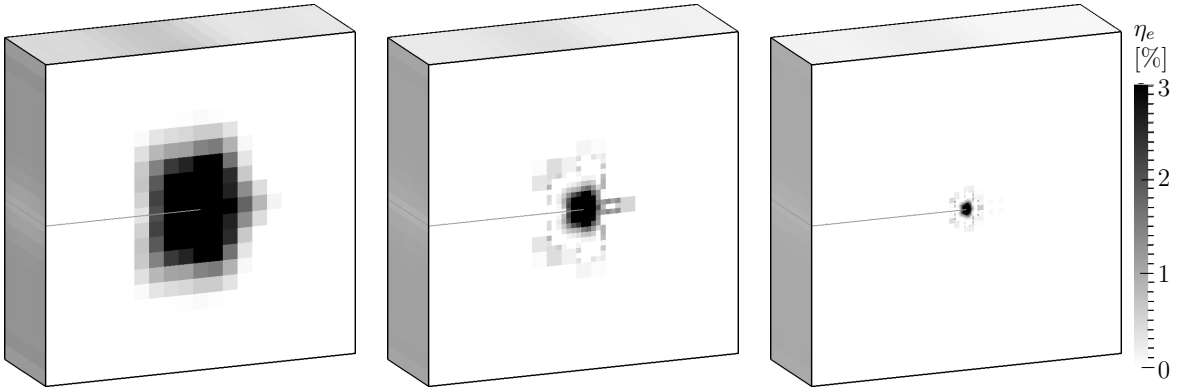

Figure 7.11: Distribution of the local error indicator η_e in the coarse scale. *left* without refinements, *middle* after one refinement with $\eta_{tol} = 3\%$, *right* after two refinements with $\eta_{tol} = 3\%$.

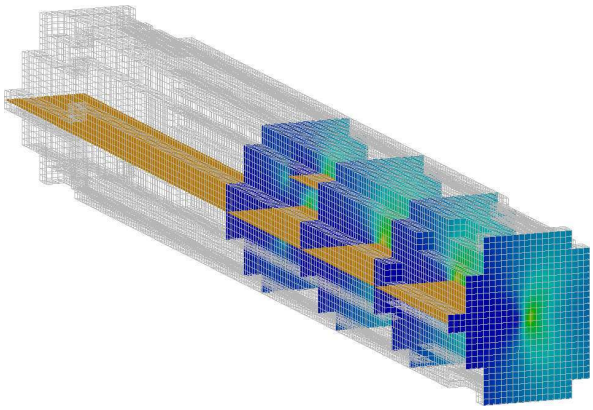

Figure 7.12: Positions of slices in the fine scale domain. The coordinates according to the coordinate system shown in figure 7.9 are begining at the backmost slide
$y_1 = 0.33$ mm, $y_2 = 0.22$ mm, $y_3 = 0.11$ mm, $y_4 = 0.0$ mm.

of the fine scale cracks to the main crack front is shown in figure 7.13 for $y_1 = 0.33$ mm. To resolve more precise results, a discretization indicator based adaptive mesh refinement is applied to the fine scale domain. The threshold value is chosen to be the same as for the coarse scale refinement, i.e. $\eta_{tol} = 3\%$. Every element, which has to be refined, is divided into $3 \times 3 \times 3$ elements. This leads to a resulting element edge length of 1.2 μm. The improvements according to the zz stress field are displayed in figure 7.13. The reduction of the local discretization error in the fine scale domain is shown in figure 7.14.

To summarize, the resulting element edge length, the number of elements for the simulation and the number of elements, if a single scale simulation would have been used for the according steps, are shown in table 7.2.

simulation step	number of elements (single scale, uniform refinement)	number of elements used in the applied simulation	minimal element edge length in the simulation
coarse scale 0 refinements	3,087	3,087	0.1 mm
coarse scale 2 refinements	$2.2 \cdot 10^6$	54,000	10.6 μm
fine scale 0 refinements	$61 \cdot 10^6$	54,000+105,000	3.5 μm
fine scale 1 refinement	$1{,}650 \cdot 10^6$	54,000+415,000	1.2 μm

Table 7.2: Comparison of the number of elements for a comparable single scale simulation to the applied simulation steps. The minimal element edge length is given.

The 3D simulation with adaptive refinements on both scales and with the identification of the fine scale domain based on a model indicator leads to a factor of 1,700 between the entire domain edge length and the minimal edge length of an element in the refined fine scale simulation. The factor between the number of elements for a uniform single scale simulation and the number of elements for the presented simulation steps is 3,500. As the number of elements are approximately proportional to computational costs, the space for computer memory as well as the computational time can be drastically reduced with the presented techniques. These differences are not given for the current simulation because the uniform single scale analysis with approximately 1,650 million elements is only computable on powerful computer cluster systems. A full parallelization of the program code enables the solution for more unknowns. However, it is not reasonble to use a fully fine resolved mesh as in some areas the fine scale effects do not significantly change the overall solution (98). The presented results with the applied simulation substeps can be computed on modern standard computer achitectures within a few hours, whereby an internal memory of 16 GB is sufficient.

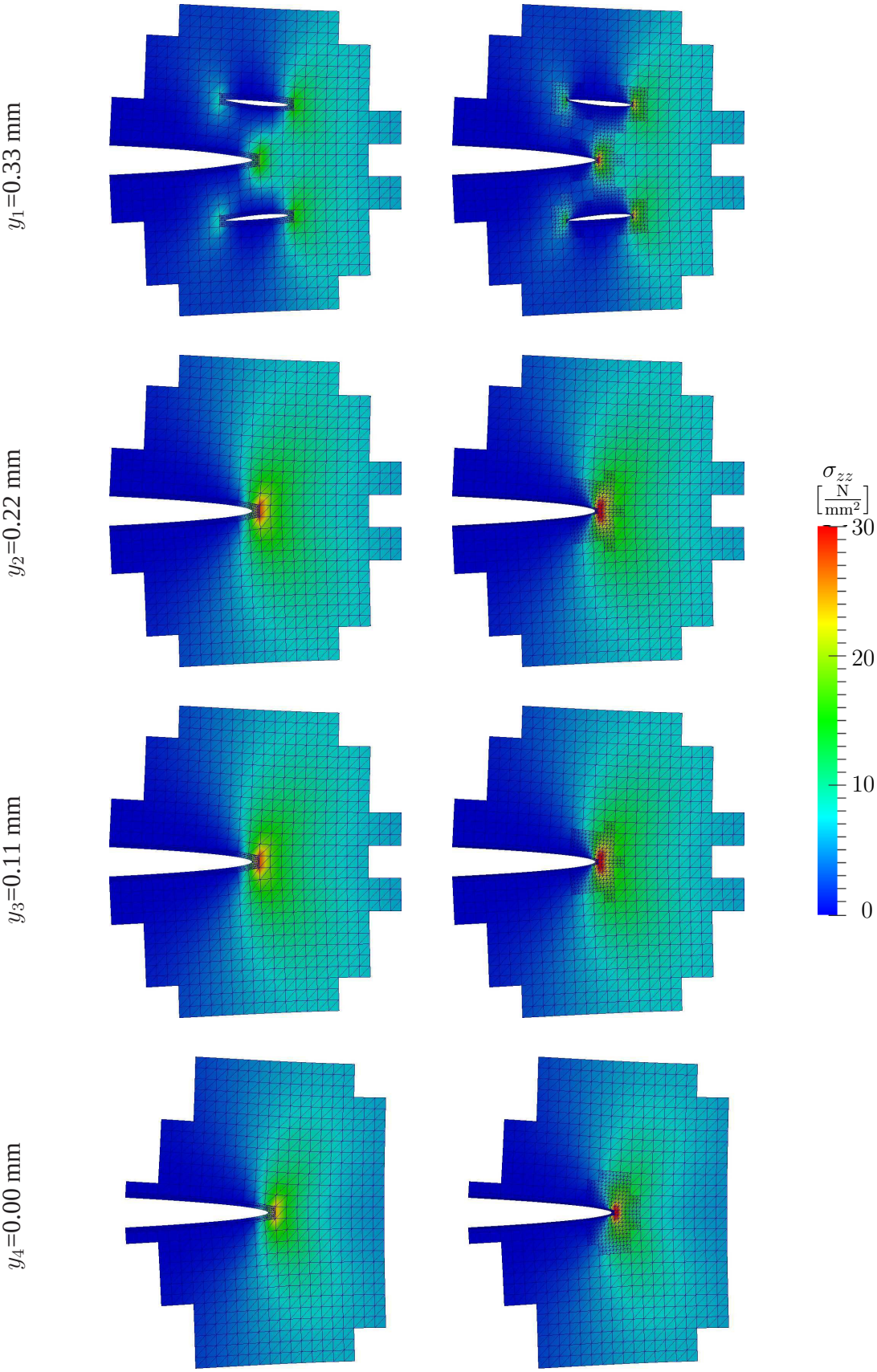

Figure 7.13: zz stress distribution at the slice positions. *left* unrefined fine scale, *right* fine scale with one refinement with $\eta_{tol} = 3\%$.

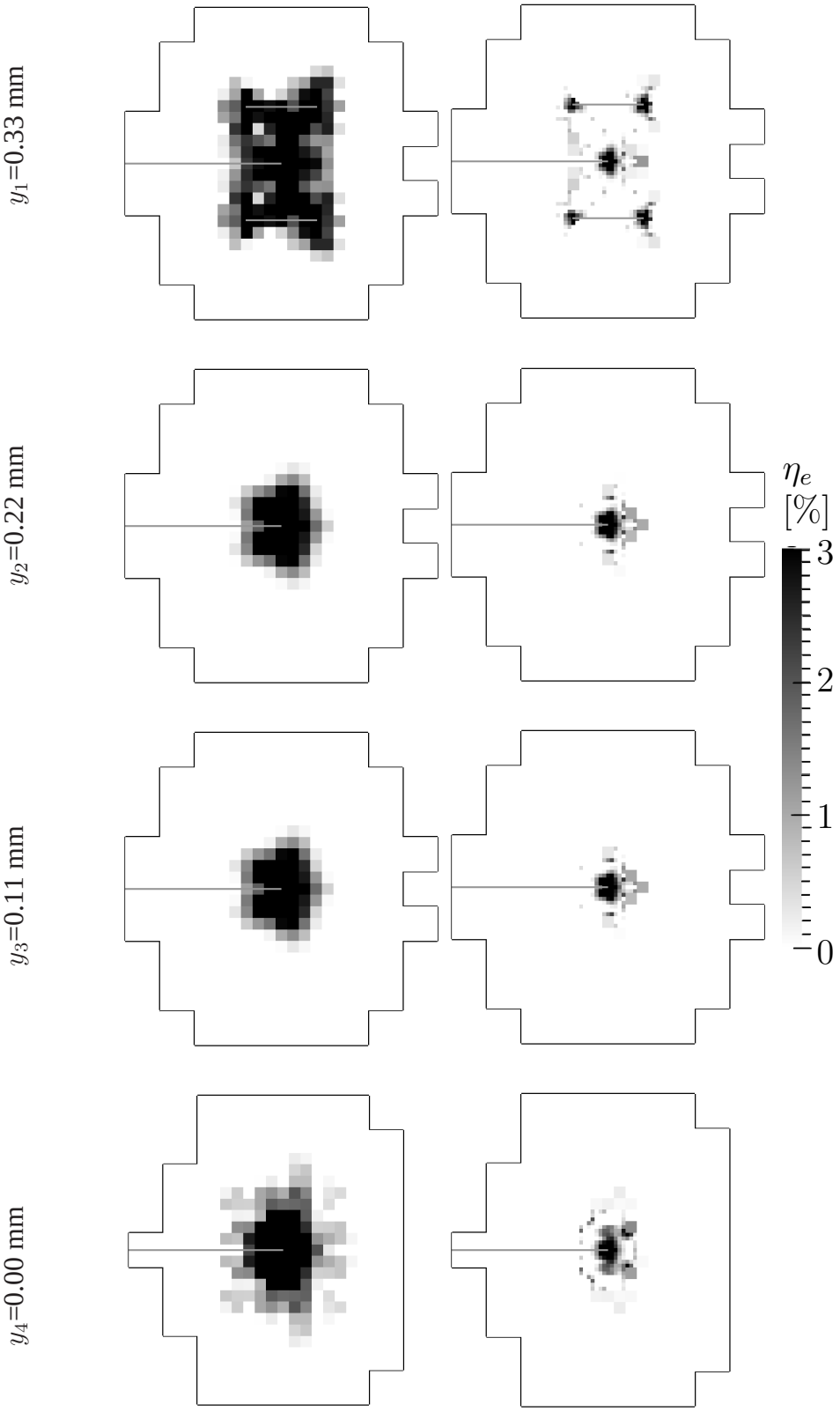

Figure 7.14: Distribution of the local discretization error indicator η_e on the unrefined *(left)* and on the refined *(right)* fine scale domain.

7.4 Application to Experiments

As a final example the application of the presented techniques to an experimentally determined crack configuration, cf. section 3.2.2, is presented. The test specimen has a length of 25 mm and a cross section area of $1.5\,\mathrm{mm} \times 1.5\,\mathrm{mm}$. The domain size is shown in figure 7.15. The mesh size which is needed to represent this crack with level sets is relatively small compared to the length of the overall domain. Regarding the crack geometry, the necessary minimal element edge length is 0.017 mm. A uniform discretization with this mesh resolution leads to approximately 11.6 million elements. This number of elements leads to high computational costs regarding time and memory storage. Thus, an a priori mesh refinement of an initially coarser mesh around the crack has to be applied. The initial mesh is $10 \times 159 \times 10$ elements. Thereafter, the mesh is refined in two steps, whereby every element which has to be refined is divided into $3 \times 3 \times 3$ elements. Not only the domain around the crack, but also the domains where boundary conditions need to be applied are refined in the first step. Therefore, every element with one node in the domains 1-4 in table 7.3 is refined. In a second refinement only elements around the crack path are refined, these are elements with one node in domain 5, which is given in table 7.3.

	$x_{\min}$ [mm]	$x_{\max}$ [mm]	$y_{\min}$ [mm]	$y_{\max}$ [mm]	$z_{\min}$ [mm]	$z_{\max}$ [mm]
domain 1 *(red)*	0.0	1.5	-0.28	0.12	-1.5	0.0
domain 2 *(red)*	1.4	1.5	0.5	0.3	-1.5	0.0
domain 3 *(red)*	0.0	0.1	-7.4	-7.2	-1.5	0.0
domain 4 *(red)*	0.0	0.1	6.9	7.15	-1.5	0.0
domain 5 *(yellow)*	0.0	1.3	-0.2	0.05	-1.5	0.0

Table 7.3: Domains which have to be refined to represent the crack geometry of the experimental result. The colored representation is given in figure 7.15.

The resulting domains with different element sizes are displayed in figure 7.15. The elements in the domain without refinement have an element edge length of approximately 0.15 mm, those in the domain with one refinement have an element edge length of approximately 0.05 mm and the element edges in the domain with two refinements have the necessary element edge length to represent the main crack geometry of approximately 0.017 mm.

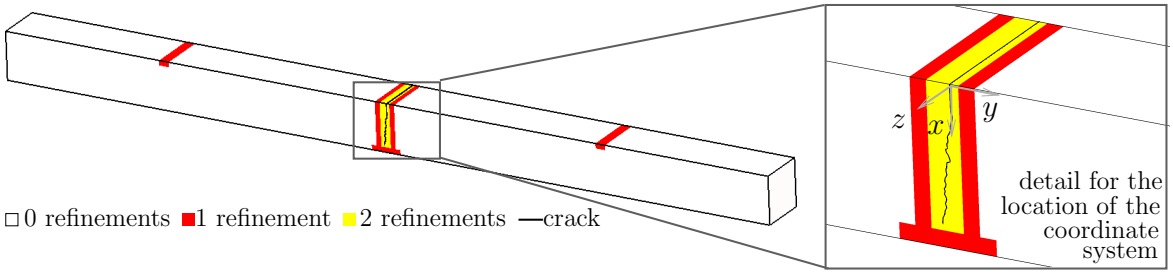

Figure 7.15: Setup for the numerical simulation with the refined domains marked in different colors.

In the three-point-bending test, the crack usually propagates into the direction of the bearing roll on the opposite side of the initial crack. In the experiment it could not be guaranteed that the bearing roll is positioned directly at the opposite side. As the resulting crack path has the crack front at the position of -0.12 mm in y direction correlating to the applied coordinate system shown in figure 7.15, the boundary conditions for the bearing rolls are shifted by -0.12 mm. Hence, fixed boundary conditions in x direction are applied in the total depth (z direction) in the regions with $x = 0$ mm and $-7.4\,\mathrm{mm} < \mathrm{y} < -7.2\,\mathrm{mm}$, $6.9\,\mathrm{mm} < \mathrm{y} < 7.15\,\mathrm{mm}$ respectively. This means that four rows of nodes are fixed for each of the bearing rolls at the top. At the bottom at the position of the third bearing roll, a distributed pressure is applied at $x = 1.5$ mm and $-0.4979\,\mathrm{mm} \leq \mathrm{y} \leq 0.2883\,\mathrm{mm}$, displayed in figure 7.16. The total force of the applied pressure on the defined domain at the bottom is 0.13 N. The material parameters are given with a YOUNG's modulus $E = 200\,\mathrm{GPa}$ and a POISSON's ratio $\nu = 0.3$ as measured for the magnesium-stabilized zirconia $Z - 507$, cf. section 3.2.2.

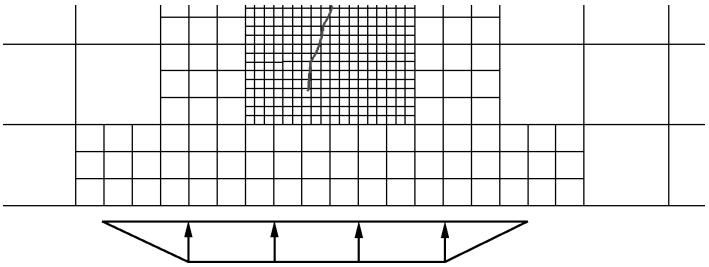

Figure 7.16: Pressure distribution at the position of the lower bearing roll.

Together with the corrected XFEM and an enforcement of the hanging node constraints with LAGRANGE multipliers, the a priori refined mesh leads to 625,695 degrees of freedom. The discretization is analyzed by applying the relative discretization error indicator given in equation (6.20). The results for the local error distribution are shown in figure 7.17. The local error is nearly equally distributed in the entire domain. Solely in the elements in the domains with applied boundary conditions, the relative local error is larger than the tolerance of $\eta_{tol} = 3\%$. However, the boundary constraints in the applied way lead to stress singularities even for finer meshes. Thus, the coarse scale domain is not refined anymore.

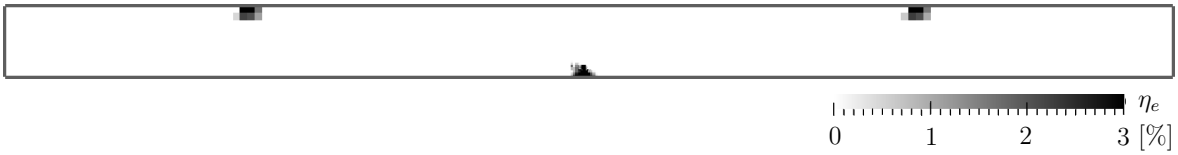

Figure 7.17: Distribution of the local discretization error indicator on the a priori refined coarse scale.

To include small cracks in the simulation, the multiscale projection method (section 5.2) is applied to the simulation. The fine scale cracks are chosen to be circular and arbitrarily distributed and located in the fine scale domain. Here only one possible distribution is assumed as no measurement data are available. To ensure a real representation of the crack distribution a statistically MONTE CARLO analysis should be done. This is excluded as here the force of the presented methodology is shown in general. As the fine scale cracks are

also represented with level sets, the minimal size of a fine scale crack depends on the mesh resolution of the fine scale. Furthermore, the number of fine scale elements is influenced by the size of the fine scale domain. The fine scale domain is chosen depending on the model indicator (section 6.4). The threshold values $\|\nabla\boldsymbol{\sigma}\|_{\mathrm{tol}} = 240\frac{\mathrm{N}}{\mathrm{mm}^3}$ is choosen to define the fine scale domain, which leads to 2,896 coarse scale elements included in the fine scale domain. The resulting number of elements depending on the mesh resolution of the fine scale as well as the minimal fine scale crack diameter, which depends on the allowed XFEM enrichment scheme and thus on the element size, are given in table 7.4.

fine scale discretization in one coarse scale element	minimal diameter of fine scale crack [μm]	number of fine scale elements
$5 \times 5 \times 5 = 125$	29.40	360,000
$7 \times 7 \times 7 = 343$	20.00	990,000
$9 \times 9 \times 9 = 729$	16.33	$2.1{\cdot}10^6$
$11 \times 11 \times 11 = 1,331$	13.36	$3.9{\cdot}10^6$

Table 7.4: Minimal crack diameter for circular cracks on the fine scale dependent on the fine scale mesh resolution. Additionally, the resulting number of elements on the fine scale is given for a threshold value $\|\nabla\boldsymbol{\sigma}\|_{\mathrm{tol}} = 240\frac{\mathrm{N}}{\mathrm{mm}^3}$.

For a fine scale mesh resulting from a refinement of one coarse scale element with 125 or 343 fine scale elements, the minimal diameter of a fine scale crack (29.4 μm and 20.0 μm) is larger than the coarse scale element edge length of 0.17 μm. Every element with the L_2 norm of the stress gradient of the recovered enhanced stress field larger than $\|\nabla\boldsymbol{\sigma}\|_{\mathrm{tol1}} = 240\frac{\mathrm{N}}{\mathrm{mm}^3}$ (cf. equation (6.24)) is included in the fine scale domain.
For the simulation a fine scale mesh of $5\times5\times5$ elements in each related coarse scale element is applied. As a measurement of the fine scale cracks around the main crack front was not possible in the experiments, 20 circular arbitrarily oriented and distributed fine scale cracks are applied to the fine scale domain. A penetration of fine scale cracks or a penetration of a fine scale crack into the main crack is excluded. The fine scale cracks have a diameter of 29.4 μm. The fine scale domain as well as the fine scale cracks around the main crack front are sketched in figure 7.18.
The deformed state of the overall domain and the fine scale zone are visualized in figure 7.19. As the fine scale domain is rather small, a zoom to the area around the main crack is figured out.
As the influence of the fine scale cracks on the main crack and the fine scale crack openings are not visible in figure 7.19, the stress distribution in the fine scale domain is shown on different slices through the domain. The slice positions are given as shown in figure 7.20.
The stress distribution in y direction is plotted in figure 7.21 in the right column. Especially in the slice with z=-0.35 mm, the crack shielding effect of the fine scale crack to the stress concentration at the main crack front can be seen. The local error distribution for the fine scale domain is plotted for the four slices in figure 7.21 in the left column.
The crack length of the fine scale cracks shown in figure 7.18 is about 29 μm. However, a finer mesh resolution of the fine scale domain with an applied adaptive mesh refinement

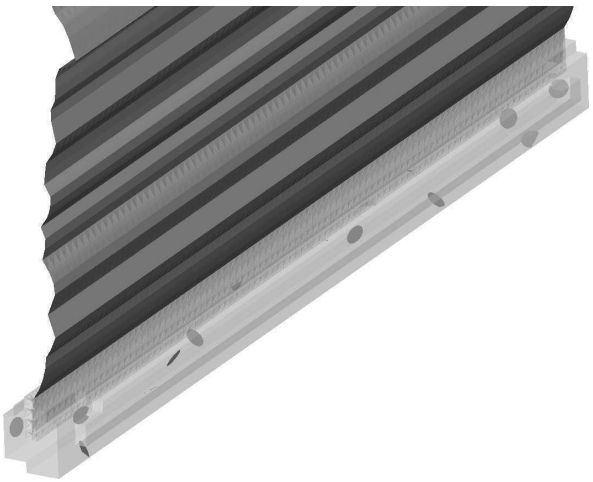

Figure 7.18: Fine scale domain and fine scale cracks around the main crack front for a fine scale domain determined by a model indicator of $\|\nabla\boldsymbol{\sigma}\|_{\mathrm{tol1}} = 240\frac{\mathrm{N}}{\mathrm{mm}^3}$ applied to the coarse scale.

Figure 7.19: Deformed domain after a multiscale simulation. The light gray part is the fine scale domain.

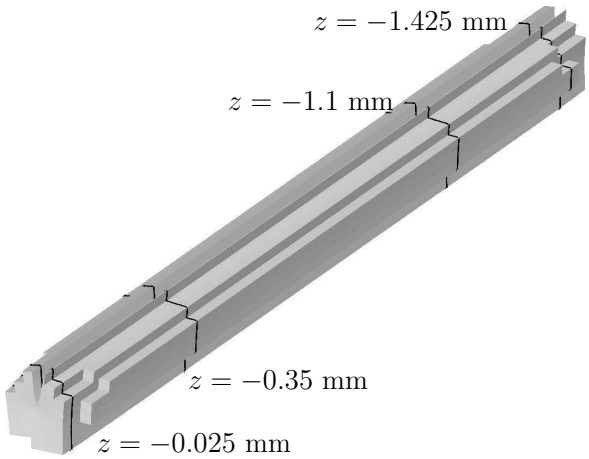

Figure 7.20: Positions of slices to analyze the effect of the fine scale cracks on the coarse scale.

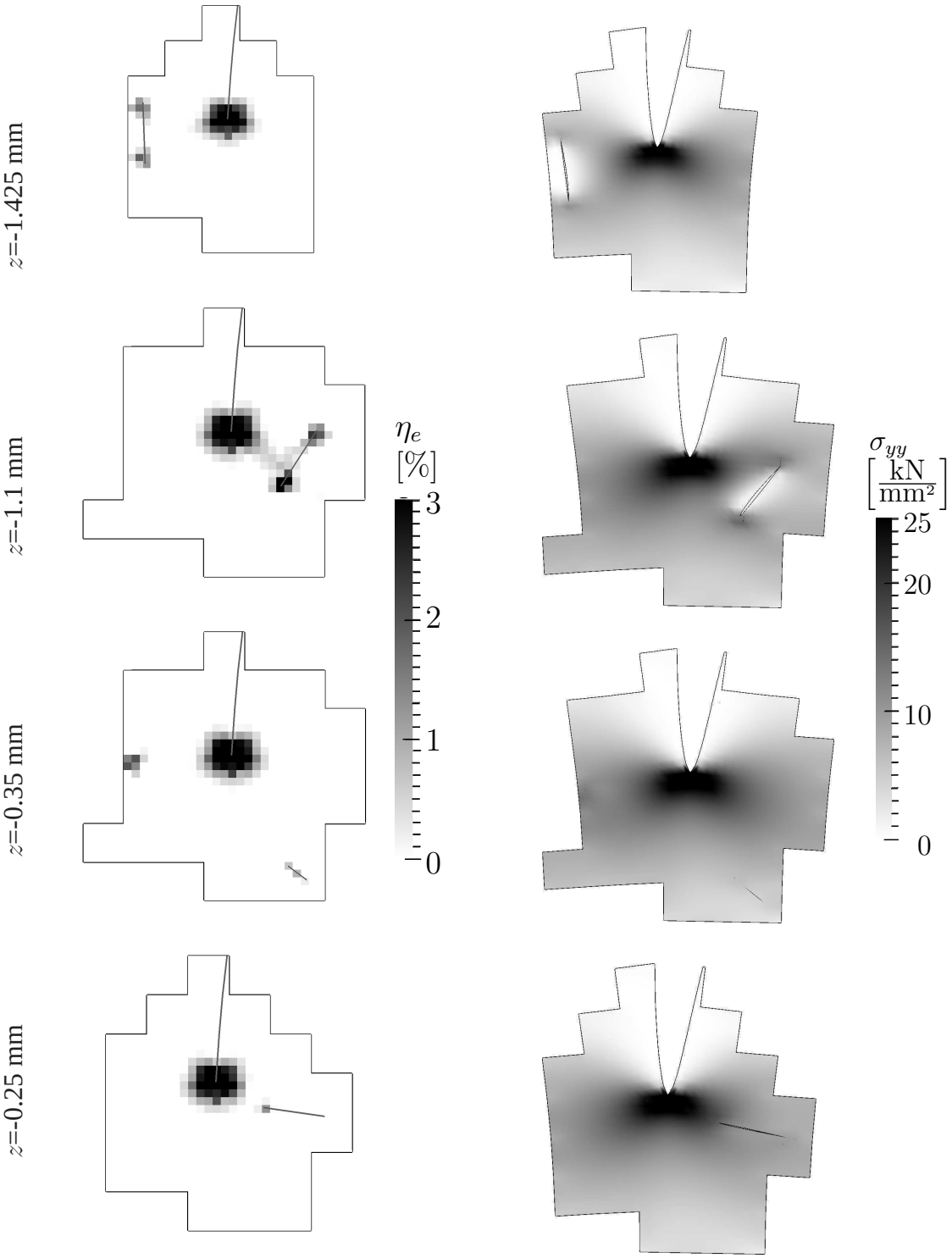

Figure 7.21: Local error distribution in the fine scale, which is the basis for mesh refinement on the fine scale domain *(left)*. Stress distribution around the main crack front influenced by fine scale cracks without refinements *(right)*.

is not possible for the given experiment as the computational costs are limited especially regarding memory storage. Thus, the measured micro crack length of approximately 10 μm (section 3.2.2) could not be modeled in the presented simulation.
Nevertheless, cracks with a length of 29 μm are included in the simulation. The main crack and the fine scale cracks can be included in the same simulation to obtain accurate results especially for the stress distribution around the crack fronts.
On the whole, different length scales of 25 mm to 29 μm can be simulated within one simulation without exceeding the computer capacities of modern standard computer architectures. Thus, a priori mesh refinement, model indication and the application of a multiscale technique as well as a posteriori adaptive mesh refinement lead to an efficient simulation with accurate results. The first difference in scale between the entire domain (25 mm) and the main crack length (1.3 mm) is realized with a priori refinement of an initial coarse mesh. Nevertheless, the local error distribution has to be controlled after the a priori mesh refinement to ensure that all domains which include high error values are refined appropriately. For the implementation of the second difference in length scales between the main crack and micro cracks (29 μm) the multiscale projection method (section 5.2) is applied in combination with a model indicator (section 6.4) for the detection of the fine scale domain. However, the drawback of the adaptive mesh refinement on the fine scale especially for 3D is the large number of degrees of freedom in the refined fine scale simulation. A further improvement to the presented strategy is an a priori refinement of the fine scale domain, especially, if fine scale cracks are not defined arbitrarily, but represent measured micro cracks.

Chapter 8

Conclusions

A combination of error indication techniques to allow for cracks of different scales within one simulation is presented. Different steps are necessary to include cracks which are orders of magnitude smaller than main cracks. The numerical method for the representation of the cracks in the simulation is the XFEM (18).
The first simulation step is an adaptive mesh refinement of the overall (coarse scale) domain including only main cracks. The mesh refinement criterion is based on a discretization error indicator. The error indication technique can be based on different error estimators. Goal oriented error estimators lead to a refinement which improves the quantities of interest applied to the estimator. A recovery based error estimator leads to a first estimation of the entire discretization quality. Here, the adaptivity is based on a stress recovery process and a corresponding discretization error indicator. The error indicator based on stresses, facilitates the application of the error indicator to various materials, especially to the implementation of plasticity. Consequently, an enhanced stress field has to be computed and is compared to the stress field resulting from the XFEM simulation. Therefore, in a postprocessing step the difference between the smoothed enhanced stress field and the stress field according to the XFEM solution is minimized with a least squares technique. The stress recovery process has, as the XFEM makes use of additional degrees of freedom at nodes close to the crack, to be evaluated on the entire domain. For a local patch-wise recovery process, the patch of elements can include enriched nodes, while the crack, which enforces the enrichments is not inside the patch. The evaluation of the stress components concerning to the enrichments then becomes complicated. However, the stress singularities around the crack front have to be present in the recovered stress field. Thus, additional degrees of freedom belonging to the analytical solutions of mode I, mode II and mode III crack opening are introduced at the nodes of the finite element mesh around the crack front. These analytical solutions differ for each stress component. The stress recovering process is enforced separately for each stress component. With the recovered stresses a discretization error indicator can be achieved in the L_2 norm of stresses which takes all stress components into account. This type of discretization error indicator automatically leads to a mesh refinement not only around crack fronts, but also in regions around re-entrant corners or close to prescribed boundary conditions. After some refinement steps, the error controlled mesh refinement leads to a mostly uniform distribution of the discretization error in the entire domain.
For the resolution of smaller cracks in larger structures difficulties may already arise in this

first simulation step as the XFEM is combined with the level set method to evaluate the description of the cracks in the simulation. Using the level set method, the precision of the crack surface and the crack front geometry are influenced due to the discretization. An improvement to the applied level set method is the use of higher order level sets. Thus, features of the crack surface can be represented in more detail. However, the representation of the crack surface depends on the element sizes. An alternative is an explicit description of cracks using non-uniform rational B-splines, which enables a precise representation of the crack surface. However, since for enrichment functions in the vicinity of the crack front it is necessary to calculate the distance of the quadrature points to the crack front as well as their angle to the tangential plane to the crack surface at the crack front, an explicit crack description is computationally more complex compared to a level set description. In contrast, the level set method simplifies the evaluation of the distance to the crack front, as a direct computation based on the level set values is possible. A further advantage is the necessary storage of the level sets only for the different nodes as they can be easily interpolated for the quadrature points using the FE shape functions. However, to resolve a crack surface in detail, a minimal discretization is necessary. This minimal discretization depends primarily on the implemented enrichment scheme which currently does not allow for more than one crack associated to a node. Additionally, a whole crack inside of one element is excluded. Non-planar cracks can therefore only be resolved in appropriately fine meshes. However, a use of the minimal discretization required for the crack representation should be avoided for the entire coarse scale domain to achieve an efficient simulation. Two possibilities to avoid a fine mesh in the entire domain exist. The method chosen in this thesis is the use of an a priori mesh refinement based on empirical knowledge. The regions in which boundary conditions have to be applied as well as the area where the crack is located are refined before the level sets are introduced to the FE mesh. A second method is to use at the beginning an overall mesh with the minimal mesh size given due to the crack surface. Thereafter, a coarsening in regions with rather small discretization error indicated has to be applied, to reduce the computation time and the internal memory usage during the simulation. A difficulty of the coarsening process is the definition of elements which belong to a new coarser element. Another drawback is the high computational costs required for the first simulation step. Thus, the method applied for the presented simulations has more advantages. However, as the a priori refinements are based on heuristic experiences, the resulting coarse scale mesh has to be analyzed with the discretization error indicator. Based on the results further refinements have to be applied if necessary.

In a second simulation step the multiscale projection method (98) is applied to include cracks that are some orders of magnitude smaller than a main crack in the simulation. The multiscale projection method enables simulations of different scales with a representation of localization effects which cannot be represented with the application of classical homogenization techniques. In the multiscale projection method a, fine scale domain around the main crack front is introduced, whereby the fine scale domain explicitly includes the smaller cracks. The first idea to define the fine scale domain is a tubular domain around the main crack front based on heuristic experiences. A more physical approach is the fine scale domain based on a model indicator. This indicator makes use of the enhanced smoothed stress field already needed for the adaptive mesh refinement on the coarse scale domain. In every element with

only non-enriched nodes, the stress gradient of all stress components is evaluated at the element center. However, in all elements with some or all nodes enriched, the stress gradient is computed at every integration point and the mean value of these stress gradients is taken to decide whether the element has to be included in the fine scale or not. Especially for barely cut coarse scale elements, this procedure leads to single coarse scale elements indicated for the fine scale domain. In those cases, the surrounding elements are not included in the fine scale domain, which indicates that the averaging of the stress gradients for the XFEM elements is probably not the best choice. Instead, improvements to the evaluation of the stress gradient or the possibilities for different criteria to define the fine scale domain should be taken into account in future works. Nevertheless, the detection of the fine scale domain based on the presented model indicator leads to a consideration of fine scale features not only in regions around the crack front, but also in regions around re-entrant corners or close to prescribed boundary conditions which may induce cracks. Therefore, especially if crack propagation or crack nucleation has to be simulated, the model indicator has to be applied to define the fine scale domain.

An important issue regarding the applied multiscale strategy is the crack geometry of coarse scale cracks in the fine scale simulation. As the crack geometry in the presented approach is evaluated using the level set method, the coarse scale level sets have to be projected onto the fine scale mesh. Thus, kinks in the crack surface resulting from the discretization on the coarse scale are not allowed to be smoothed. Especially for non-planar crack surfaces, the crack geometry in general cannot be represented exactly with level sets. Therefore, the coarse scale mesh has to be fine enough to include the main features of the coarse scale crack geometry.

The third simulation step to improve the results is an adaptive mesh refinement on the fine scale. With each refinement step, the small cracks only existing on the fine scale are described more precisely with a recalculation of the level set values. Again, the main cracks which exist on the coarse scale as well, need to be represented with exactly the same crack geometry on the fine scale. Thus, only the fine scale crack geometry is allowed to be modified during mesh refinement of the fine scale. Refinements on the fine scale are necessary to improve the accuracy of the stress distribution around the crack fronts. Based on the presented discretization error indicator, one step of mesh refinement of the fines scale already improves the solution.

Applying the discretization error indication technique, the model indication and the multiscale projection method to the XFEM, cracks of significantly different length scales can be considered in the same simulation. The application of error indication techniques to the XFEM is still a topic of current research, although, as presented, different methods within this field already exist.

Nevertheless, a couple of further simulation steps should be taken into account. Crack propagation is one of the most important topics, especially to validate numerical simulations with experiments. As the coupling of the multiscale projection method to crack propagation was proposed in (80), in a next step, the crack propagation should be included in the discretization and model adaptive simulation. Using discretization adaptivity, more accurate stress distribution fields lead to more precise crack paths. In the context of crack propagation other error indication technique should be considered as well. Goal oriented error estimation (65; 118)

leads to an improvement of quantities of interest as e.g. stress intensity factors which can be used as a criterion for crack propagation.
Furthermore, even if the multiscale projection methods allows for different orders of magnitude of cracks, the size of the cracks is limited due to computer capacities. Especially in 3D, the fine scale simulation with the mesh size to represented fine scale cracks can lead to large systems of equations with a minimum of 50 million of degrees of freedom. In those cases, a simulation is only reasonable on powerful computer cluster systems. However, if the fine scale domain is refined a priori, the cracks can be represented while keeping low computational costs. Thus, especially for experiments with measured fine scale cracks an a priori refined fine scale domain should be applied within the multiscale projection method. Then fine scale cracks of orders of magnitude smaller than the dimension of the structure which is analyzed can be represented.
Further, more general extensions to the XFEM are crack face contact or the inclusion of cracking under thermal loads among others. Crack face contact is important especially if the load case changes during the simulation. If crack closure occurs during a simulation without crack face contact, a non-physical overlapping of the material appears (40; 64). Cracking under thermal loads includes heat conduction also between crack faces and open cracks (46). The XFEM enables a lot of possibilities to model fracture with meshes independent of the crack path. Prospectively, a lot of research has to be done to extend this method to more general examples especially for 3D. Nevertheless, XFEM in combination with multiscale methods and error estimation techniques already allows for accurate solutions for cracks on different scales in the same simulation.

Bibliography

[1] M. Abramowitz and I. A. Stegun. Handbook of mathematical functions with formulas, graphs, and mathematical tables. *National Bureau of Standards Applied Mathematics Series 55, Tenth Printing*, 1972.

[2] R. Ahmad Akbari, P. Kerfriden, T. Rabczuk, and S. Bordas. An adaptive multiscale method for fracture based on concurrent-hierarchical hybrid modelling. 2012.

[3] M. Ainsworth and J. T. Oden. A posteriori error estimation in finite element analysis. *Computer Methods in Applied Mechanics and Engineering*, 142:1–88, 1997.

[4] J. Altenbach and H. Altenbach. *Einführung in die Kontinuumsmechanik*. Teubner, 1994.

[5] T. L. Anderson. *Fracture Mechanics*. Talor & Francis, 3 edition, 2005.

[6] S. N. Atluri, A. S. Kobayashi, and M. Nakagaki. An assumed displacement hybrid finite element model for linear fracture mechanics. *International Journal of Fracture*, 11:257–271, 1975.

[7] I. Babuška and U. Banerjee. Stable generalized finite element method (SGFEM). *Computer Methods in Applied Mechanics and Engineering*, 201:91–111, 2012.

[8] I. Babuška and A. Miller. The post-processing approach in the finite element method-part 1: Calculation of displacements, stresses and other higher derivatives of the displacements. *International Journal for numerical methods in Engineering*, 20:1085–1109, 1984.

[9] I. Babuška and J. M. Melenk. The partition of unity method. *International Journal for Numerical Methods in Engineering*, 40:727–758, 1997.

[10] I. Babuška and W. C. Rheinboldt. A-posteriori error estimates for the finite element method. *International Journal For Numerical Methods in Engineering*, 12:1597–1615, 1978.

[11] I. Babuška and W. C. Rheinboldt. Error estimates for adaptive finite element computations. *Society for Industrial and Applied Mathematics*, 15:736–754, 1978.

[12] Y. Başar and D. Weichert. *Nonlinear continuum mechanics of solids*. Springer, Berlin Heidelberg, 2000.

[13] G. I. Barenblatt. The mathematical theory of equilibrium cracks in brittle fracture. *Advances in applied mechanics*, 7:55–129, 1962.

[14] J. Barlow. Optimal stress locations in finite element models. *International Journal for Numerical Methods in Engineering*, 10:243–251, 1976.

[15] R. S. Barsoum. On the use of isoparametric finite elements in linear fracture mechanics. *International Journal for Numerical Methods in Engineering*, 10:25–37, 1976.

[16] R. S. Barsoum. Triangular quarter-point elements as elastic and perfectly-plastic crack tip elements. *International Journal for numerical Methods in engineering*, 11:85–98, 1977.

[17] E. Béchet, H. Minnebo, N. Moës, and B. Burgardt. Improved implementation and robustness study of the x-fem for stress analysis around cracks. *International Journal for Numerical Methods in Engineering*, 64:1033–1056, 2005.

[18] T. Belytschko and T. Black. Elastic crack growth in finite elements with minimal remeshing. *International Journal for Numerical Methods in Engineering*, 45:601–620, 1999.

[19] T. Belytschko, R. Gracie, and G. Ventura. A review of extended/generalized finite element methods for material modeling. *Modelling and Simulation in Materials Science and Engineering*, 17:043001, 2009.

[20] T. Belytschko, W. Liu, and B. Moran. *Nonlinear finite elements for continua and structures*. Wiley, 2003.

[21] T. Belytschko, S. Loehnert, and J.-H. Song. Multiscale aggregating discontinuities: a method for circumventing loss of material stability. *International Journal for Numerical Methods in Engineering*, 73:869–894, 2008.

[22] T. Belytschko, Y. Y. Lu, and L. Gu. Element-free galerkin methods. *International Journal for Numerical Methods in Engineering*, 37:229–256, 1994.

[23] T. Belytschko, N. Moës, S. Usui, and C. Parimi. Arbitrary discontinuities in finite elements. *International Journal for Numerical Methods in Engineering*, 50:993–1013, 2001.

[24] H. ben Dhia and G. Rateau. The arlequin method as a flexible engineering design tool. *International Journal for Numerical Methods in Engineering*, 62:1442–1462, 2005.

[25] D. J. Benson, Y. Bazilevs, E. De Luycker, M.-C. Hsu, M. Scott, T. J. R. Hughes, and T. Belytschko. A generalized finite element formulation for arbitrary basis functions: from isogeometric analysis to xfem. *International Journal for Numerical Methods in Engineering*, 83:765–785, 2010.

[26] S. E. Benzley. Representation of singularities with isoparametric finite elements. *International Journal for Numerical Methods in Engineering*, 8:537–545, 1974.

[27] J. Betten. *Kontinuumsmechanik*. Springer, Berlin Heidelberg, 2 edition, 2001.

[28] S. Bordas and M. Duflot. Derivative recovery and a posteriori error estimate for extended finite elements. *Computer Methods in Applied Mechanics and Engineering*, 196:3381–3399, 2007.

[29] S. Bordas, M. Duflot, and P. Le. A simple error estimator for extended finite elements. *Communications in Numerical Methods in Engineering*, 24(11):961–971, 2008.

[30] E. Budyn, G. Zi, N. Moës, and T. Belytschko. A method for multiple crack growth in brittle materials without remeshing. *International Journal for Numerical Methods in Engineering*, 61:1741–1770, 2004.

[31] A. Byfut and A. Schröder. *hp*-adaptive extended finite element method. *International Journal for Numerical Methods in Engineering*, 89:1392–1418, 2012.

[32] F. Cajori. Historical note on the newton-raphson method of approximation. *The American Mathematical Monthly*, 18(2):29–32, 1911.

[33] C. Carstensen and S. A. Funken. Averaging technique for fe-a posteriori error control in elasticity. part i: Conforming fem. *Computer Methods in Applied Mechanics and Engineering*, 190:2483–2498, 2001.

[34] J. Chessa, P. Smolinski, and T. Belytschko. The extended finite element method (XFEM) for solidification problems. *International Journal for Numerical Methods in Engineering*, 53:1959–1977, 2002.

[35] J. Chessa, H. Wang, and T. Belytschko. On the construction of blending elements for local partition of unity enriched finite elements. *International Journal for Numerical Methods in Engineering*, 57:1015–1038, 2003.

[36] T. A. Cruse. Numerical evaluation of elastic stress intensity factors by the boundary-integral equation method. Technical report, 1972.

[37] T. A. Cruse. An improved boundary-integral equation method for three dimensional elastic stress analysis. *Computers & Structures*, 4:741–754, 1974.

[38] C. Daux, N. Moës, J. Dolbow, N. Sukumar, and T. Belytschko. Arbitrary branched and intersecting cracks with the extended finite element method. *International Journal for Numerical Methods in Engineering*, 48:1741–1760, 2000.

[39] L. Demkowicz, P. Devloo, and J. T. Oden. On an h-type mesh-refinement strategy based on minimization of interpolation errors. *Computer Methods in Applied Mechanics and Engineering*, 53:67–89, 1985.

[40] J. Dolbow, N. Moës, and T. Belytschko. An extended finite element method for modeling crack growth with frictional contact. *Computer Methods in Applied Mechanics and Engineering*, 190:6825–6846, 2001.

[41] C. A. Duarte and J. T. Oden. *A review of some meshless methods to solve partial differential equations*. Texas Institute for Computational and Applied Mathematics, 1995.

[42] C. A. Duarte and J. T. Oden. Hp clouds-an hp meshless method. *Numerical Methods for Partial Differential Equations*, 12:673–706, 1996.

[43] C. A. Duarte, L. G. Reno, and A. Simone. A high-order generalized fem for through-the-thickness branched cracks. *International Journal for Numerical Methods in Engineering*, 72:325–351, 2007.

[44] M. G. Duffy. Quadrature over a pyramid or cube of integrands with a singularity at a vertex. *SIAM Journal on Numerical Analysis*, 19:1260–1262, 1982.

[45] M. Duflot. A study of the representation of cracks with level sets. *International Journal for Numerical Methods in Engineering*, 70:1261–1302, 2007.

[46] M. Duflot. The extended finite element method in thermoelastic fracture mechanics. *International journal for numerical methods in engineering*, 74:827–847, 2008.

[47] M. Duflot and S. Bordas. A posteriori error estimation for extended finite elements by an extended global recovery. *International Journal for Numerical Methods in Engineering*, 76(8):1123–1138, 2008.

[48] D. S. Dugdale. Yielding of steel sheets containing slits. *Journal of the Mechanics and Physics of Solids*, 8:100–104, 1960.

[49] T. Elguedj, A. Gravouil, and A. Combescure. Appropriate extended funtions for x-fem simulation of plastic fracture mechanics. *Computer Methods in Applied Mechanics and Engineering*, 195:501–515, 2006.

[50] F. Erdogan and G. C. Sih. On the crack extension in plates under plane loading and transverse shear. *Journal of Basic Engineering*, 85(4):519–525, 1963.

[51] V. I. Fabrikant. Close interaction of coplanar circular cracks in an elastic medium. *Acta Mechanica*, 67:39–59, 1987.

[52] F. Feyel and J.-L. Chaboche. FE^2 multiscale approach for modelling the elastovis-coplastic behaviour of long fibre SiC/Ti composite materials. *Computer methods in applied mechanics and engineering*, 183:309–330, 2000.

[53] B. A. Finlayson. *The method of weighted residuals and variational principles: with application in fluid mechanics, heat and mass transfer*, volume 87. Academic Press, New York, 1972.

[54] J. Fish. The s-version of the finite element method. *Computers and Structures*, 43:539–547, 1992.

[55] M. Frémond and B. Nedjar. Damage, gradient of damage and principle of virtual power. *International Journal of Solids and Structures*, 33:1083–1103, 1996.

[56] T.-P. Fries. *A stabilized and coupled meshfree, meshbased method for fluid-structure interaction problems*. Inst. für Angewandte Mechanik, 2005.

[57] T.-P. Fries. A corrected xfem approximation without problems in blending elements. *International Journal for Numerical Methods in Engineering*, 75:503–532, 2008.

[58] T.-P. Fries and T. Belytschko. The intrinsic xfem: a method for arbitrary discontinuities without additional unknowns. *International Journal for Numerical Methods in Engineering*, 68:1358–1385, 2006.

[59] T.-P. Fries and T. Belytschko. The extended/generalized finite elment method: An overview of the method and its applications. *International Journal for Numerical Methods in Engineering*, 84:253–304, 2010.

[60] T.-P. Fries, A. Byfut, A. Alizada, K. W. Cheng, and A. Schröder. Hanging nodes and xfem. *International Journal for Numerical Methods in Engineering*, 86:404–430, 2011.

[61] W. Gander and W. Gautschi. Adaptive quadraturerevisited. *BIT Numerical Mathematics*, 40:84–101, 2000.

[62] J. Garzon, C. A. Duarte, and J. P. Pereira. Extraction of stress intensity factors for the simulation of 3-d crack growth with the generalized finite element method. *Key Engineering Materials*, 560:1–36, 2013.

[63] M. G. D. Geers, V. G. Kouznetsova, and W. A. M. Brekelmans. Multi-scale computational homogenization: Trends and challenges. *Journal of Computational and Applied Mathematics*, 234:2175–2182, 2010.

[64] S. Geniaut, P. Massin, and N. Moës. A stable 3d contact formulation using x-fem. *European Journal of Computational Mechanics/Revue Européenne de Mécanique Numérique*, 16:259–275, 2007.

[65] T. Gerasimov, M. Rüter, and E. Stein. An explicit residual-type error estimator for q_1-quadrilateral extended finite element method in two-dimensional linear elastic fracture mechanics. *International Journal for Numerical Methods in Engineering*, 90:1118–1155, 2012.

[66] E. Giner, F. L. Fuenmayor, L. Baeza, and J. E. Tarancón. Error estimation for the finite element evaluation of g_i and g_{II} in mixed-mode linear elastic fracture mechanics. *Finite Elements in Analysis and Design*, 41:1079–1104, 2005.

[67] O. González-Estrada, S. Natarajan, J. J. Ródenas, H. Nguyen-Xuan, and S. Bordas. Efficient recovery-based error estimation for the smoothed finite element method for smooth and singular linear elasticity. *Computational Mechanics*, 52:37–52, 2013.

[68] R. Gracie and T. Belytschko. Concurrently coupled atomistic and xfem models for dislocations and cracks. *International Journal for Numerical Methods in Engineering*, 78:354–378, 2009.

[69] R. Gracie, J. Oswald, and T. Belytschko. On a new extended finite element method for dislocations: Core enrichment and nonlinear formulation. *Journal of the Mechanics and Pysics*, 56:200–214, 2008.

[70] R. Gracie, H. Wang, and T. Belytschko. Blending in the extended finite element method by discontinuous galerkin and assumed strain methods. *International Journal for Numerical Methods in Engineering*, 74:1645–1669, 2008.

[71] T. Grätsch and K.-J. Bathe. A posteriori error estimation techniques in practical finite element analysis. *Computers & Structures*, 83:235–265, 2005.

[72] A. A. Griffith. The phenomena of rupture and flow in solids. *Philosophical Transactions of the Royal Society of London. Series A, Containing Papers of a Mathematical or Physical Character*, 221:163–198, 1921.

[73] D. Gross and T. Seelig. *Bruchmechanik*. Springer, Berlin Heidelberg, 4 edition, 2007.

[74] P.-A. Guidault, O. Allix, L. Champaney, and C. Cornuault. A multiscale extended finite element method for crack propagation. *Computer Methods in Applied Mechanics and Engineering*, 197:381–399, 2008.

[75] A. K. Gupta. A finite element for transition from a fine to a coarse grid. *International Journal for Numerical Methods in Engineering*, 12:35–45, 1978.

[76] R. J. Hartranft and G. C. Sih. Stress singularity for a crack with an arbitrarily curved front. *Engineering Fracture Mechanics*, 9(3):705–718, 1977.

[77] P. Haupt. *Continuum Mechanics and Theory of Materials*. Springer, Berlin Heidelberg, 2 edition, 2002.

[78] R. D. Henshell and K. G. Shaw. Crack tip finite elements are unnecessary. *International Journal for Numerical Methods in Engineering*, 9:495–507, 1975.

[79] E. Hinton and J. S. Campbell. Local and global smoothing of discontinous finite element functions using a least square method. *International Journal for Numerical Methods in Engineering*, 8:461–480, 1974.

[80] M. Holl, S. Loehnert, and P. Wriggers. An adaptive multiscale method for crack propagation and crack coalescence. *International Journal for Numerical Methods in Engineering*, 93:23–51, 2013.

[81] G. A. Holzapfel. *Nonlinear Solid Mechanics*. Wiley, 2000.

[82] X. Huang and B. L. Karihaloo. Interaction of penny-shaped cracks with a half-plane crack. *International Journal of Solids and Structures*, 30(15):2117 – 2139, 1993.

[83] T. J. R. Hughes. *The finite element method: linear static and dynamic finite element analysis*. Dover Publications, 2000.

[84] M. C. Hussain, S. L. Pu, and J. Underwood. Strain energy release rate for a crack under combined mode i and mode ii. *Fracture Analysis, ASTP STP*, 560:2–28, 1973.

[85] L. W. Hutchinson. Singular behaviour at the end of a tensile crack in a hardening material. *Journal of the Mechanics and Physics of Solids*, 16:13–31, 1968.

[86] G. R. Irwin. Analysis of stresses and strains near the end of a crack traversing a plate. *Transactions of the ASME Journal of Applied Mechanics*, 24:361–364, 1957.

[87] K. Jayaswal and I. R. Grosse. Finite element error estimation for crack tip singular elements. *Finite Elements in Analysis and Design*, 14:17–35, 1993.

[88] M. Kachanov and J.-P. Laures. Three-dimensional problems of strongly interacting arbitrarily located penny-shaped cracks. *International Journal of Fracture*, 41:289–313, 1989.

[89] A. Karma, D. A. Kessler, and H. Levine. Phase-field model of mode III dynamic fracture. *Physical Review Letters*, 87:045501, 2001.

[90] D. Kim, J. Pereira, and C. Duarte. Analysis of three-dimensional fracture mechanics problems: A two-scale approach using coarse-generalized fem meshes. *International Journal for Numerical Methods in Engineering*, 81:335–365, 2010.

[91] V. Kouznetsova, M. G. D. Geers, and W. A. M. Brekelmans. Multi-scale constitutive modelling of heterogeneous materials with a gradient-enhanced computational homogenization scheme. *International Journal for Numerical Methods in Engineering*, 54:1235–1260, 2002.

[92] R. Krause and E. Rank. Multiscale computations with a combination of the *h*- and *p*-versions of the finite-element method. *Computer methods in applied mechanics and engineering*, 192:3959–3983, 2003.

[93] M. Kuna. *Numerische Beanspruchungsanalyse von Rissen*. Vieweg+Teubner, 2 edition, 2010.

[94] P. Laborde, J. Pommier, Y. Renard, and M. Salaün. High-order extended finite element method for cracked domains. *International Journal for Numerical Methods in Engineering*, 64:354–381, 2005.

[95] A. Legay, H. W. Wang, and T. Belytschko. Strong and weak arbitrary discontinuities in spectral finite elements. *International Journal for Numerical Methods in Engineering*, 64:991–1008, 2005.

[96] G. Legrain, N. Moës, and E. Verron. Stress analysis around crack tips in finite strain problems using the extended finite element method. *International Journal for Numerical Methods in Engineering*, 63:290–314, 2005.

[97] S. Loehnert. A stabilization technique for the extended finite element simulation of arbitrary crack geometries in 3d. In M. Jirásek, O. Allix, N. Moës, and L. Oliver, editors, *Computational modeling of fracture and failure of materials and structures, CFRAC2013*, page 139, 2013.

[98] S. Loehnert and T. Belytschko. A multiscale projection method for macro/microcrack simulations. *International Journal for Numerical Methods in Engineering*, 71:1466–1482, 2007.

[99] S. Loehnert and D. Mueller-Hoeppe. Multiscale methods for fracturing solids. In B. Reddy, editor, *IUTAM Symposium on Theoretical, Computational and Modelling Aspects of Inelastic Media*, IUTAM Bookseries, pages 79–87. Springer, 2008.

[100] S. Loehnert, D. S. Mueller-Hoeppe, and P.Wriggers. 3d corrected xfem approach and extension to finite deformation theory. *International Journal for Numerical Methods in Engineering*, 86:431–452, 2011.

[101] S. Loehnert, C. Prange, and P. Wriggers. Error controlled adaptive multiscale xfem simulation of cracks. *International Journal of Fracture*, 178, 2012.

[102] E. Lutz, A. R. Ingraffea, and L. J. Gray. Use of simple solutions for boundary integral methods in elasticity and fracture analysis. *International Journal for Numerical Methods in Engineering*, 35:1737–1751, 1992.

[103] K. M. Mathisen, K. M. Okstad, and T. Kvamsdal. Error estimation and adaptivity in linear static finite element analysis. 1997.

[104] A. Menk and S. Bordas. A robust preconditioning technique for the extended finite element method. *International Journal for Numerical Methods in Engineering*, 85:1609–1632, 2011.

[105] J. Mergheim. A variational multiscale method to model crack propagation at finite strains. *International Journal for Numerical Methods in Engineering*, 80:269–289, 2009.

[106] J. C. Michel, H. Moulinec, and P. Suquet. Effective properties of composite materials with periodic microstructure: a computational approach. *Computer methods in applied mechanics and engineering*, 172:109–143, 1999.

[107] C. Miehe, F. Welschinger, and M. Hofacker. Thermodynamically consistent phase-field models of fracture: Variational principles and multi-field fe implementations. *International Journal for Numerical Methods in Engineering*, 83:1273–1311, 2010.

[108] H. Minnebo. Three-dimensional integration strategies of singular functions introduced by the XFEM in the LEFM. *International Journal for Numerical Methods in Engineering*, 92:1117–1138, 2012.

[109] N. Moës and T. Belytschko. Extended finite element method for cohesive crack growth. *Engineering Fracture Mechanics*, 69:813–833, 2002.

[110] N. Moës, J. Dolbow, and T. Belytschko. A finite element method for crack growth without remeshing. *International Journal for Numerical Methods in Engineering*, 46:131–150, 1999.

[111] N. Moës, A. Gravouil, and T. Belytschko. Non-planar 3d crack growth by the extended finite element and level sets-part i: Mechanical model. *International Journal for Numerical Methods in Engineering*, 53:2549–2568, 2002.

[112] M. Moumnassi, S. Belouettar, E. Béchet, S. Bordas, D. Quoirin, and M. Potier-Ferry. Finite element analysis on implicitly defined domains: An accurate representation based on arbitrary parametric surfaces. *Computer Methods in Applied Mechanics and Engineering*, 200(5):774–796, 2011.

[113] S. E. Mousavi and N. Sukumar. Generalized gaussian quadrature rules for discontinuities and crack singularities in the extended finite element method. *Computer Methods in Applied Mechanics and Engineering*, 199:3237–3249, 2010.

[114] J. T. Oden, S. Prudhomme, A. Romkes, and P. T. Bauman. Multiscale modeling of physical phenomena: Adaptive control of models. *SIAM Journal on Scientific Computing*, 28:2359–2389, 2006.

[115] R. W. Ogden. *Non-linear elastic deformations*. Dover, 1984.

[116] J. Oliver. Continuum modelling of strong discontinuities in solid mechanics using damage models. *Computational Mechanics*, 17:49–61, 1995.

[117] L. Oliver, A. E. Huespe, M. D. G. Pulido, and E. Chaves. From continuum mechanics to fracture mechanics: the strong discontinuity approach. *Engineering Fracture Mechanics*, 69:113–136, 2002.

[118] J. Panetier, P. Ladevèze, and F. Louf. Strict bounds for computed stress intensity factors. *Xomputers and Structures*, 87:1015–1021, 2009.

[119] T. Pannachet, L. J. Sluys, and H. Askes. Error estimation and adaptivity for discontinuous failure. *International Journal for Numerical Methods in Engineering*, 78:528–563, 2009.

[120] K. Park, G. H. Paulino, and J. R. Roesler. A unified potential-based cohesive model of mixed-mode fracture. *Journal of the Mechanics and Physics of Solids*, 57:891–908, 2009.

[121] R. H. J. Peerlings, R. De Borst, W. A. M. Brekelmans, and M. G. D. Geers. Gradient-enhanced damage modelling of concrete fracture. *Mechanics of Cohesive-frictional Materials*, 3:323–342, 1998.

[122] C. Prange, S. Loehnert, and P. Wriggers. Error estimation for crack simulations using the xfem. *International Journal for Numerical Methods in Engineering*, 91:1459–1474, 2012.

[123] R. Rannacher and F.-T. Suttmeier. *Error estimation and adaptive mesh design for FE models in elasto-plasticity theory*, chapter 2, pages 5–52. Wiley, 2003.

[124] J. Rannou, A. Gravouil, and A. Combescure. A multi-grid extended finite element method for elastic crack growth simulation. *European Journal of Computational Mechanics/Revue Européenne de Mécanique Numérique*, 16:161–182, 2007.

[125] J. R. Rice. A path independent integral and the approximate analysis of strain concentrations by notches and cracks. *Transaction of the ASME Journal of Applied Mechanics*, 35:379–386, 1968.

[126] J. R. Rice. Elastic fracture mechanics concepts for interfacial cracks. *Trans. ASME Journal of Applied Mechanics*, 55:98–103, 1988.

[127] J. R. Rice and G. F. Rosengren. Plane strain deformation near a crack tip in a power-law hardening material. *Journal of the Mechanics and Physics of Solids*, 16:1–12, 1968.

[128] J. J. Ródenas, O. A. González-Estrada, F. J. Fuenmayor, and F. Chinesta. Enhanced error estimator based on a nearly equilibrated moving least squares recovery technique for fem and xfem. *Computational Mechanics*, pages 1–24, 2012.

[129] J. J. Ródenas, O. A. González-Estrada, J. E. Tarancón, and F. J. Fuenmayor. A recovery-type error estimator for the extended finite element method based on singular + smooth stress field splitting. *International Journal for Numerical Methods in Engineering*, 76:545–571, 2008.

[130] L. R. F. Rose. Microcrack interaction with a main crack. *International Journal of Fracture*, 31:233–242, 1986.

[131] A. A. Rubinstein. Macrocrack-microdefect interaction. *Journal of Applied Mechanics*, 53:505–510, 1986.

[132] M. Rüter. *Error controlled adaptive finite element methods in large strain hyperelasticity and fracture mechanics*. Inst. für Baumechanik und Numerische Mechanik Hannover, 2003.

[133] J. C. Simo and T. J. R. Hughes. *Computational Inelasticity*. Springer-Verlag, New York, 1998.

[134] J. C. Simo, J. Oliver, and F. Armero. An analysis of strong discontinuities induced by strain-softening in rate-independent inelastic solids. *Computational Mechanics*, 12:277–296, 1993.

[135] A. Simone, C. A. Duarte, and E. V. der Giessen. A generalized finite element method for polycrystals with discontinuous grain boundaries. *International Journal for Numerical Methods in Engineering*, 67:1122–1145, 2006.

[136] I. N. Sneddon. The distribution of stress in the neighbourhood of a crack in an elastic solid. *Proceedings of the Royal Society (London) A*, 187:229–260, 1946.

[137] F. L. Stazi, E. Budyn, J. Chessa, and T. Belytschko. An extended finite element method with higher-order elements for curved cracks. *Computational Mechanics*, 31:38–48, 2003.

[138] E. Stein and S. Ohnimus. Coupled model- and solution-adaptivity in the finite-element method. *Computer Methods in Applied Mechanincs and Engineering*, 150:327–350, 1997.

[139] E. Stein and M. Rüter. Finite element methods for elasticity with error-controlled discretization and model adaptivity. *Encyclopedia of Computational Mechanics*, 2007.

[140] M. Stolarska, D. L. Chopp, N. Moës, and T. Belytschko. Modelling crack growth by level sets in the extended finite element method. *International Journal for Numerical Methods in Engineering*, 51:943–960, 2001.

[141] T. Strouboulis, I. Babuška, and K. Copps. The design and analysis of the generalized finite element method. *Computer Methods in Applied Mechanics and Engineering*, 181:43–69, 2000.

[142] T. Strouboulis, K. Copps, and I. Babuška. The generalized finite element method. *Computer Methods in Applied Mechanics and Engineering*, 190:4081–4193, 2001.

[143] T. Strouboulis, L. Zhang, D. Wang, and I. Babuška. A posteriori error estimation for generalized finite element methods. *Computer Methods in Applied Mechanics and Engineering*, 195:852–879, 2006.

[144] N. Sukumar, D. L. Chopp, N. Moës, and T. Belytschko. Modeling holes and inclusions by level sets in the extended finite-element method. *Computer Methods in Applied Mechanics and Engineering*, 190:6183–6200, 2001.

[145] N. Sukumar, N. Moës, B. Moran, and T. Belytschko. Extended finite element method for three-dimensional crack modelling. *International Journal for Numerical Methods in Engineering*, 48:1549–1570, 2000.

[146] B. Szabó and I. Babuška. *Finite Element Analysis*, chapter Estimation and Control of Errors of Discretization, pages 290–315. Wiley, 1991.

[147] V. P. Tamuzs and V. E. Petrova. On macrocrack-microdefect interaction. *Inernational Applied Mechanics*, 38:1157–1177, 2002.

[148] I. Temizer and P. Wriggers. An adaptive multiscale resolution strategy for the finite deformation analysis of microheterogeneous structures.

[149] D. M. Tracey. Finite elements for three-dimensional elastic crack analysis. *Nuclear Engineering and Design*, 26:282–290, 1974.

[150] C. Truesdesll and R. A. Toupin. *Encyclopedia of Physiks, Principles of classical mechanics and field theory*, volume 3, chapter The classical field theories, pages 226–793. Springer, 1960.

[151] G. Ventura. On the elimination of quadrature subcells for discontinuous functions in the extended finite-element method. *International Journal for Numerical Methods in Engineering*, 66:761–795, 2006.

[152] G. Ventura, R. Gracie, and T. Belytschko. Fast integration and weight function blending in the extended finite element method. *International Journal for Numerical Methods in Engineering*, 77:1–29, 2009.

[153] P. F. Walsh. The computation of stress intensity factors by a special finite element technique. *International Journal of Solids and Structures*, 7:1333–1342, 1971.

[154] G. N. Wells and L. J. Sluys. A new method for modelling cohesive cracks using finite elements. *International Journal for Numerical Methods in Engineering*, 50:2667–2682, 2001.

[155] H. M. Westergaard. Bearing pressure and cracks. *Trans. ASME Journal of Applied Mechanics*, 66:49–53, 1939.

[156] M. L. Williams. The bending stress distribution at the base of a stationary crack. *Journal of Applied Mechanics*, 28:78–82, 1961.

[157] P. Wriggers. *Nichtlineare Finite-Element-Methoden*. Springer, 2001.

[158] C. C. Wu, R. W. Rice, and P. F. Becher. The character of cracks in fracture toughness measurements of ceramics. *Fracture Mechanics Methods for Ceramics, Rocks and Concrete*, ASTM STP 745:127–140, 1981.

[159] X.-P. Xu and A. Needleman. Numerical simulations of fast crack growth in brittle solids. *Journal of the Mechanics and Physics of Solids*, 42:1397–1434, 1994.

[160] O. C. Zienkiewicz, R. L. Taylor, and J. Z. Zhu. *The finite element method for solids and structural mechanics*. Elsevier, 6 edition, 2005.

[161] O. C. Zienkiewicz, R. L. Taylor, and J. Z. Zhu. *The finite element method: its basis and fundamentals*. Elsevier, 6 edition, 2005.

[162] O. C. Zienkiewicz and J. Z. Zhu. A simple error estimator and adaptive procedure for practical engineering analysis. *International Journal for Numerical Methods in Engineering*, 24:337–357, 1987.

[163] A. Zilian and A. Legay. The enriched space-time finite element method (EST) for simultaneous solution of fluid-structure interaction. *International Journal for Numerical Methods in Engineering*, 75:305–334, 2008.

Curriculum vitae

Corinna Prange

born March 4, 1984 in Rheda-Wiedenbrück, Germany

Professional Experience

since 03.2014	Scientist Applied Research Contact Physics, Continental Reifen Deuschland GmbH Hannover
04.2008 - 02.2014	Research assistant at the Institute of Continuum Mechanics, Leibniz Universität Hannover
09.2011 - 02.2013	Lectureship Engineering Mechanics 1, University of Applied Sciences and Arts, Hannover
01.2008 - 03.2008	Design engineer, at Miele & Cie. KG, Lehrte

Education

09.2003 - 12.2007	University of Applied Sciences and Arts Hannover Mechanical Engineering (as dual education) Focus: Construction Technology Degree: Dipl.-Ing. (FH)
09.2003 - 05.2005	Apprenticeship as a Mechatronics Engineer Miele & Cie. KG, Lehrte
1990 - 2003	Secondary education at the grammar school, Verl Elementary education at the primary school Grosse Heide, Gütersloh